CAIT-UTC-NC22

Long-Term Monitoring of a Geosynthetic Reinforced Soil Integrated Bridge System (GRS-IBS)

FINAL REPORT
November 2017

Submitted by:

Christopher L. Meehan
Associate Professor

Tyler M. Poggiogalle
Graduate Student

University of Delaware, Department of Civil and Environmental Engineering
301 DuPont Hall, Newark, DE 19716, U.S.A.

External Project Manager
Jason Hastings, M.C.E., P.E.

In cooperation with

Rutgers, The State University of New Jersey
And
Delaware
Department of Transportation
And
U.S. Department of Transportation
Federal Highway Administration

Disclaimer Statement

The contents of this report reflect the views of the authors, who are responsible for the facts and the accuracy of the information presented herein. This document is disseminated under the sponsorship of the Department of Transportation, University Transportation Centers Program, in the interest of information exchange. The U.S. Government assumes no liability for the contents or use thereof.

The Center for Advanced Infrastructure and Transportation (CAIT) is a National UTC Consortium led by Rutgers, The State University. Members of the consortium are the University of Delaware, Utah State University, Columbia University, New Jersey Institute of Technology, Princeton University, University of Texas at El Paso, Virginia Polytechnic Institute, and University of South Florida. The Center is funded by the U.S. Department of Transportation.

1. Report No.	2. Government Accession No.	3. Recipient's Catalog No.
CAIT-UTC-NC22		

4. Title and Subtitle	5. Report Date
Long-Term Monitoring of a Geosynthetic Reinforced Soil Integrated Bridge System (GRS-IBS)	November 2017
	6. Performing Organization Code CAIT/University of Delaware

TECHNICAL REPORT STANDARD TITLE PAGE

7. Author(s)	8. Performing Organization Report No.
Christopher L. Meehan, Tyler M. Poggiogalle	CAIT-UTC-NC22

9. Performing Organization Name and Address	10. Work Unit No.
University of Delaware 301 DuPont Hall, Newark, DE 19716, U.S.A.	
	11. Contract or Grant No. DTRT12-G-UTC28

12. Sponsoring Agency Name and Address	13. Type of Report and Period Covered
Center for Advanced Infrastructure and Transportation Rutgers, The State University of New Jersey 100 Brett Road Piscataway, NJ 08854	Final Report 9/1/16 - 8/31/17
	14. Sponsoring Agency Code

15. Supplementary Notes
U.S. Department of Transportation/OST-R
1200 New Jersey Avenue, SE
Washington, DC 20590-0001

16. Abstract

The geosynthetic reinforced soil integrated bridge system (GRS-IBS) is an innovative alternative to conventional bridge technology that utilizes closely spaced layers of geosynthetic reinforcement and compacted granular fill material to provide direct bearing support for structural bridge members. Using this technology, over 200 bridges in 44 states, Puerto Rico, and the District of Columbia have been built as of early 2017. In 2013, the first GRS-IBS in the state of Delaware was constructed. An overview of the design, construction, and monitoring process that was performed for this GRS-IBS project will be discussed in this report. This report will focus on the data collected over the past year of operation, September 1, 2016 through August 31, 2017. To evaluate the performance of the GRS-IBS structure over this time period, this data is compared with the data collected from the construction, load testing, and initial monitoring period of this structure, May 29, 2013 through August 31, 2016. In general, the instrumentation installed for this project indicated that the structure has performed well over the current monitoring period.

17. Key Words	18. Distribution Statement
Geosynthetics, Geosynthetic Reinforced Soil, Bridge Abutment	No restrictions

19. Security Classification (of this report)	20. Security Classification (of this page)	21. No. of Pages	22. Price
Unclassified	Unclassified	139	

Form DOT F 1700.7 (8-69)

Acknowledgements

This research was supported by the Center for Advanced Infrastructure and Transportation (CAIT) National UTC consortium led by Rutgers, The State University of New Jersey. CAIT UTC is funded by the US Department of Transportation (grant number DTRT13-G-UC28) and matching funds organized by the Delaware Center for Transportation. This material is also based upon work supported by the Delaware Department of Transportation under Award Nos. 12A00269 and 11A01477. The authors would also like to acknowledge support provided by Mike Adams, Jennifer Nicks, Majid Talebi, Matthew Becker, Daniel Cacciola, William Baker, Truxton Boyce, Marc Toussant, and Scott Forsythe.

Table of Contents

Chapters ii
List of Figures iv
List of Tables viii

Chapters

1. Description of the Problem 1
1.1 Introduction 1
References 6

2. Approach 7
2.1 Introduction 7
2.2 Project Specifications 7
2.2.1 Geometrical Specifications 7
2.2.2 Geotechnical Specifications 8
2.2.3 Reinforced Fill Material 10
2.2.4 Reinforced Soil Foundation (RSF) 10
2.2.5 Road Base Material 10
2.2.6 Concrete Masonry Unit (CMU) Blocks 11
2.2.7 Geosynthetic 11
2.3 Design Layout 12
2.4 Loading 12
2.5 External Stability Analysis 13
2.6 Internal Stability Analysis 14
2.7 Typical Geometrical Section 15
2.8 Construction 15
References 17

3. Methodology 18

3.1 Introduction 18
3.2 Sensors 20
3.2.1 Inclinometer Sensors 24
3.2.2 Piezometers 25
3.2.3 Pressure Cells 26
3.2.4 Strain Gauges 28
3.2.5 Thermistors 29
3.2.6 Volumetric Water Content Sensors 30
3.2.7 Surveying Targets 31
3.3 Data Collection Process 32
References 35

4. Findings 39
4.1 Introduction 39
4.2 Analysis of the Collected Data 39
4.2.1 Volumetric Water Content and Pore Water Pressure 40
4.2.2 Temperature measured by the Thermistors 48
4.2.3 Strain in the Abutment Measured by the Strain Gauges 52
4.2.4 Under Bridge Strain Gauges 64
4.2.5 Facing Wall Movements Measured by Surveying Targets 66
4.2.6 Inclinometer Sensors 104
4.2.7 Foundation Pressure Cells 109
4.2.8 Abutment Pressure Cells 115
4.3 Conclusion 120
References 121

5. Conclusions and Recommendations 122
5.1 Introduction 122
5.2 Conclusions 122
5.3 Recommendations 126
References 128

List of Figures

Figure 1.1 Typical GRS-IBS cross-section (modified after Adams et al. 2011) 4
Figure 1.2 Location of Bridge 1-366 in Delaware 5
Figure 2.1 Cross-section of Bridge 1-366, along the roadway centerline 8
Figure 2.2 Bridge 1-366 plan view 8
Figure 2.3 Soil layer geometry with engineering properties used for Bridge 1-366 design 9
Figure 2.4 Bridge 1-366 typical section 15
Figure 2.5 Existing Bridge 1-366 before demolition 16
Figure 2.6 Completed Bridge 1-366 16
Figure 3.1 Bridge 1-366 instrumented section about the roadway centerline 19
Figure 3.2 In-place inclinometer (IPI) sensor 25
Figure 3.3 IPI sensor array installation 25
Figure 3.4 Piezometer sensor 26
Figure 3.5 Piezometer sensor installation 26
Figure 3.6 Pressure cell 27
Figure 3.7 Pressure cell installation 27
Figure 3.8a Long strain gauge 28
Figure 3.8b Short strain gauge 28
Figure 3.9 Strain gauge wiring in the University of Delaware lab prior to site installation 29
Figure 3.10 Strain gauge protection and installation at the site 29
Figure 3.11 Thermistor 30
Figure 3.12 Thermistor installation 30
Figure 3.13 Volumetric water content sensor 31
Figure 3.14 East abutment facing wall surveying points 32
Figure 3.15 CR800 logger 33
Figure 3.16 CR1000 logger 33
Figure 3.17 Front and back view of rotary data switches 34
Figure 4.1 Measured volumetric water content 40
Figure 4.2 Histogram of volumetric water content for both monitoring periods 42
Figure 4.3 Histogram of volumetric water content for the current monitoring period 43

Figure 4.4 Minimum and maximum measured water content profile for both monitoring periods 44
Figure 4.5 Minimum and maximum measured water content profile for the current monitoring period 44
Figure 4.6 Measured pore water pressures 45
Figure 4.7 Measured precipitation 46
Figure 4.8 Change in river water elevation.....46
Figure 4.9 Histogram of water elevation in the river for both monitoring periods 47
Figure 4.10 Histogram of water elevation in the river for the current monitoring period.....47
Figure 4.11 Recorded temperatures in the west abutment.....49
Figure 4.12 Recorded temperatures in the east abutment.....50
Figure 4.13 Ambient air temperature.....51
Figure 4.14 West abutment short strain gauge readings (uncorrected) 53
Figure 4.15 West abutment long strain gauge readings (uncorrected) 54
Figure 4.16 West abutment short strain gauge readings (corrected) 55
Figure 4.17 West abutment long strain gauge readings (corrected) 58
Figure 4.18 East abutment short strain gauge readings (uncorrected).....62
Figure 4.19 East abutment long strain gauge readings (uncorrected).....63
Figure 4.20 Under bridge strain gauge readings.....65
Figure 4.21 Lateral deflection of the east facing wall at the abutment centerline.....67
Figure 4.22 Lateral deflection of the west facing wall at the abutment centerline.....68
Figure 4.23 Settlement of the east facing wall at the abutment centerline 69
Figure 4.24 Settlement of the west facing wall at the abutment centerline 70
Figure 4.25 Lateral deflection of the east facing wall at 5.6 m offset from the abutment centerline, in the upstream direction.....71
Figure 4.26 Lateral deflection of the west facing wall at 5.6 m offset from the abutment centerline, in the upstream direction.....72
Figure 4.27 Settlement of the east facing wall at 5.6 m offset from the abutment centerline, in the upstream direction.....73
Figure 4.28 Settlement of the west facing wall at 5.6 m offset from the abutment centerline, in the upstream direction.....74

Figure 4.29 Lateral deflection of the east facing wall at 2.8 m offset from the abutment centerline, in the upstream direction.....75
Figure 4.30 Lateral deflection of the west facing wall at 2.8 m offset from the abutment centerline, in the upstream direction.....76
Figure 4.31 Settlement of the east facing wall at 2.8 m offset from the abutment centerline, in the upstream direction.....77
Figure 4.32 Settlement of the west facing wall at 2.8 m offset from the abutment centerline, in the upstream direction.....78
Figure 4.33 Lateral deflection of the east facing wall at 2.8 m offset from the abutment centerline, in the downstream direction.....79
Figure 4.34 Lateral deflection of the west facing wall at 2.8 m offset from the abutment centerline, in the downstream direction.....80
Figure 4.35 Settlement of the east facing wall at 2.8 m offset from the abutment centerline, in the downstream direction.....81
Figure 4.36 Settlement of the west facing wall at 2.8 m offset from the abutment centerline, in the downstream direction.....82
Figure 4.37 Lateral deflection of the east facing wall at 5.6 m offset from the abutment centerline, in the downstream direction.....83
Figure 4.38 Lateral deflection of the west facing wall at 5.6 m offset from the abutment centerline, in the downstream direction.....84
Figure 4.39 Settlement of the east facing wall at 5.6 m offset from the abutment centerline, in the downstream direction.....85
Figure 4.40 Settlement of the west facing wall at 5.6 m offset from the abutment centerline, in the downstream direction.....86
Figure 4.41 Contour plots of the east facing wall deflection over both monitoring periods.....87
Figure 4.42 Contour plots of the west facing wall deflection over both monitoring periods.....90
Figure 4.43 Contour plots of the east facing wall settlement over both monitoring periods.....93
Figure 4.44 Contour plots of the west facing wall settlement over both monitoring periods.....96
Figure 4.45 Changes in the west abutment wall lateral deflection over both monitoring periods 100

Figure 4.46 Changes in the east abutment wall lateral deflection over both monitoring periods..... 101
Figure 4.47 Changes in the west abutment wall settlement over both monitoring periods 102
Figure 4.48 Changes in the east abutment wall settlement over both monitoring periods 103
Figure 4.49 Lateral deflection in the E-W direction recorded by the inclinometer sensors 105
Figure 4.50 Lateral deflection in the N-S direction recorded by the inclinometer sensors 106
Figure 4.51 Initial and final foundation deflection in the E-W direction for both monitoring periods 107
Figure 4.52 Initial and final foundation deflection in the E-W direction for the current monitoring period 107
Figure 4.53 Initial and final foundation deflection in the N-S direction for both monitoring periods 108
Figure 4.54 Initial and final foundation deflection in the N-S direction for the current monitoring period 108
Figure 4.55 Measured total pressures 110
Figure 4.56 Measured total and effective pressures.....111
Figure 4.57 Changes in effective pressure distribution beneath the RSF for both monitoring periods 112
Figure 4.58 Changes in effective pressure distribution beneath the RSF for the current monitoring period 112
Figure 4.59 Histogram of effective pressure for both monitoring periods 113
Figure 4.60 Histogram of effective pressure for the current monitoring period.....114
Figure 4.61 Measured abutment pressures.....116
Figure 4.62 Histogram of measured abutment pressures for both monitoring periods 117
Figure 4.63 Histogram of measured abutment pressures for the current monitoring period.....118
Figure 4.64 Minimum, maximum, and average measured abutment pressures for both monitoring periods.....119
Figure 4.65 Minimum, maximum, and average measured abutment pressures for the current monitoring period.....119

List of Tables

Table 2.1 Geotextile Properties.....11
Table 2.2 Bridge 1-366 Loads and Surcharges.....13
Table 3.1 Instrumentation Data.....18

Chapter 1

Description of the Problem

1.1 Introduction

According to Federal Highway Administration (FHWA) reports, many of the 600,000 bridges in the United States have functional or structural deficiencies (FHWA 2011c). Financial resources to completely repair or replace these bridges are unavailable in most states (FHWA 2011a). To combat this, researchers have focused on developing more economical means for bridge repair and construction (Wu 1994). Concepts from the design of mechanically stabilized earth (MSE) retaining walls and geosynthetic reinforced soil (GRS) retaining walls can be applied to bridge abutment construction, with the potential for significant cost savings and a reduction of construction time (e.g., Adams et al. 2011).

Thousands of years ago reinforced earth structures were built using materials consisting of straw, tree branches, and other plants. More modern reinforced earth structures use more resilient reinforcement materials, like MSE walls that appeared in the 1960's, which use embedded steel reinforcing strips attached to facing elements for soil reinforcement (Berg et al. 2009). Geosynthetics were then introduced later on in the 1980's as another technique for reinforced earth structures; the use of geosynthetics helped solve corrosion problems which had been observed in the steel reinforcement of MSE structures (Berg et al. 2009). The FHWA has made advances in bridge construction over the last few years by incorporating developments from GRS construction methods into the bridge construction process.

Geosynthetic reinforced soil systems are defined by the FHWA as having close reinforcement spacing (about 0.2 m), which differs from MSE structures that typically have larger

reinforcement spacings than this; in other literature, GRS has been used to describe reinforced soil systems with geosynthetics at any spacing (Adams et al. 2011). The geosynthetic reinforcement in GRS systems serves many different purposes including: increased confinement, dilation restraint, lateral deformation reduction, and tensile inclusion to resist tensile forces (Adams et al. 2011). GRS structures have seen large growth in the United States with over 100,000 square facing feet being constructed over the last 30 years (FHWA 2011a).

Geosynthetic reinforced soil integrated bridge system (GRS-IBS) technology has been developed through research at the FHWA and has shown savings in cost and construction time compared to conventional bridge structures and construction methods (Adams et al. 2011). The GRS-IBS is a composite bridge structure with prefabricated bridge superstructure elements that bear directly on top of the GRS abutments. History shows that if designed and constructed properly, GRS-IBS structures have performed well under static and dynamic loading conditions; it was also seen that compared to conventional bridges, GRS-IBS structures can be constructed in variable weather conditions, with fewer construction difficulties, and simpler maintenance over the lifespan of the structure compared to conventional bridges (e.g., Helwany et al. 2007, 2012; Adams et al. 2011; Tatsuoka et al. 2013).

The GRS abutment is constructed by alternating layers of compacted soil with geosynthetic reinforcement. The geosynthetic is frictionally connected to the facing elements of the GRS abutment (which are most commonly concrete masonry unit (CMU) blocks); there are no rigid (i.e., structural) connection elements, as is commonly utilized with MSE structures (Adams et al. 2011). The close spacing of the reinforcement allows for stress arching between the soil reinforcement layers to play a more significant role, thus preventing the facing elements from holding back as much soil as typically seen in MSE facing elements. By encapsulating a series of

compacted soil layers with geosynthetic, a reinforced soil foundation (RSF) is used to support the base of the reinforced soil zone in fair foundation conditions. Rip rap scour protection is placed in front of the facing wall elements to prevent undermining and soil erosion if the GRS-IBS passes over a waterway. The composite soil/geosynthetic mass within the GRS abutment is strong enough to directly support the dead and live loads that are applied to the bridge superstructure due to the significant compressive and tensile strength. For the bridge span itself, a concrete box beam superstructure is popular for shorter span bridges but other steel, concrete, or composite superstructures can also be used (Russell 2011). It is common to support a concrete box beam superstructure on a beam seat which is directly built in to the GRS abutment. To help with load shedding from the bridge loads, additional bearing bed reinforcement is placed beneath the beam seat which helps serve as an embedded footing in the reinforced soil mass; this bearing bed reinforcement should be placed at a minimum of half the spacing seen in the GRS abutment (Adams et al. 2011). An integrated approach consisting of reinforced backfill in conjunction with a jointless continuous pavement interface is used at the end of both sides of the bridge beams. The elements discussed above are shown in Figure 1.1 (Adams et al. 2011).

There were 100 GRS-IBS structures in more than 20 states by the end of 2012 (FHWA 2011b). By the middle of 2014, this number had increased to 150 GRS-IBS structures in more than 35 states (Talebi et al. 2014). Currently, the most recent reports have this number at over 200 bridges in 44 states, Puerto Rico, and the District of Columbia as of early 2017 (FHWA 2017). The increasing popularity of this new technology can be seen with the construction of over 100 new bridges in 24 new states, Puerto Rico, and the District of Columbia over the course of just five years; this is also a product of the promotion of this technology through the “Every Day Counts” initiative by the FHWA.

Given its demonstrated benefits in other parts of the country, the Delaware Department of Transportation (DelDOT) decided to explore the effectiveness of GRS-IBS technology for use within the State of Delaware. To replace a bridge that has reached the end of its service life, a new GRS-IBS, Bridge 1-366, was constructed in New Castle County by DelDOT on Chesapeake City Road over Guthrie Run; the location of Bridge 1-366 is shown in Figure 1.2. Bridge 1-366 was the first GRS-IBS in the state of Delaware. DelDOT managed the design and construction processes for this project while University of Delaware staff and students worked with DelDOT to provide technical guidance through design assistance and construction inspection. An innovative system of sensors was designed by University of Delaware personnel to monitor structure performance over time.

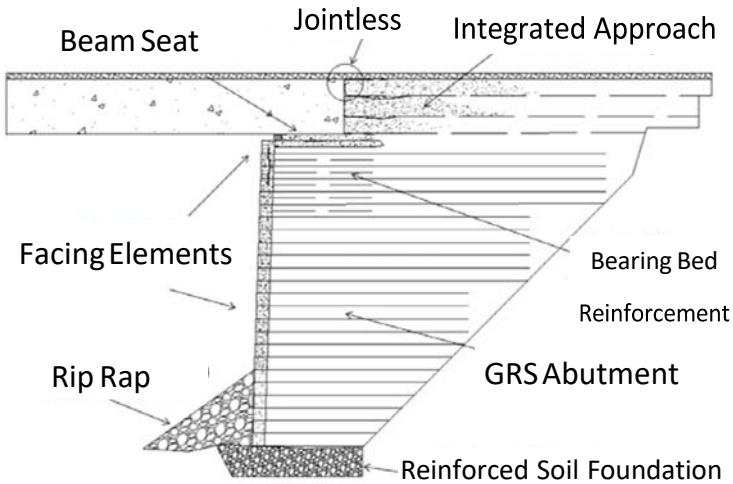

Figure 1.1 Typical GRS-IBS cross-section (modified after Adams et al. 2011)

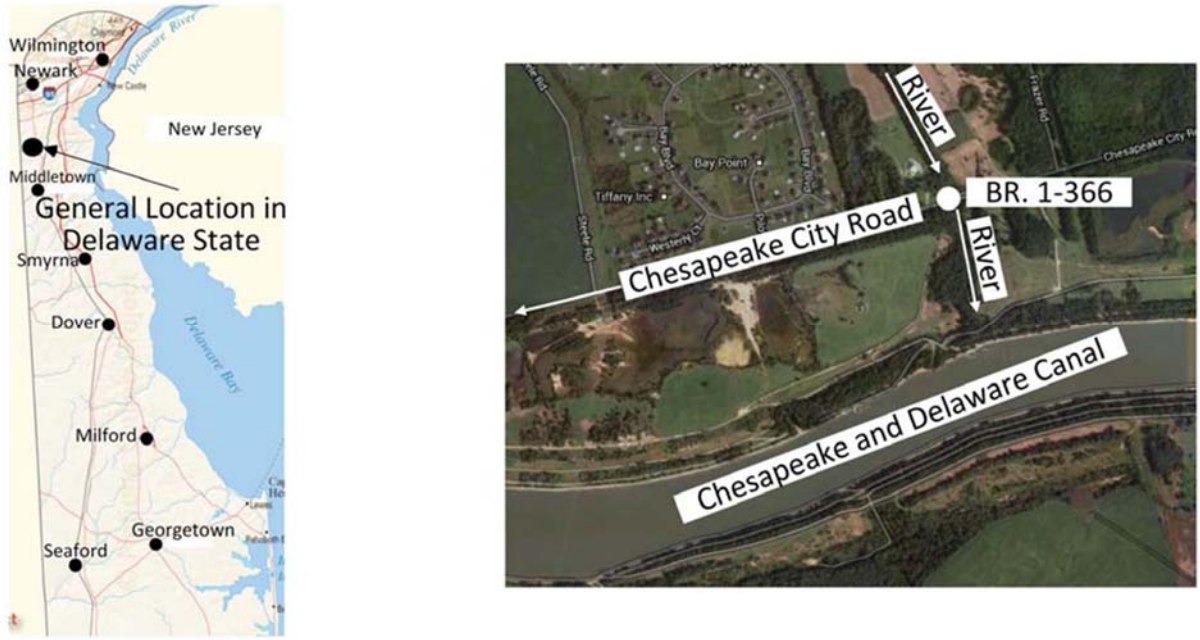

Figure 1.2 Location of Bridge 1-366 in Delaware

An overview of the design, construction, and monitoring process that was performed for this GRS-IBS project will be discussed in this report. This report will focus on the data collected over the past year of operation, September 1, 2016 through August 31, 2017. To evaluate the performance of the GRS-IBS structure over this time period, this data will be compared with the data collected from the construction, load testing, and the initial monitoring period of this structure, May 29, 2013 through August 31, 2016.

References

Adams, M., Nicks, J., Stabile, T., Wu, J., Schelatter, W. and Hartmann, J., (2011). "Geosynthetic Reinforced Soil Integrated Bridge System Interim Implementation Guide", Publication No. FHWA-HRT-11-026, Federal Highway Administration, Washington, DC.

Berg, R. Christopher, B. and Samtani, N. (2009). "Design and Construction of Mechanically Stabilized Earth Walls and Reinforced Soil Slopes", Publication No. FHWA-NHI-10-024, Federal Highway Administration, Washington, DC

FHWA, (2011a). "Geosynthetic Reinforced Soil Integrated Bridge System (GRSIBS)". EDC1 Regional Summits, www.fhwa.dot.gov/everydaycounts/pdfs/summits/GRSIBS_full_presentation.pdf

FHWA, (2011b). "Semi-Annual Project Delivery Report". www.fhwa.dot.gov/wadiv/preports/semiannual_ix.pdf

FHWA (2011c). "Bridge guide", Publication No. FHWA-HIF-11-042, Federal Highway Administration, Washington, DC.

FHWA, (2017). "Geosynthetic Reinforced Soil Integrated Bridge System (GRSIBS)". EDC3 Regional Summits, www.fhwa.dot.gov/everydaycounts/pdfs/summits/GRSIBS_full_presentation.pdf

Helwany, S., Wu, J. and Kitsabunnarat, A. (2007), "Simulating the Behavior of GRS Bridge Abutments." Journal of Geotechnical and Geoenvironmental Engineering, 133 (10): 1229-1240.

Russell, H., (2011). "Adjacent Precast Concrete Box-Beam Bridges: State of the Practice." Precast/Prestressed Concrete Institute Journal, 56 (1): 75-91.

Tatsuoka, F., Tateyama, M., Koda, M. and Koseki, J. (2013). "Seismic Design, Construction and Performance of Geosynthetic-Reinforced Soil Retaining Walls and Bridge Abutments for Railways in Japan." Proceeding of the 2013 Geo- Congress, San Diego, CA, 1143-1157.

Talebi, M., Meehan, C., Cacciola, D. and Becker, M. (2014). "Rapid Replacement." Journal of Civil Engineering, ASCE, April 2014, 64-69 and 81.

Wu, J. (1994). "Design and construction of low cost retaining walls: The next generation in technology." CTI-UCD-1-94, Colorado Transportation Institute, Denver

Chapter 2

Approach

2.1 Introduction

An overview of the design, construction, and instrumentation of Bridge 1-366 in New Castle County, Delaware is provided in this chapter. As discussed in Chapter 1, Bridge 1-366 is located on Chesapeake City Road over Guthrie Run and was newly constructed in 2013 as a GRS-IBS structure to replace an existing bridge that had reached the end of its service life. FHWA interim implementation guidelines for GRS-IBS structures were followed for the design of this bridge (Adams et al. 2011).

2.2 Project Specifications

2.2.1 Geometrical Specifications

DelDOT engineers provided preliminary geometrical details for this project and concluded that the maximum height from the road elevation to the bottom of the foundation was to be approximately 6.1 m. This is less than the maximum allowable height of approximately 9 m that is specified for GRS-IBS structures (Adams et al. 2011). The span length of the structure was determined to be 8.7 m and the overall bridge superstructure length was 11.3 m (giving a 1.3 m bearing seat width for both ends of the bridge). The width of the bridge was determined to be 12.2 m and includes two lanes with shoulders. The length and width of each abutment measure 9.8 m and 14.6 m respectively. Figures 2.1 and 2.2 depict the cross-sectional view of the GRS-IBS structure along the roadway centerline and the plan view of the structure, respectively.

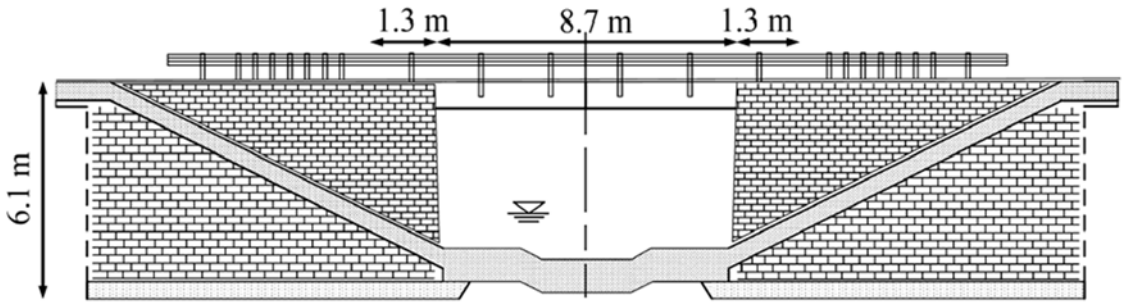

Figure 2.1 Cross-section of Bridge 1-366, along the roadway centerline

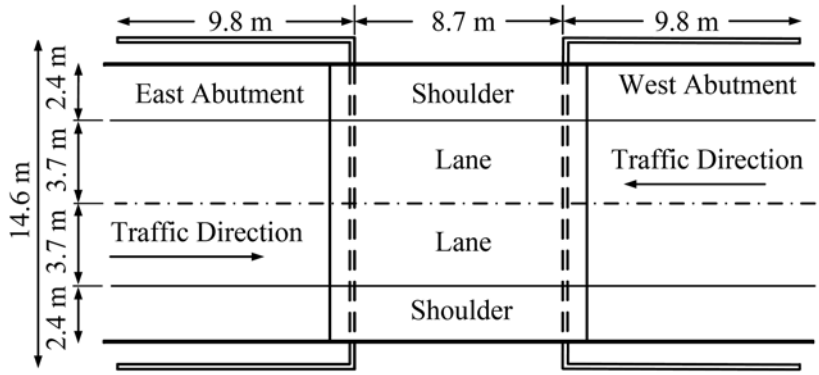

Figure 2.2 Bridge 1-366 plan view

2.2.2 Geotechnical Specifications

One borehole was drilled in each abutment as part of the geotechnical exploration process for a total of two total boreholes. Each borehole was drilled to a depth of 18.3 m in which bedrock was not observed in either of the borings and groundwater was observed at a depth of approximately 3.5 m from the ground surface. Also from these borings, 41 soil classification tests, six consolidation tests, two unconfined compression tests, four unconfined undrained triaxial shear tests, and 11 organic content tests were performed. In depth details from the boring data and the test results mentioned can be found in the appendix of Talebi (2016). Soil layer geometry was determined from the laboratory tests in addition to published correlation and engineering judgement; soil unit weights and strength parameters were also determined for the design of the GRS-IBS. Figure 2.3 displays this soil layer geometry with engineering properties assigned to each

layer. The soil exploration showed a soil profile consisting of granular and fine materials ranging from SM-SC to CL in the United Soil Classification System (USCS). Using the standard penetration testing (SPT) results and recovered samples, approximately the first 4 meters of soil was determined to be a medium dense, fine sandy material with silt and clay. Following this layer, a thin layer of stiff orange sandy clay was detected followed by a grayish-brown silty fine sandy clay layer which continued to a depth of approximately 8.5 m; this larger layer is medium stiff to stiff and includes organic material at some depths. After this layer, a dense to very dense, fine sand layer with silt was observed, extending to the end of the borehole exploration with the observance of a thin clay layer at approximately 1 m from the end of the borehole.

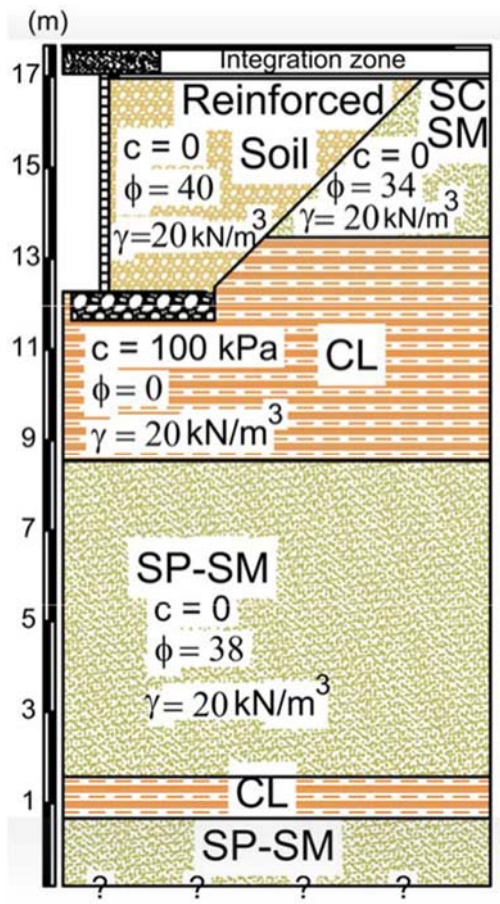

Figure 2.3 Soil layer geometry with engineering properties used for Bridge 1-366 design

2.2.3 Reinforced Fill Material

No. 8 stone was used for the backfill material in the reinforced zone, following the requirements provided by the interim implementation guidelines for GRS-IBS structures (Adams et al. 2011). No. 8 stone is described as a coarse material consisting of crushed stone with a relatively uniform gradation; DelDOT has approved this material for use in construction and it generally conforms to the associated material specification for GRS-IBS backfill material (Adams et al. 2011). Seven gradation tests were conducted at the University of Delaware lab to ensure that the material was in agreement with the standard provided by DelDOT (2001); all gradation results fit the allowable range. For the design of Bridge 1-366, the following properties for the reinforced fill material were utilized: a unit weight of 20 kN/m^3, a maximum diameter of 0.013 m, a cohesion of 0 kPA, and a friction angle of 40 degrees. More details regarding the reinforced fill material and gradation test results can be found in Chapter 3 of Talebi (2016).

2.2.4 Reinforced Soil Foundation (RSF)

No. 8 stone was used to construct the RSF, which was the same material used for the backfill material in the abutment construction; this material was selected in accordance with FHWA recommendations (Adams et al. 2011).

2.2.5 Road Base Material

For the roadway approach for the GRS-IBS, a granular fill material was placed and compacted as the road base. The estimated properties for the road base are as follows: a unit weight of 22 kN/m^3, cohesion of 0 kPa, and a friction angle of 40 degrees. These estimated properties were determined based on values from Adams et al. (2011).

2.2.6 Concrete Masonry Unit (CMU) Blocks

The split-face CMU block with dimensions of 0.2 m by 0.2 m by 0.4 m is the most commonly used facing element for GRS walls and abutments. With the selection of this facing element, soil is placed and compacted every 0.2 m (the thickness of the CMU block), which allows for easy field monitoring of soil compaction.

2.2.7 Geosynthetic

A biaxial, woven polypropylene (PP) geotextile was used for the construction of Bridge 1-366 after Adams et al. (2011) stated that the utilization of this type of geotextile was common for reinforcing elements used in GRS-IBS structures. The geotextile reinforcement used was HPG-57 and was provided by Hanes Geo Component. HPG-57 is stabilized to resist degradation due to ultraviolet exposure and is also resistant to common soil chemicals, mildew, and insects according to the manufacturer. For this material, an ultimate strength of 70 kN/m was used for GRS load-bearing applications. Polypropylene is one of the most stable polymers available for geotextiles as it is stable between pH levels of 2 to 13. Table 2.1 provides the main properties of this material.

Table 2.1 Geotextile Properties

Property	**Test Method**	**Value**
Wide Width Tensile Strength (Max)	ASTM D4595	70 x 70 kN/m
Wide Width Tensile Strength (2% Strain)	ASTM D4595	14 x 19.3 kN/m
Wide Width Tensile Strength (5% Strain)	ASTM D4595	35 x 39.4 kN/m
Permittivity	ASTM D4491	0.400 sec^{-1}
UV Resistance	ASTM D4355	80% @ 500 hr.

2.3 Design Layout

A bearing width of 0.9 m was selected for the design of Bridge 1-366 based on the expected dead load (DL) and live load (LL) that the structure will experience. A setback distance between the back of the wall face and the front edge of the bridge beam should be 0.2 m, the height of the CMU block used. A clear space, the distance between the top of the CMU block wall and the bottom of the bridge superstructure, of 0.1 m was selected for this project. The RSF width, length, and depth for this project were determined to be 2.5 m, 3.13 m, and 0.63 m respectively. The spacing of the reinforcement is the same as the height of the CMU blocks, 0.2 m, and the reinforcement spacing within the bearing reinforcement bed is 0.1 m. The minimum reinforcement length at the base of the wall was determined to be 2.5 m. Moving upwards in the wall, the reinforcement length was chosen based on the 45-degree cut slope angle. In depth details on the determination of the design layout for this GRS-IBS structure can be found in Chapter 3 of Talebi (2016).

2.4 Loading

Detailed loading conditions are described in Chapter 3 of Talebi (2016). Table 2.2 summarizes the loads and surcharges that were selected for design of Bridge 1-366. Parameters used in Table 2.2 are as follows: h_{eq} = equivalent height of overburden for traffic surcharge, h_{rb} = height of road base, H = height of the GRS abutment, B_{RSF} and D_{RSF} = width and depth of the RSF, respectively, B = base length of reinforcement, γ_b = unit weight of retained backfill, γ_{rb} = unit weight of road base material, γ_r = unit weight of reinforced backfill, and K_{ab} = coefficient of active earth pressure (Adams et al. 2011).

Table 2.2 Bridge 1-366 Loads and Surcharges

Property	Notation	Measurement	Equation
Bridge DL	q_b	73.1 kPa	Calculated using the bridge weight
Bridge LL	q_{LL}	97.5 kPa	In accordance with AASHTO LRFD Bridge Design (2010)
Roadway LL	q_t	15 kPa	$qt = (h_{eq})(\gamma_b)$, $h_{eq} = 0.76$ m
Road Base DL	q_{rb}	11.7 kPa	$qrb = (h_{rb})(\gamma_{rb})$, $h_{rb} = 1.75 ft$
Weight of GRS Abutment	W	200 kN/m	$W = BH\gamma_r$
Weight of RSF	W_{RSF}	36.4 kN/m	$W_{RSF} = B_{RSF}D_{RSF}\gamma_r$
Lateral Load (Retained Backfill)	F_b	65.9 kN/m	$F_b = 0.5(\gamma_b)(H^2)K_{ab}$
Lateral Load (q_{rb} Effect)	F_{rb}	16.1 kN/m	$F_{rb} = (q_{rb})(H)K_{ab}$
Lateral Load (q_t Effect)	F_t	20.6 kN/m	$F_t = (q_t)(H)K_{ab}$

2.5 External Stability Analysis

External stability of the GRS-IBS was evaluated prior to the construction of the structure in 2013. Direct sliding, bearing capacity, and global stability failure mechanisms were assessed with the corresponding required factor of safety for each failure mechanism being 1.5, 3.0, and 1.5 respectively (Adams et al. 2011). The calculated factor of safety for each of these failure mechanisms was greater than the required factor of safety (factor of safety against direct sliding = 1.57, factor of safety against bearing capacity failure = 3.3, and factor of safety against global stability failure = 1.51). Details of the values and equations used in this analysis are available in Chapter 3 of Talebi (2016).

2.6 Internal Stability Analysis

Ultimate capacity corresponds to the ultimate load that can be applied before failure occurs. For this GRS-IBS structure, ultimate capacity was determined using an empirical method and an analytical method as suggested in Adams et al. (2011). It was concluded that the empirical approach and the analytical approach yielded satisfactory results thus concluding that the structure is stable against ultimate internal capacity failure.

Vertical and horizontal deformation applied by the superstructure dead load were also checked. A satisfactory factor of safety against vertical deformation failure of 2.9 was calculated. A lateral strain of 0.9% was calculated using equations from Adams at al. (2011). This is in accordance with the acceptable values of lateral strain in regards to horizontal deformation as the GRS-IBS interim implementation guide states the maximum lateral strain should not exceed 1% (Adams et al. 2011).

The GRS-IBS interim implementation guide states the geotextile strength at 2% strain should not be less than 23.3 kN/m (Adams et al. 2011). Applying a factor of safety of 3.5 to the strength of the reinforcement used in this project yields an allowable reinforcement strength of 23.3 kN/m. The maximum required reinforcement strength was calculated to be 19.5 kN/m which is less than the allowable reinforcement strength and thus, it can be concluded that the reinforcement strength is sufficient. More in-depth details including equations and values used in calculations for the internal stability analysis can be found in Chapter 3 of Talebi (2016).

2.7 Typical Geometrical Section

The geometry of Bridge 1-366 was decided upon from the overall project geometrical requirements as well as the calculations and process described in the previous section. The typical section of the structure can be seen in Figure 2.4.

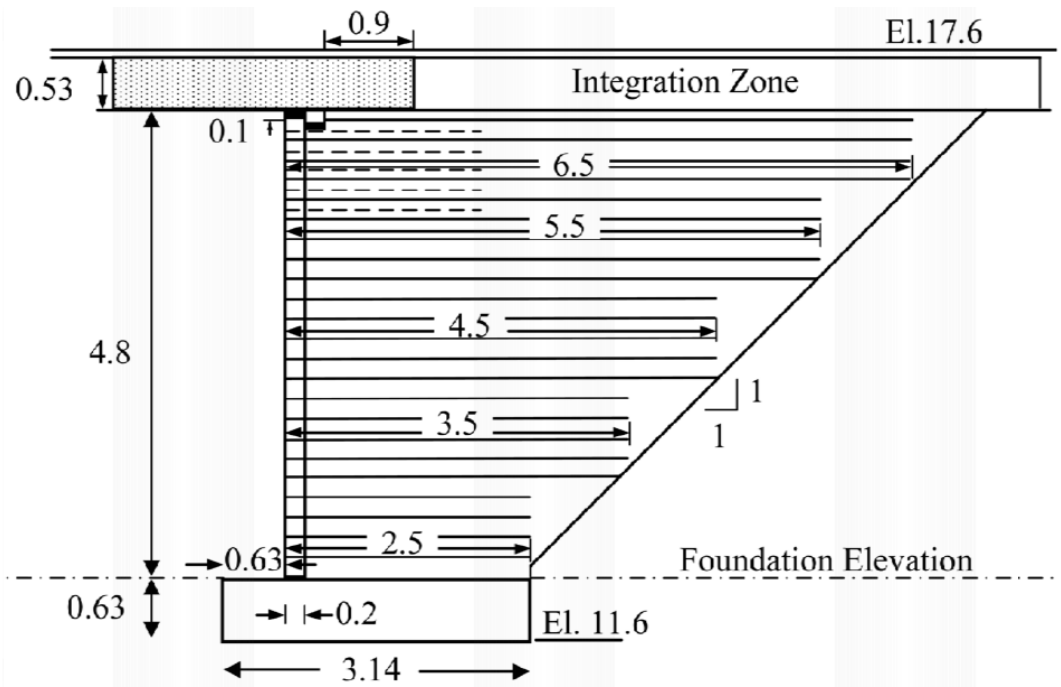

Figure 2.4 Bridge 1-366 typical section

2.8 Construction

The existing bridge before its demolition in March of 2013 can be seen in Figure 2.5. As discussed in previous sections, the bridge was to be replaced since it was at the end of its service life. Excavation for the east abutment foundation began on March 22, 2013 and the east abutment was completed on April 5, 2013. Excavation for the west abutment began on April 3, 2013 and the west abutment was completed on April 23, 2013. On April 25, 2013 the bridge beams were placed and the integrated zone was constructed over the three weeks following that. After the construction of the integration zone, paving was completed and guard rails were installed, thus completing the

GRS-IBS structure. The speed of construction was fairly quick given that this was the first GRS-IBS constructed in the state of Delaware and it is expected that similar future projects can be built at a more accelerated pace as contractors become familiar with the technology. Figure 2.6 shows the GRS-IBS structure approximately eight months after the completion of construction.

Figure 2.5 Existing Bridge 1-366 before demolition

Figure 2.6 Completed Bridge 1-366

Additional construction photos of abutment excavation and construction, bridge placement, and integration zone construction are available in Talebi (2016).

References

Adams, M., Nicks, J., Stabile, T., Wu, J., Schelatter, W. and Hartmann, J. (2011). "Geosynthetic Reinforced Soil Integrated Bridge System Interim Implementation Guide", Federal Highway Administration, Publication No. FHWA-HRT-11-026, Washington, DC.

AASHTO (2010). LRFD Bridge Design Specifications, Fifth Edition, American Association of State Highway and Transportation Officials, Washington, DC.

Delaware Department of Transportation (2001), "Standard Specifications for Road and Bridge Construction Manual".

Talebi, M. (2016). "Analysis of the field behavior of a geosynthetic reinforced soil integrated bridge system during construction and operation", PhD Dissertation, University of Delaware, 2016.

Chapter 3

Methodology

3.1 Introduction

The long-term performance of GRS-IBS technology is of interest to the Delaware Department of Transportation (DelDOT) to assess the viability of this technology for use within their bridge inventory. An instrumentation system was consequently designed and deployed to monitor the behavior of the first constructed GRS-IBS in Delaware over time after construction. Figure 3.1 displays the instrumented section about the roadway centerline as that is the location of all the sensors. There were 180 sensors installed consisting of in-place inclinometers, piezometers, pressure cells, strain gauges, thermistors, volumetric water content sensors, and surveying target points. Table 3.1 lists the instrument type with the location and number of sensors that were used. The following sections provide additional details about each sensor and its respective purpose served for this project.

Table 3.1 Instrumentation Data

Instrument types	**Location**	**No.**
Inclinometer sensors	Foundation, West GRS Abutment	4
Piezometers	Foundation, West GRS Abutment	3
Pressure cells	Foundation, West GRS Abutment, between Bridge and Integrated Zone	8
Strain gauges	West GRS Abutment, East GRS Abutment and beneath the Bridge	110
Thermistors	West GRS Abutment and East GRS Abutment	50
Volumetric water content sensors	West GRS Abutment	5
Surveying points	West and East Facing Walls	30

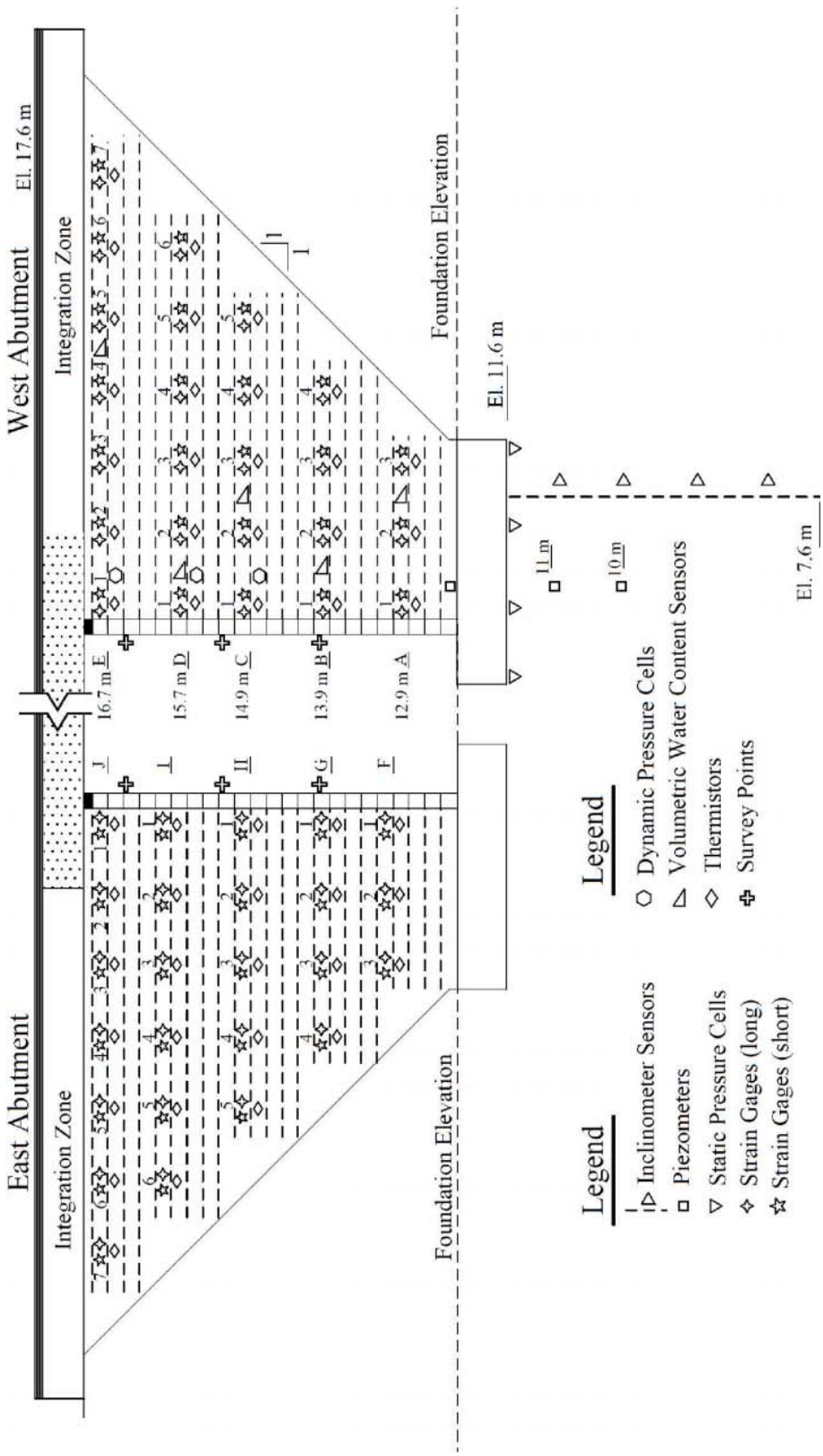

Figure 3.1 Bridge 1-366 instrumented section about the roadway centerline

3.2 Sensors

To investigate the potential effect of induced effective stress by changes in the abutment suction on the stability of the abutment, volumetric water content sensors were installed in the west abutment. Similarly, piezometers were installed in the foundation and lowermost level of the west abutment to capture changes in pore pressure in the fine-grained foundation soils. With this data, it becomes possible to assess the potential influence of pore water pressure on the performance of the structure. The volumetric water content sensors and the piezometers together provide useful data for the investigation of the effect water and water content have on the structure.

Studies have shown there is an effect of precipitation on the performance of reinforced backfill. Under real conditions, Ng and Pang (2000) indicated that about 60% of rainfall infiltrates in the soil and this amount of infiltration can ultimately affect the response of the backfill depending on its permeability. As expected for GRS-IBS structures over water, precipitation will increase the river water level which may have an adverse effect of the stability of the reinforced backfill by decreasing the soil strength in the reinforced soil zone, backfill, and foundation. Many researchers have studied the effect of water on the performance of reinforced earth structures. In some studies, it was determined that over 60% of failures and poor performance of GRS structures are caused by the presence of internal or external water (Koerner and Koerner 2013, Valentine 2013). Significantly more failures have been seen in structures that utilized fine grained backfill material due to poor drainage capabilities; this indicates the importance of backfill material selection on the overall performance of the structure.

Recently, researchers have investigated the importance of suction on the behaviors of reinforced soil abutments (Yoo and Jung 2006, Leshchinsky 2009, Leshchinsky and Tatsuoka 2013, Yoo 2013, Esmaili et al. 2014, Vahedifard et al. 2015). Increasing levels of suction tend to

increase the effective stress between soil particles; this increase in suction has the tendency to decrease abutment deformation under load thus increasing its stability (Fredlund et al. 1978). The effect of suction is not accounted for in the methods for design proposed by design manuals for reinforced soil structures (FHWA 2009, AASHTO 2014). Through experiments and numerical simulation, researchers have emphasized the adverse effect of the decrease in soil suction on the performance of low quality reinforced backfills (Yoo and Jung 2006, Kim and Borden 2013, Yoo 2013, Esmaili et al. 2014). By using non-woven geotextile as a reinforcing element in backfill material, the overall drainage capacity of the reinforced backfill is increased which decreased the failure potential (e.g., Portelinha et al. 2013).

Thermistors were installed in both the east and west abutments of the GRS-IBS structure to investigate the changes in abutment temperature and the influence temperature may have on the structure. A thermistor was also placed within the datalogger housing unit to record the ambient air temperature; this was used to investigate relationships between changes in ambient air temperature and abutment temperature. To date, most researchers have focused on the effect of air temperature change on bridge expansion and contraction which can induce pressure and deformation to the abutment. Some studies have incorporated temperature sensors in the reinforced soil backfill to evaluate the effect of the abutment temperature changes on the structure itself. Buttry et al. (1996) reported the influence that temperature and seasonal changes had on a 3.5 m high GRS segmental retaining wall; it was concluded that the changes in temperature ultimately affected the stress level and deformation in the wall. Abu-Hejleh et al. (2001) discussed measured air temperatures in comparison with soil temperatures nearest the facing wall and farthest from the facing wall; a cyclic lateral movement of the facing wall induced by the temperature change was

reported. These studies show that abutment temperature changes can influence deformation and pressure distribution in GRS structures.

Foil strain gauges and surveying targets were installed within the abutments and on the facing walls, respectively, to investigate the deformation of the GRS-IBS abutments. Two different strain gauges were utilized for comparison purposes, which will be discussed in more detail in a later section. Many researchers have used data from strain gauges and surveying targets to analyze the response of reinforced earth structures as it is very common to monitor the deformation of MSE and GRS structures (e.g., Wu et al. 2008, Yang et al. 2013, Lawrence 2014, Jiang et al. 2016, Nicks et al. 2016).

To monitor the clay foundation beneath the structure, inclinometer sensors were installed. The stability of the foundation of reinforced structures, including GRS walls and abutments, has been widely investigated by researchers (Abu-Hejleh et al. 2002, Helwany et al. 2003, Skinner and Rowe 2005, Wu 2006, Adams et al. 2007, Vennapusa et al. 2012, Santos et al. 2013 and 2014, Miyata et al. 2015). This is due to the critical effect that the foundation behavior can have on the overall performance of the structure.

Vibrating wire pressure cells were installed in the foundation and abutment to monitor the pressure distribution beneath the RSF and within the abutment adjacent to the beam seat. Abutment pressure cells have been utilized by other researchers for both laboratory and field projects to investigate the induced pressure by live and dead loads on abutments (e.g., Abu-Hejleh et al. 2003, Warren et al. 2010, Vennapusa et al. 2012, Iwamoto 2014, Lawrence 2014, Zhang et al. 2016). The pressure distribution in the abutment and its effect on the deformations, lateral pressure, force(s) in the geotextile(s), and pullout resistance has also been evaluated in these studies.

The effect of temperature on vibrating wire pressure cells has been examined by numerous researchers as the pressure inside the cells is affected by the behavior of the fluid inside of it, and any temperature increase/decrease causes the fluid to expand/contract thus generating a change in measured pressure (Weiler and Kulhawy 1982, Dunnicliff and Green 1988, Dunnicliff 1997, Sellers 2000, Yang et al. 2001, Daigle and Zhao 2004, and Huntley and Valsangkar 2016). Ultimately, it was concluded that all utilized vibrating wire pressure cells need to be calibrated for temperature change effects since each cell is unique. Developing an accurate methodology for correcting measured pressure values for temperature is not straightforward because it depends on both the nature of the cell itself as well as the condition in the field that the cell is installed in. This means that every vibrating wire pressure cell has to be calibrated in the field after installation over the range of expected temperature values. For many field projects that are under a tight time deadline, this is not practical.

According to additional literature, air temperature changes induce expansion and contraction of the bridge superstructure, which presents another challenge in interpreting the data from the vibrating wire pressure cells (Abu-Hejleh et al. 2002 and 2006, Puppala et al. 2009, Lawrence 2014, Warren et al. 2014, Tatsuoka et al. 2016). This expansion and contraction changes the pressure between the bridge and the integrated abutment as the bridge moves into and away from the abutment; this issue has been reported by several studies on integral bridge abutments (Abu-Hejleh et al. 2006, Efretuei 2013, Horvath 2005, Puppala et al. 2009). There is more limited experience with this behavior for GRS-IBS structures. The GRS-IBS study conducted by Warren et al. (2010) concluded that the bridge expansion induced by increases in ambient temperature increased the lateral pressure between the bridge and the abutment and decreased the abutment vertical pressure. After 3.5 years of monitoring, it was concluded that the integrated approach of

the GRS-IBS was flexible and moved successfully with thermally induced superstructure deformations; the GRS approach remained engaged with the superstructure as it expanded and contracted during seasonal temperature changes (Warren et al. 2014). Lawrence (2014) reported with an increase in the ambient temperature, the vertical pressure on the installed pressure cells beneath the bridge footing decreased and vice versa for a decrease in the ambient temperature.

3.2.1 Inclinometer Sensors

As shown in Figure 3.1, the four in-place inclinometer (IPI) sensors were installed beneath the RSF of the west abutment in the clay foundation; the IPI sensors were placed in this layer to measure its displacement during construction and over the monitoring periods of the structure. Beneath the clay layer was a relatively stiff sandy layer so the inclinometer casing was terminated in the sandy soil. The inclinometer boreholes were drilled before the existing bridge was demolished as it was determined that drilling after removal of the existing bridge would have been too time consuming and difficult given the site foundation conditions. The inclinometer holes and its casing were left in place during the excavation and the sensors were installed once the excavation reached the base elevation for new construction to take place. By employing a fixed chain of sensors affixed to a series of connected rods, the IPI sensors provide an in-place alternative to traditional traversing probe-type inclinometers. Displacements were measured in both the N-S and E-W directions since vertical biaxial IPIs were used. Figures 3.2 and 3.3 show a typical IPI sensor used in the project and installation of the IPI array in the field, respectively.

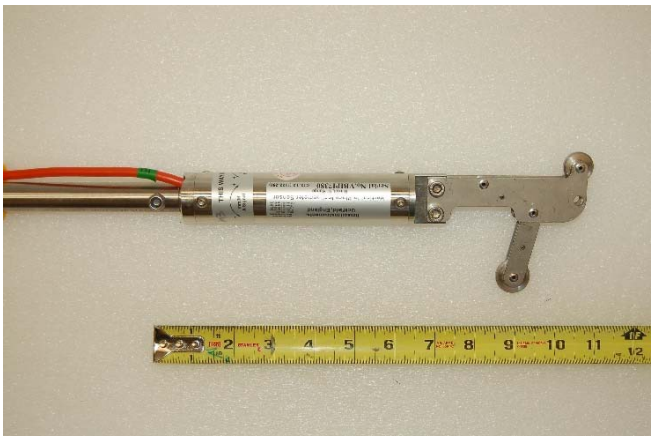

Figure 3.2 In-place inclinometer (IPI) sensor

Figure 3.3 IPI sensor array installation

3.2.2 Piezometers

To measure pore water pressure in the clay foundation three vibrating wire piezometers were installed. As shown in Figure 3.1, two piezometers were installed beneath the RSF of the west abutment and one was installed within the abutment, closer to the bottom. The piezometer within the abutment was not only used to measure water pressure but it was also used to determine the water elevation within the abutments. The borehole used for the piezometers was the same borehole for the IPI sensors mentioned in the previous section and the casing was used to protect the cables down to the foundation elevation during excavation. The piezometers are able to record

pressures from 0-300 kPa. Figures 3.4 and 3.5 show a typical piezometer sensor utilized in this project and its installation, respectively.

Figure 3.4 Piezometer sensor

Figure 3.5 Piezometer sensor installation

3.2.3 Pressure Cells

Figure 3.1 displays the respective locations of the eight total pressure cells that were utilized in this project (four beneath the RSF, three within the west abutment, and one in-between the end of the concrete bridge and the integration zone). The four pressure cells located beneath the RSF measure the static pressure and its distribution beneath the RSF. The three pressure cells

installed within the abutment have the capability to measure both static and "instantaneous" pressure produced by live load on the road; this is possible in this case because a foil-based strain sensor is utilized within these total pressure cells to measure fluid pressure. For the instantaneous pressure measurements to be accurate, they must be made with a data logger that is capable of taking readings at a high rate of data acquisition; the datalogger used in the current study was a budget model that did not have this capability. The pressure cell between the concrete bridge and the integration zone measures the horizontal stress induced by loads and temperature-induced changes on the bridge deck. The pressure range for these cells are similar to that of the piezometers, 0-300 kPa. During installation, sand bags were used to provide a flat surface around the cells to prevent stress concentrations from forming at the sensor location. Figures 3.6 and 3.7 display a typical utilized pressure cell and its installation, respectively.

Figure 3.6 Pressure cell

Figure 3.7 Pressure cell installation

3.2.4 Strain Gauges

A total of 110 strain gauges were utilized in this project, with 50 strain gauges installed in each abutment to monitor the strain in the geotextile, and 10 strain gauges installed on the underside of the bridge beams to monitor the response of the concrete superstructure; for locations of each strain gauge see Figure 3.1. The strain gauges that were utilized were provided by Micro-Measurements. Two different types of strain gauges, long (EA-06-20CBW-120) and short (EP-08-250BG-120), were used in this project and one of each was placed at each location of interest; Figures 3.8a and 3.8b provide sample photos of the long and short strain gauges, respectively, following the gauge attachment processes that were used for each type of sensor.

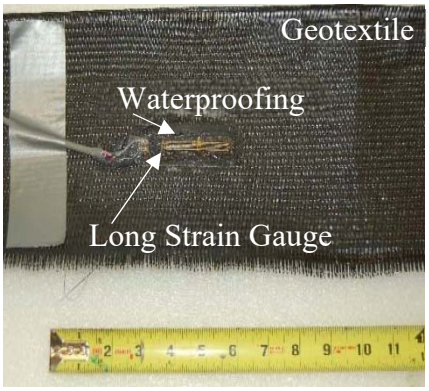

Figure 3.8a Long strain gauge

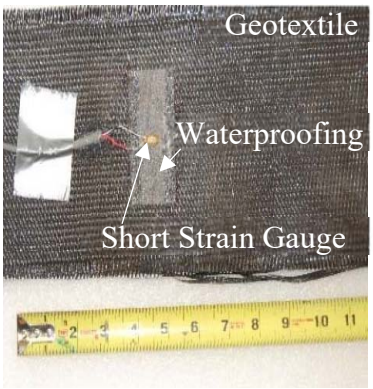

Figure 3.8b Short strain gauge

Two different gauge attachment techniques (Lechchinsky and Fowler 1990, Wu et al. 2013) were utilized in conjunction with the two different sized strain gauges. This gauge layout was intentional, as one of the goals of this instrumentation plan was to assess the effect of the strain gauge installation methodology on the resulting strain readings; more details regarding the strain gauge attachment techniques utilized in this project can be found in Talebi (2016). The strain gauges were installed on the geotextile, waterproofed, and wired in the University of Delaware lab prior to construction and installation. The strain gauges were protected from the granular fill material by placing sand above and below each sensor area. Using this installation process, all

strain gauges survived the GRS-IBS construction process in the field. Figure 3.9 shows the strain gauge wiring that was performed in the University of Delaware laboratory before installation, while Figure 3.10 shows the gauge installation and protection at the site.

Figure 3.9 Strain gauge wiring in the University of Delaware lab prior to site installation

Figure 3.10 Strain gauge protection and installation at the site

3.2.5 Thermistors

A total of 50 thermistors were utilized for this project to monitor the effect temperature has on the GRS-IBS structure, and on the measured strains in the geotextile. As Figure 3.1 shows, the thermistors were placed in the same location as the strain gauges (25 in each abutment); each

thermistor was placed between the long and short strain gauges on the geotextile. The thermistors were provided by Therm-x, the YSI 55000 series. To protect the thermistors against the presence of water in the abutment, the thermistors were waterproofed prior to their installation; more details regarding the thermistor waterproofing process can be found in Talebi (2016). Figures 3.11 and 3.12 display a typical waterproofed thermistor and its installation.

Figure 3.11 Thermistor

Figure 3.12 Thermistor installation

3.2.6 Volumetric Water Content Sensors

Five volumetric water content sensors (MAS-1) provided by Decagon were utilized in this project. They were installed at different elevations within the west abutment, as shown in Figure 3.1, to monitor soil moisture content and its effect on the strains in the geotextile. The use of these

sensors also makes it possible to investigate the effect of increase in water content due to precipitation or changes in the river elevation on the structure's behavior. Figure 3.13 displays a typical volumetric water content sensor that was utilized for this project.

Figure 3.13 Volumetric water content sensor

3.2.7 Surveying Targets

Surveying targets were installed on each abutment facing wall to monitor facing wall settlement and lateral deflection during in-service operation of the GRS-IBS. Fifteen targets were installed on each abutment facing wall; targets were installed at three different elevations with five targets at each elevation spanning the width of the abutment facing wall. Surveying data was collected on a weekly basis for the first two months of the project to ensure no significant displacements were occurring. After this, data was collected monthly for approximately the following year. Data was then collected bi-monthly for the year after that, and bi-annually for the year after that. As time went on, it was concluded that the structure was not moving significantly so surveying was performed less frequently. The relative accuracy of measurements for the surveying approach that was used in this study was approximately 6 mm. Figure 3.14 shows the surveying points on the east abutment facing wall; the surveying points are located in the same positions on the west abutment facing wall.

Figure 3.14 East abutment facing wall surveying points

3.3 Data Collection Process

A data logging system provided by itmsoil USA was utilized for data collection in the west GRS-IBS abutment. The first logger in the data logging system consists of the following: one CR1000 data logging and control module, one AVW200 vibrating wiring sensor interface, one PS100 power supply, three BCM-1 bridge completion modules, six AM16/32 multiplexers, and two 16” x 16” GRP enclosures. Different multiplexer configurations were employed based on the types of readings being taken from various sensors. This logger collected inclinometer, piezometer, static pressure cell, and strain gauge data. The second logger in the data logging system consists of one CR800 data logging and control module and three AM16/32 multiplexers installed in one 16” x 16” GRP enclosure. Thermistor, dynamic pressure cell, and volumetric water content sensor data was collected by this logger.

The loggers are programmed with CRBasic and the source of the logger program, named Logger1 CR1000.CR1, is supplied on the USB drive; it is viewable with an ASCII editor. Logger

1 had the program already loaded into it by itmsoil USA. To send the program to the logger, the PC200W program provided by itmsoil USA was used. Figure 3.15 and 3.16 display the loggers.

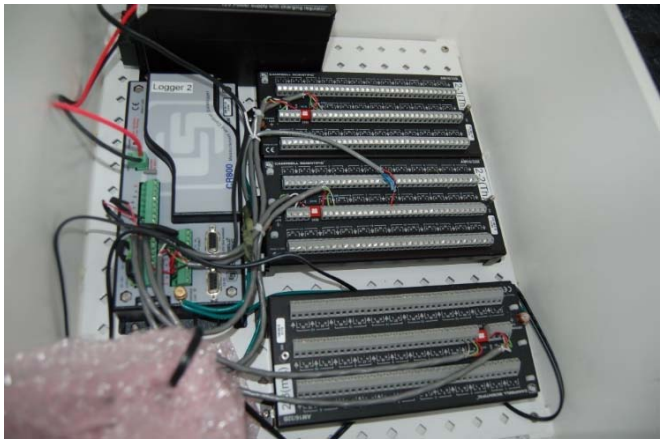

Figure 3.15 CR800 logger

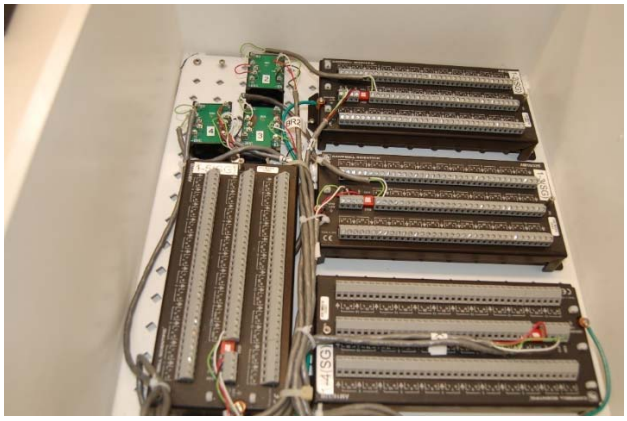

Figure 3.16 CR1000 logger

For this abutment, sensor data was recorded simultaneously for all sensors every 10 minutes using the loggers. Using such a short time interval for data collection ensured that high quality data was collected and that data for specific events, such as heavy rainfall or a rapid increase in river water level, would be available. By recording data every 10 minutes, a large dataset was collected over the length of the previous monitoring period and this current monitoring period, over four years total. Given the size of the data set, it was somewhat difficult to manually manage and analyze the data. As a result, the data was managed and analyzed using the R

programming language. Chapter 5 of Talebi (2016) discusses, in depth, the techniques used to manage and filter the large amounts of data that were recorded using the R program.

For the east GRS-IBS abutment, two rotary data switches manufactured by Omega (OSWG5-40) were utilized for the data collection of the 75 installed sensors (Figure 3.17). From these rotary switches, raw data was collected manually approximately every two weeks over the course of each monitoring period. A multimeter was used to collect this data as the raw data was outputted in ohms and the data was later converted to engineering units.

Figure 3.17 Front and back view of rotary data switches

References

AASHTO (2014). "AASHTO LRFD bridge design specifications." 7th ed. Washington, DC: American Association of State Highway and Transportation Officials

Abu-Hejleh, N., Hanneman, D., White, D., Wang, T. and Ksouri, I. (2006). "Flowfill and MSE Bridge Approaches: Performance, Coast, and Recommendations for Improvements (No. CDOT-DTD-R-2006-2)." Colorado Department of Transportation, Research Branch.

Abu-Hejleh, N., Wang, T., and Zornberg, J. (2001). "Performance of geosynthetic-reinforced walls supporting bridge and approaching roadway structures." In GeoDenver 2000 Congress.

Abu-Hejleh, N., Zornberg, J., Elias, V., and Watcharamonthein, J. (2003). "Design assessment of the founders/meadows GRS abutment structure." In Proc., 82nd Annual TRB Meeting.

Abu-Hejleh, N., Zornberg, J., Wang, T., and Watcharamonthein, J. (2002). "Monitored displacement of unique geosynthetic-reinforced soil bridge abutments." Geosynthetics International, 9 (1), 71–95.

Adams, M., Schlatter, W., and Stabile, T. (2007). "Geosynthetic-reinforced soil integrated abutments at the bowman road bridge in defiance county, Ohio." Proceedings, Geo-Denver, 1-11.

Buttry, K., McCullough, E., and Wetzel, R. (1996). "Temperatures and related behavior in segmental retaining wall system." Transportation Research Record: Journal of the Transportation Research Board, (1534), 19-23.

Daigle, L. and Zhao, J. (2004). "The influence of temperature on earth pressure cell readings." Canadian geotechnical journal, 41(3), 551-559.

Dunnicliff, J. (1997). "Temperature sensitivity of earth pressure cells." Geotechnical Instrumentation News, 15(2): 42.

Dunnicliff, J. and Green, G. (1988). "Geotechnical instrumentation for monitoring field performance." John Wiley & Sons, Inc., New York.

Efretuei, E. (2013). "Thermal impact on soil-structure interaction for integral bridges." University of Leeds.

Esmaili, D., Hatami, K., and Miller, G. (2014). "Influence of matric suction on geotextile reinforcement-marginal soil interface strength." Geotextiles and Geomembranes, 42(2), 139-153.

FHWA (2009). "Mechanically stabilized earth walls and reinforced soil slopes design and construction guidelines". Volume I, publication No. FHWANHI-10-025.

Fredlund, D. G., Morgenstern, N. R., and Widger, R. A. (1978). "The shear strength of unsaturated soils." Canadian geotechnical journal, 15(3), 313-321.

Helwany, S., Wu, J., and Froessl, B. (2003). "GRS bridge abutments—an effective means to alleviate bridge approach settlement." Geotextiles and Geomembranes, 21(3), 177-196.

Horvath, J. (2005). "Integral-abutment bridges: geotechnical problems and solutions using geosynthetics and ground improvement." In West Virginia University.

Huntley, S. and Valsangkar, A. (2016). "Laboratory thermal calibration of contact pressure cells installed on integral bridge abutments." Canadian Geotechnical Journal, 53(6), 1013-1025.

Iwamoto, M. (2014). "Observations from load tests on geosynthetic reinforced soil". Doctoral dissertation, University of Hawaii.

Jiang, Y., Han, J., Parsons, R., and Brennan, J. (2016). "Field Instrumentation and Evaluation of Modular-Block MSE Walls with Secondary Geogrid Layers." Journal of Geotechnical and Geoenvironmental Engineering, 05016002.

Kim, W. and Borden, R. (2013). "Numerical simulation of MSE wall behavior induced by surface-water infiltration." Journal of Geotechnical and Geoenvironmental Engineering, 139(12), 2110-2124.

Lawrence, J. (2014). "Structural health monitoring of the first geosynthetic reinforced soil--integrated bridge system in Hawaii." Doctoral dissertation, University of Hawaii at Manoa.

Leshchinsky D. and Tatsuoka F. (2013). "Performance, design, and redundancy, geosynthetic reinforced walls in the public sector." Geosynthetics 31(3), 12–21.

Leshchinsky, D. (2009). "On global equilibrium in design of geosynthetic reinforced wall." Journal of Geotechnical and Geoenvironmental Engineering, 135(3), 309–15

Leshchinsky, D. and Fowler, J. (1990). "Laboratory measurement of load-elongation relationship of high-strength geotextiles" Geotextiles and Geomembranes, 9(2), 145- 164.

Miyata, Y., Bathurst, R., and Miyatake, H. (2015). "Performance of three geogrid-reinforced soil walls before and after foundation failure." Geosynthetics International, 22(4), 311-326.

Ng C. and Pang Y. (2000). "Influence of stress state on soil–water characteristics and slope stability." Journal of Geotechnical and Geoenvironmental Engineering, 126(2), 157–66

Nicks, J., Esmaili, D., and Adams, M. (2016). "Deformations of geosynthetic reinforced soil under bridge service loads." Geotextiles and Geomembranes, 44(4), 641-653.

Portelinha, F., Bueno, B., and Zornberg, J. (2013). "Performance of nonwoven geotextile-reinforced walls under wetting conditions: laboratory and field investigations." Geosynthetic International, 20(2), 90–104.

Puppala, A., Saride, S., Archeewa, E., Hoyos, L., and Nazarian, S. (2009). "Recommendations for design, construction, and maintenance of bridge approach slabs: Synthesis report." Rep. No. FHWA/TX-09/6022, 1.

Santos, E., Palmeira, E., and Bathurst, R. (2013). "Behaviour of a geogrid reinforced wall built with recycled construction and demolition waste backfill on a collapsible foundation." Geotextiles and Geomembranes, 39, 9-19.

Santos, E., Palmeira, E., and Bathurst, R. (2014). "Performance of two geosynthetic reinforced walls with recycled construction waste backfill and constructed on collapsible ground." Geosynthetics International, 21(4), 256-269.

Sellers, B. (2000). "Temperature effects on earth pressure and concrete stress cells – some theoretical considerations." Geotechnical Instrumentation News, 18(1), 23–24.

Skinner, G.D. and Rowe R.K. (2005). "A novel approach to estimating the bearing capacity stability of geosynthetic reinforced retaining walls constructed on yielding foundations." Canadian Geotechnical Journal, 42(3), 763-779.

Talebi, M. (2016). "Analysis of the field behavior of a geosynthetic reinforced soil integrated bridge system during construction and operation", PhD Dissertation, University of Delaware, 2016.

Tatsuoka, F., Tateyama, M., Koda, M., Kojima, K., Yonezawa, T., Shindo, Y., and Tamai, S. (2016). "Recent research and practice of GRS integral bridges for railways in Japan." Japanese Geotechnical Society Special Publication, 2(68), 2307-2312.

Vahedifard, F., Leshchinsky, B., Mortezaei, K., and Lu, N. (2015). "Active earth pressures for unsaturated retaining structures." Journal of Geotechnical and Geoenvironmental Engineering, 141(11), 04015048.

Vennapusa, P., White, D., Klaiber, F., Wang, S., and Gieselman, H. (2012). "Geosynthetic reinforced soil for low-volume bridge abutments."

Warren, K. A., Schlatter, W., Adams, M., Stabile, T., and LeGrand, D. (2010). "Preliminary Results for a GRS Integrated Bridge System Supporting a Large Single Span Bridge." In Earth Retention Conference 3, 612-619.

Warren, K., Whelan, M., Hite, J., and Adams, M. (2014). "Three-Year Evaluation of Thermally Induced Strain and Corresponding Lateral End Pressures for a GRS IBS in Ohio." In Geo-Congress 2014 Technical Papers: Geo-characterization and Modeling for Sustainability, 4238-4251

Weiler, W. and Kulhawy, F. (1982). “Factors affecting cell stress measurements in soil. Journal of the Geotechnical Engineering Division.” ASCE, 108(GT12), 1529–1548.

Wu, J. (2006). “Design and construction guidelines for geosynthetic-reinforced soil bridge abutments with a flexible facing.” Transportation Research Board.

Wu, J., Ketchart, K., and Adams, M. (2008). “Two full-scale loading experiments of geosynthetic-reinforced soil (GRS) abutment wall. International Journal of Geotechnical Engineering.”

Wu, J., Nicks, J., Pham, T., and Adams, M. (2013). “Composite Behavior of Geosynthetic Reinforced Soil Mass”, Federal Highway Administration, Publication No. FHWA-HRT-10-077, Washington, DC.

Yang, K., Utomo, P., and Liu, T. (2013). “Evaluation of force-equilibrium and deformation-based design approaches for predicting reinforcement loads within geosynthetic-reinforced soil structures.” Journal of GeoEngineering, 8(2), 41-54.

Yang, M., Drumm, E., Bennett, R., and Mauldon, M. (2001). “Temperature effects on contact earth pressure cells: inferences from long term field instrumentation.” Geotechnical Instrumentation News, 19(2), 25–28.

Yoo, C. (2013). “Effect of rainfall on performance of geosynthetic reinforced soil wall using stress-pore pressure coupled analysis.” In Geo-Congress 2013: Stability and Performance of Slopes and Embankments III, 566-573).

Yoo, C. and Jung, H. (2006). “Case history of geosynthetic reinforced segmental retaining wall failure.” Journal of Geotechnical and Geoenvironmental Engineering, 132(12), 1538-1548.

Zhang, J., Zheng, J., Zhao, D., and Chen, S. (2016). “Field study on performance of new technique of geosynthetic-reinforced and pile-supported embankment at bridge approach.” Science China Technological Sciences, 59(1), 162-174.

Chapter 4

Findings

4.1 Introduction

Different types of instruments were installed in the GRS-IBS abutments including inclinometers, piezometers, total pressure cells, strain gauges, thermistors, volumetric water content sensors, and surveying targets; sensor location, installation, and purpose were described in Chapter 3. These instruments were used to monitor the GRS-IBS structure response during construction, live load testing, and two different operational monitoring periods; the first operational monitoring period was from May 29, 2013 through August 31, 2016 and the second was from September 1, 2016 through August 31, 2017 (this monitoring period will be referred to in this report as the current monitoring period). The purpose of this chapter is to present all the data recorded during construction, live load testing, and both operational monitoring periods while also investigating and comparing the data from the most recent monitoring period to the past monitoring period.

4.2 Analysis of the Collected Data

As previously mentioned, the measured data for each sensor during the construction phase, live load testing, and both operational monitoring periods will be presented in the following sections with emphasis on comparing the data from the most recent monitoring period with data from the prior monitoring periods. In depth details about data collected during construction, live load testing, and the first monitoring period can be found in Talebi (2016). It should be noted that

the grey line within the operational plots at September 1, 2016 represents the separation between the two monitoring periods.

4.2.1 Volumetric Water Content and Pore Water Pressure

Five volumetric water content sensors were installed at different elevations in the west abutment to measure the change in moisture content within the abutment over time. As discussed in Chapter 3, the use of these sensors also makes it possible to investigate the effect of increases in water content due to precipitation or changes in the river elevation. Figure 4.1 shows the changes in volumetric water content that occurred during live load testing and both monitoring periods; no data was recorded for these sensors during the construction process.

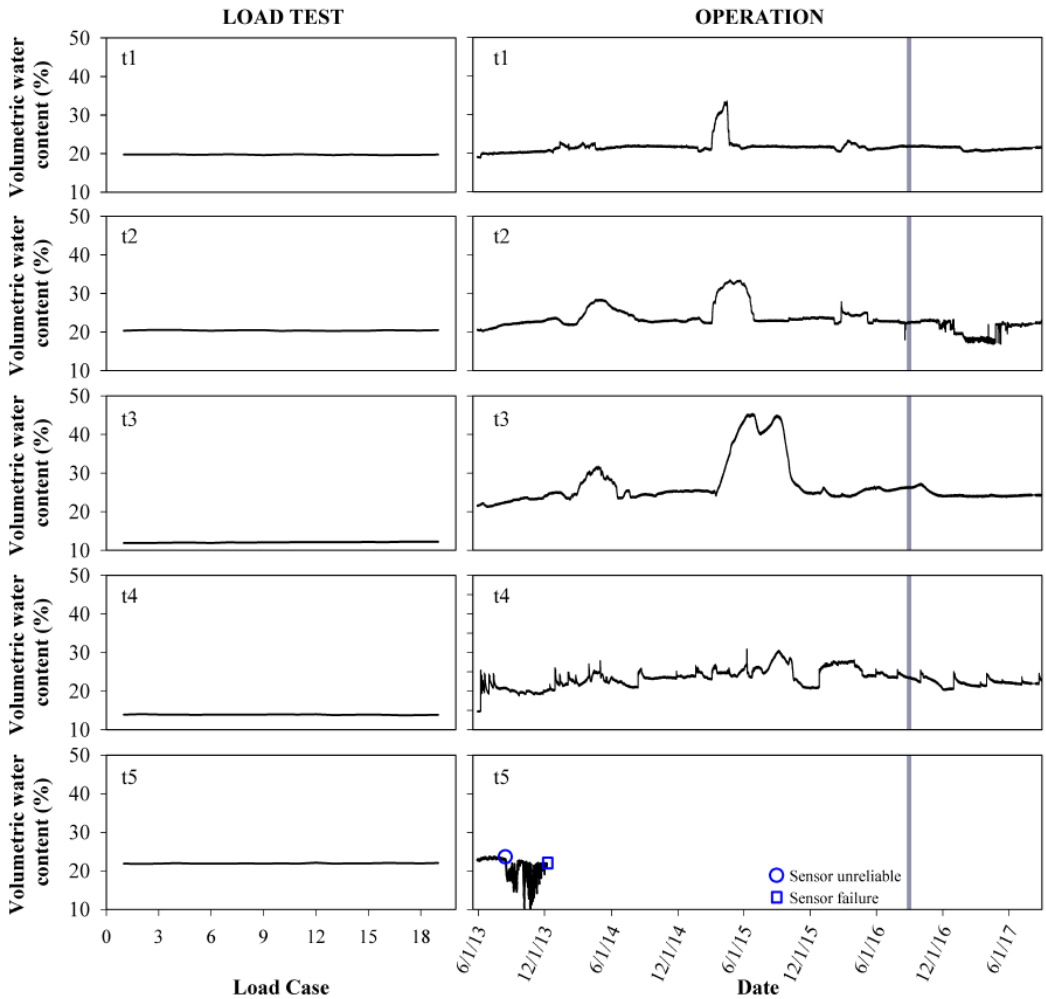

Figure 4.1 Measured volumetric water content

The volumetric water content was constant during live load testing and fairly constant over both monitoring periods; over the course of the two monitoring periods, the moisture content typically ranged from 20-25%. As shown, the lowermost sensor, sensor t5, failed after approximately 3 months of operation. Although the reason for this sensor failure is not clear, this sensor was generally always submerged so it could have failed due to waterproofing issues. Spikes in the water content were seen in the winter and spring of each year; this is expected as Delaware has a generally wet spring. The spike in the second year is considerably higher than other years and this is thought to be from an increased amount of snowfall and the corresponding rate of infiltration since the amount of rainfall precipitation did not significantly vary over both monitoring periods. Talebi (2016) suggested that a slight increase was seen in water content over the first three years of operation and that it should continue to be monitored, however this current monitoring period suggests that the water content within the abutment is steady.

The current monitoring period, September 1, 2016 through August 31, 2017, did not show significant difference in abutment water content as the plots continued to stay rather steady throughout the past year. Histograms for both monitoring periods combined and just the current monitoring period are presented in Figures 4.2 and 4.3 respectively. Water contents between 20 to 25 percent were the most frequent in both figures; both figures also show similar peak values between the same sensors.

Figures 4.4 and 4.5 show the minimum and maximum measured water content values in the west abutment for both monitoring periods combined and just the current monitoring period respectively. The maximum water content occurs at the middle elevation, sensor t3, in both figures. Water content values approximately ranged from 14-46% for both monitoring periods combined but only ranged from about 16-28% for this current monitoring period.

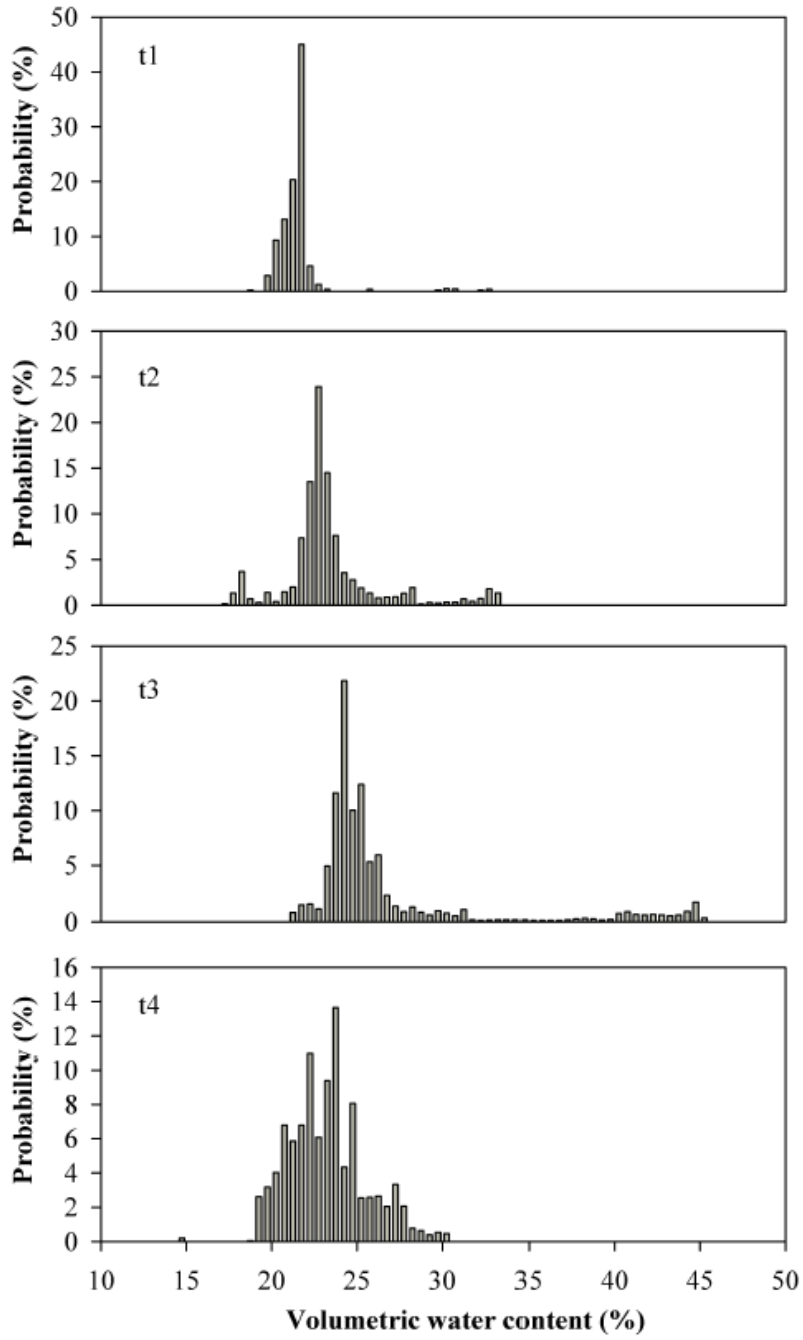

Figure 4.2 Histogram of volumetric water content for both monitoring periods

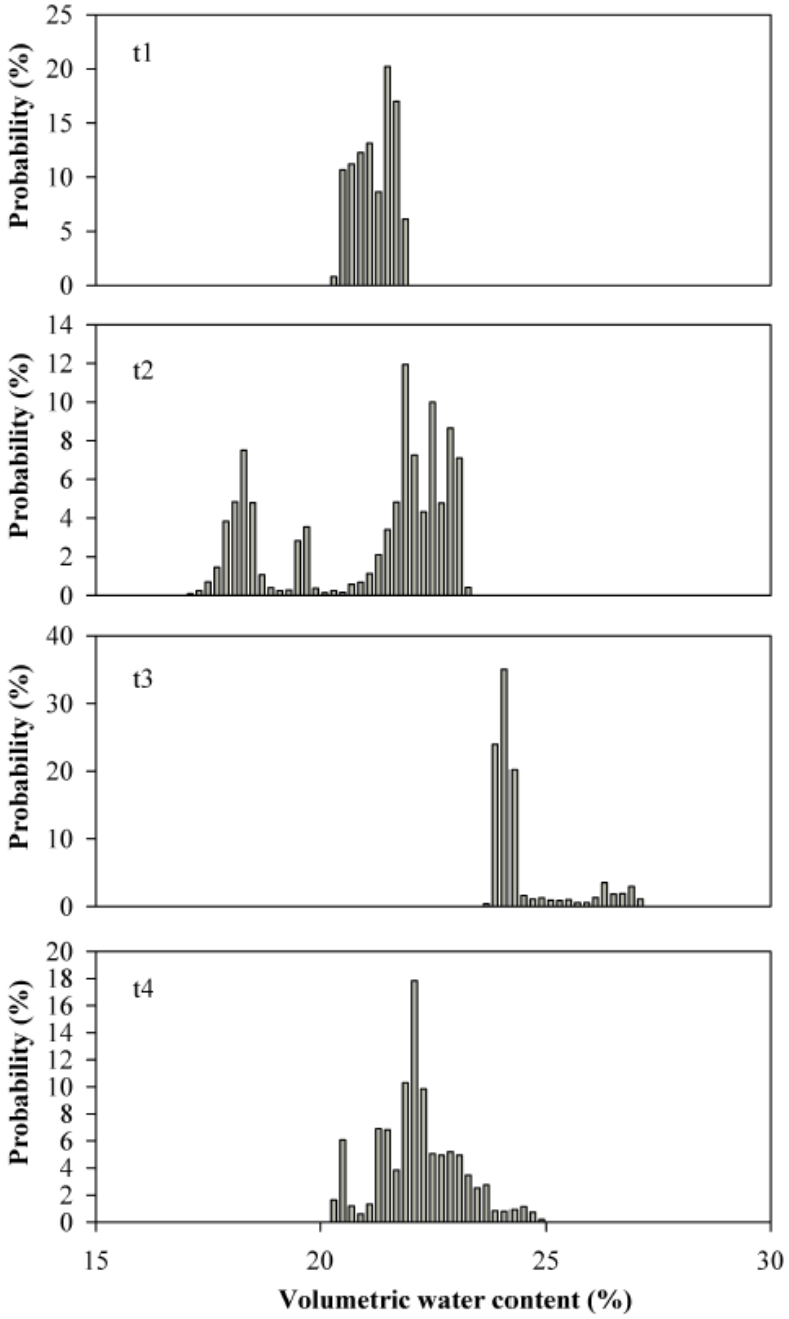

Figure 4.3 Histogram of volumetric water content for the current monitoring period

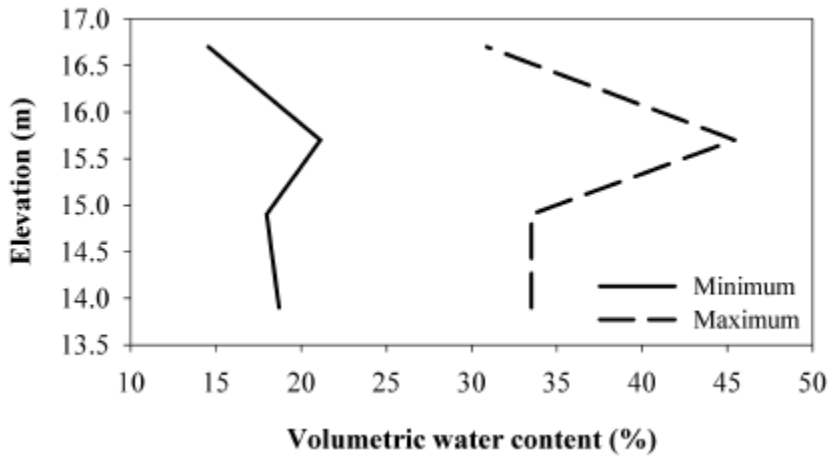

Figure 4.4 Minimum and maximum measured water content profile for both monitoring periods

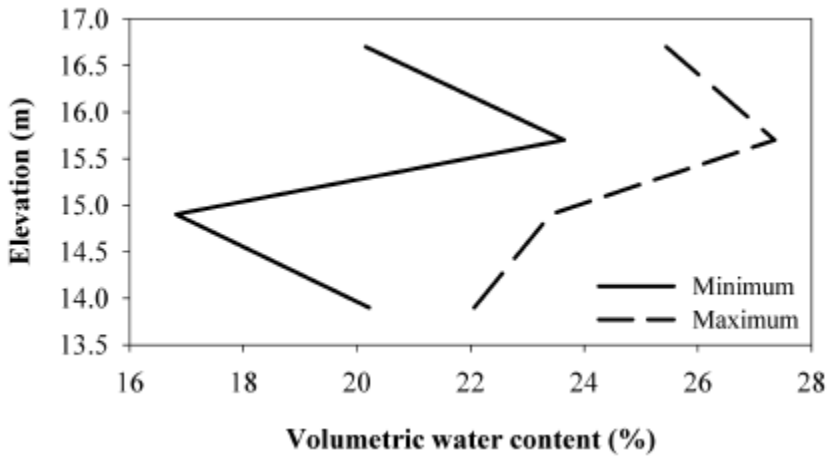

Figure 4.5 Minimum and maximum measured water content profile for the current monitoring period

As discussed in Chapter 3, three vibrating wire piezometers were installed to measure pore water pressure in the clay foundation; two of the piezometers reside beneath the RSF of the west abutment while the other was installed at the bottom of the abutment. This abutment piezometer is also used to determine the river water elevation, as discussed in the previous section. Figure 4.6 presents the measured pore pressures during construction, live load testing, and both monitoring periods. Load-induced changes in pore pressure were seen during construction but no significant changes in pore pressure were seen during the live load testing period. Talebi (2016) states this is

due to the fact that this was a replacement structure so the overall change in loading after unloading and reloading is believed to not be significant. The increase in pore water pressure between the end of construction and the beginning of the live load testing is the result of the river channel beneath the bridge being refilled (Talebi 2016).

As shown, the pore pressure was generally steady over both monitoring periods of operation with spikes in pore pressure at the same time in each sensor. The pore water pressure for the current monitoring period is consistent with what was observed in the previous monitoring period.

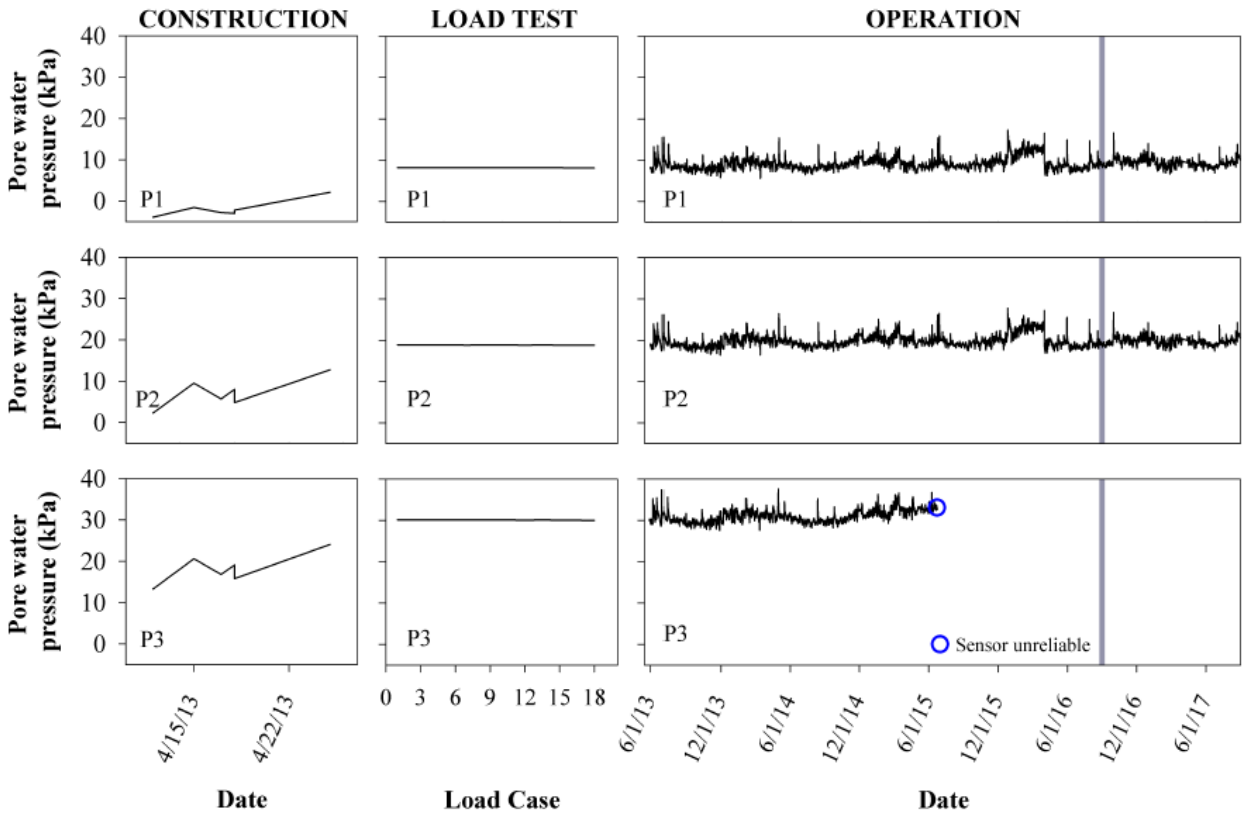

Figure 4.6 Measured pore water pressures

Figure 4.7 displays the daily accumulated precipitation for the location of Bridge 1-366. Figure 4.8 shows the change in river water elevation over both monitoring periods based on piezometer readings. There were no observed differences in the measured precipitation or the river

water elevation between the two monitoring periods. The spikes seen in the measured pore water pressures are consistent with the spikes seen in Figures 4.7 and 4.8, suggesting that storm events or any increase in precipitation affects the river water elevation, as expected, while also increasing the water content within the abutment and the pore water pressure readings. This is directly supported by what is presented in Figures 4.1 and 4.6.

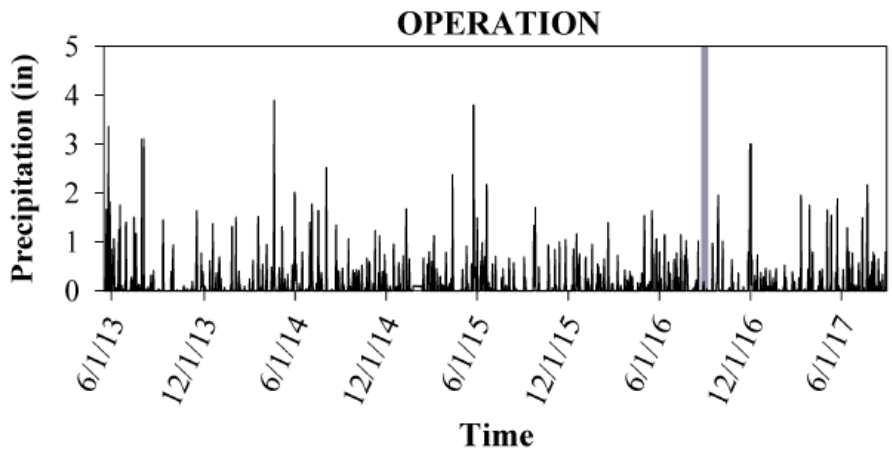

Figure 4.7 Measured precipitation

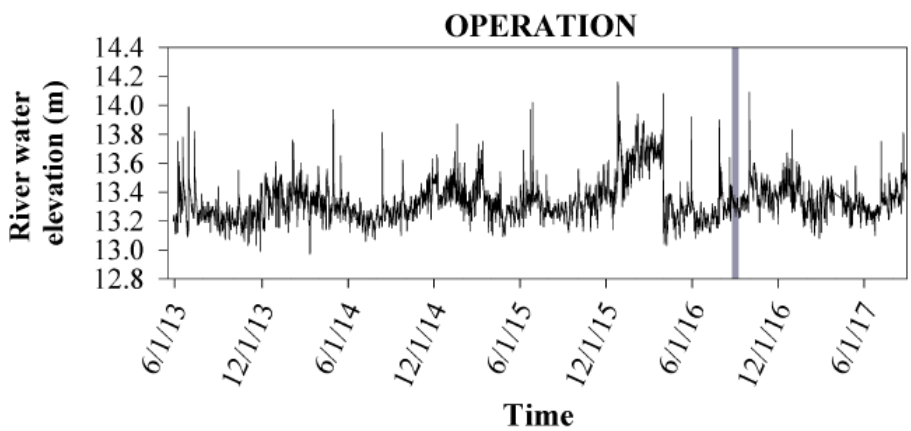

Figure 4.8 Change in river water elevation

Figures 4.9 and 4.10 present histograms for the water elevation in the river for both monitoring periods combined and the current monitoring period respectively. Both figures are very similar with values ranging between 13.0 m and 14.0 m with the most frequency occurring between 13.2 m and 13.6 m.

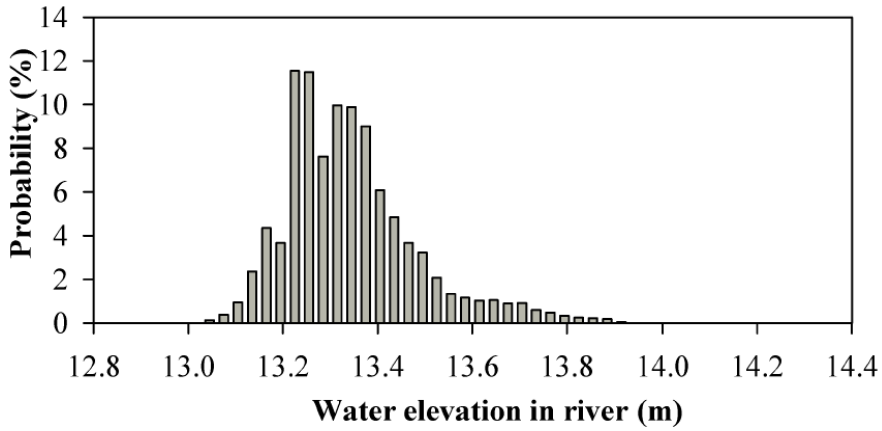

Figure 4.9 Histogram of water elevation in the river for both monitoring periods

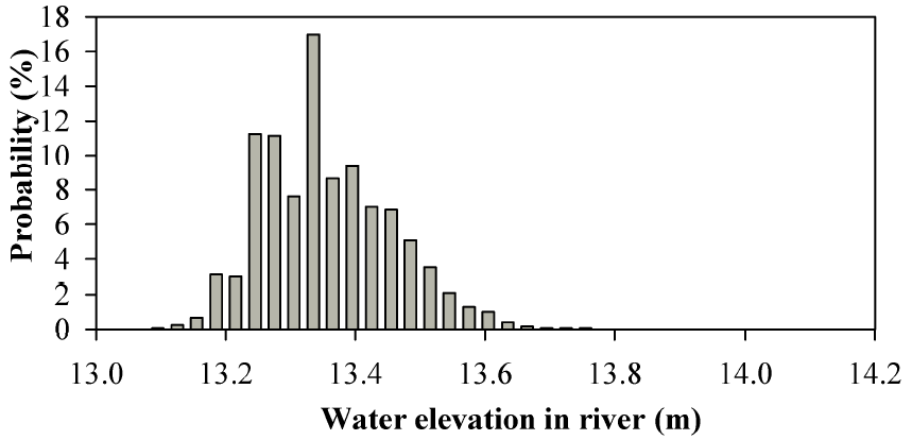

Figure 4.10 Histogram of water elevation in the river for the current monitoring period

As discussed in Talebi (2016), there was not a strong correlation between the water content within the abutment and abutment strain, facing wall deformation, or foundation displacements. It was also stated that there was not a strong correlation between the water level and the deformation of the abutment. At the end of the first monitoring period, it was concluded that the structure's response was not significantly influenced by the abutment water content or the presence of water, internally or externally, but it was suggested that this be reexamined in a year or so. After this current monitoring period it can be concluded again that structure's response was not significantly influenced by the abutment water content or pore water pressure.

4.2.2 Temperature measured by Thermistors

A total of 50 thermistors were installed for this project, 25 in each abutment, as discussed in Chapter 3. These thermistors were installed at the same location as the strain gauges to investigate the effect temperature had on the strain gauge readings. Figure 4.11 presents the recorded thermistor temperatures for the west abutment (layers A through E) during construction, live load testing, and both monitoring periods; Figure 4.12 shows the same except for the east abutment (layers F through J), which were manually collected approximately every two weeks.

The temperature changes in both abutments are very similar, as expected; the seasonal temperature changes in both abutments follow the same trend. Recorded temperatures for layers A and F fall mostly between 10°C and 20°C while temperature for layers E and J range from 0°C and 35°C and have more noise. The larger range in values for layers E and J is because those layers are closer to the ground surface and are more exposed to changes in air temperature. As one moves deeper into the abutment, further from the ground surface and the facing wall, less variation is seen. Sensors closest to the facing wall (A1-F1) see more daily noise since they are most affected by daily, weekly, or monthly changes in ambient temperature changes. The temperature in layers B and G change between 5°C and 20°C while the corresponding values for layers C and H are 0°C and 23°C. Finally, the temperature variation in layers D and I is 0°C and 26°C. It can be seen that this current monitoring period follows the same trend as the first monitoring period.

The majority of the sensors are still working after the last monitoring period, which shows that the initial waterproofing process that was utilized for the thermistors was successful. Sensors A1-th, A-2th, A3-th, C1-th, C4-th, D2-th, G1-th, H2-th, J6-th and J7-th all failed during the first monitoring period. As stated in Talebi (2016), the reason for sensor failure is not clear but it is speculated the presence of water is to blame.

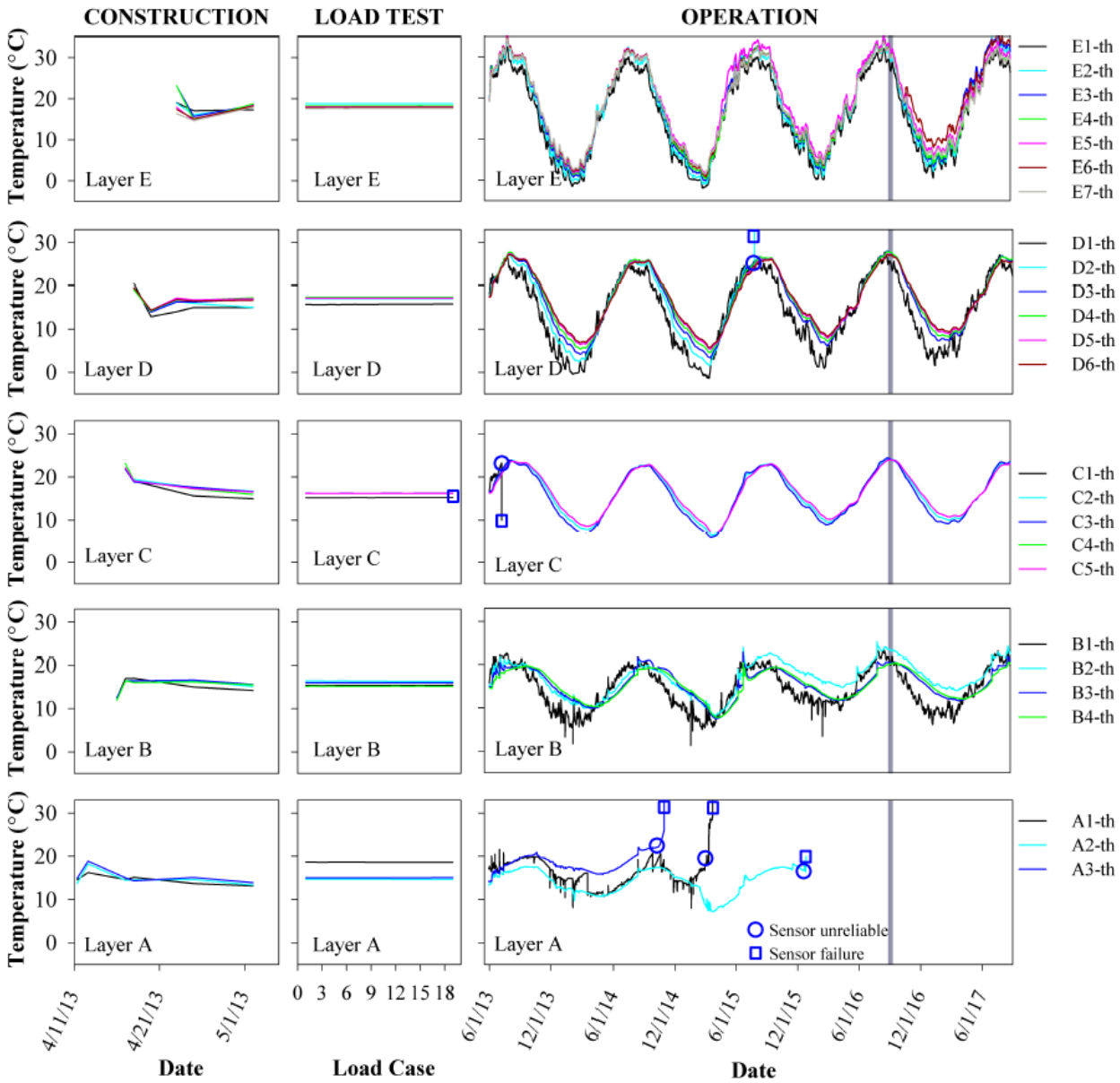

Figure 4.11 Recorded temperatures in the west abutment

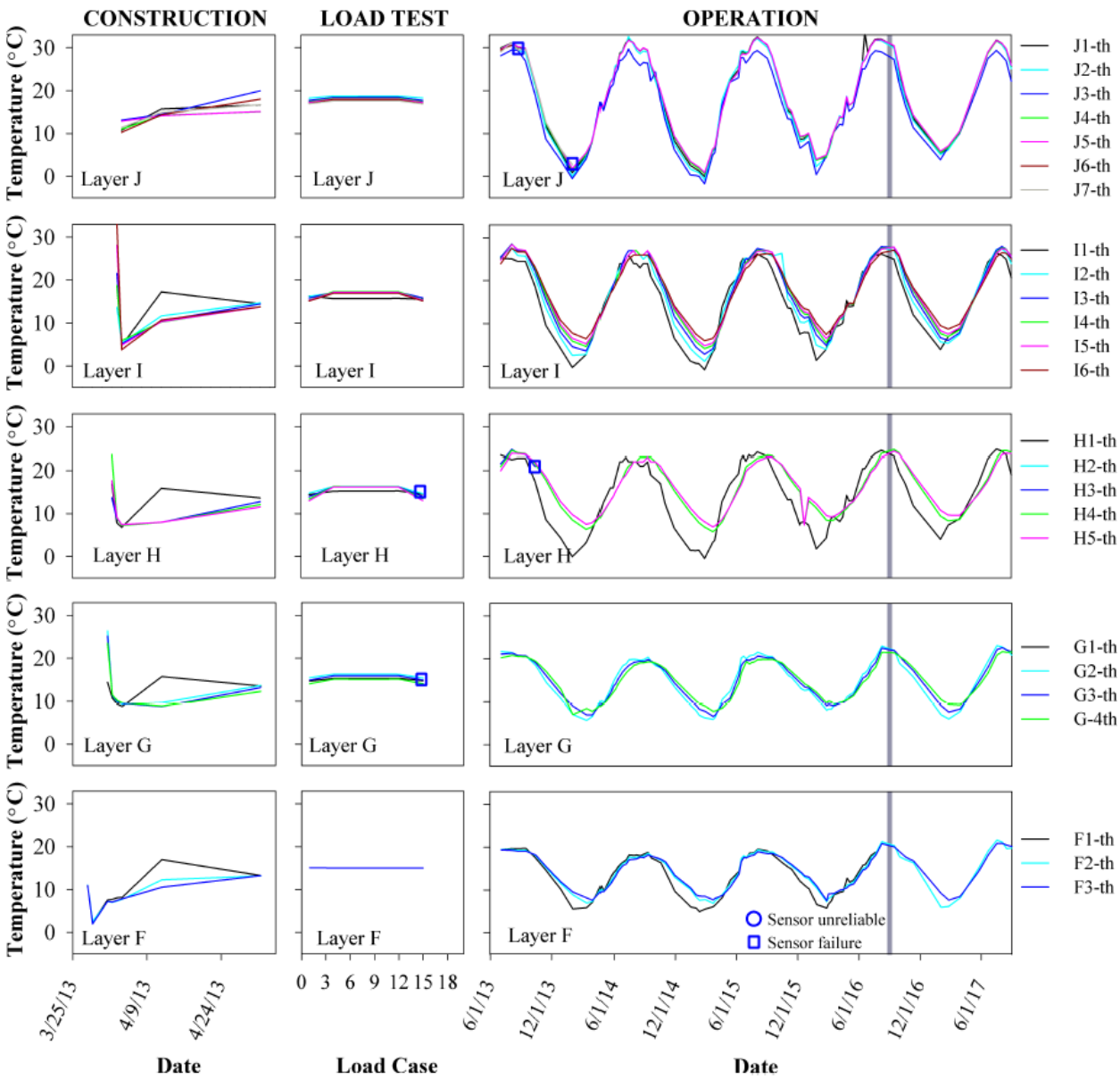

Figure 4.12 Recorded temperatures in the east abutment

Plotting the temperature distribution throughout the GRS-IBS abutments for the current monitoring period proved difficult due to the sensor failure that had occurred over the first monitoring period (particularly in the lower portions of the abutment). Consequently, spatial distribution maps of temperature could not be easily created for the current monitoring period. However, these types of plots are available in Talebi (2016) for the early stages of the first monitoring period when almost all of the thermistors were still functioning properly. What these

contour plots showed was that the daily temperature changes had a negligible effect on temperature changes within the abutment, particularly deeper within the abutment. However, noticeable temperature changes within the abutment can be observed on a month to month basis. In general, it was concluded that on hot days, thermistor readings near the ground surface and facing wall were higher than that of the readings deeper within the abutment. For cold days it was observed that the temperature near the ground surface and the facing wall were much lower than further away.

Figure 4.13 displays the ambient air temperature that was recorded at the datalogger location. It can be seen that the thermistor readings follow the same trend as the ambient air temperature readings but with less noise.

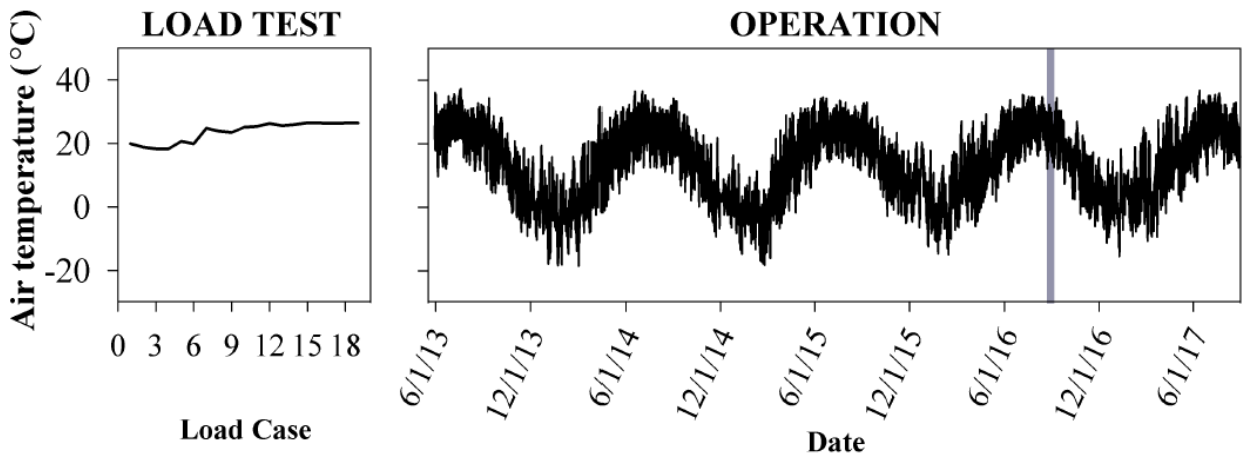

Figure 4.13 Ambient air temperature

4.2.3 Strain in the Abutment Measured by the Strain Gauges

Two different types of strain gauges were utilized in this project to monitor strain in the geotextile. Figures 4.14 and 4.15 show the strain gauge readings in the west abutment during construction, live load testing, and both monitoring periods for the short and long strain gauges, respectively. As shown, all strain readings of properly working gauges were less than 0.5%. It can also be observed that the strain readings follow the same pattern as the temperature readings produced by the thermistors. As explained in Talebi (2016), there is a clear effect of temperature on strain gauge readings and it should be corrected for. A detailed method for correcting field strain measurements to account for temperature effects is presented in Meehan and Talebi (2017). The resulting corrected strains for each short strain gauge and each long strain gauge in the west abutment are presented in Figures 4.16 and 4.17 respectively; plots for C1-s and C3-s are not presented since they stopped working during the live load testing. From these figures, it can be observed that the estimated amount of creep from the start of the first monitoring period to the end of this current monitoring period was generally less than 0.1%.

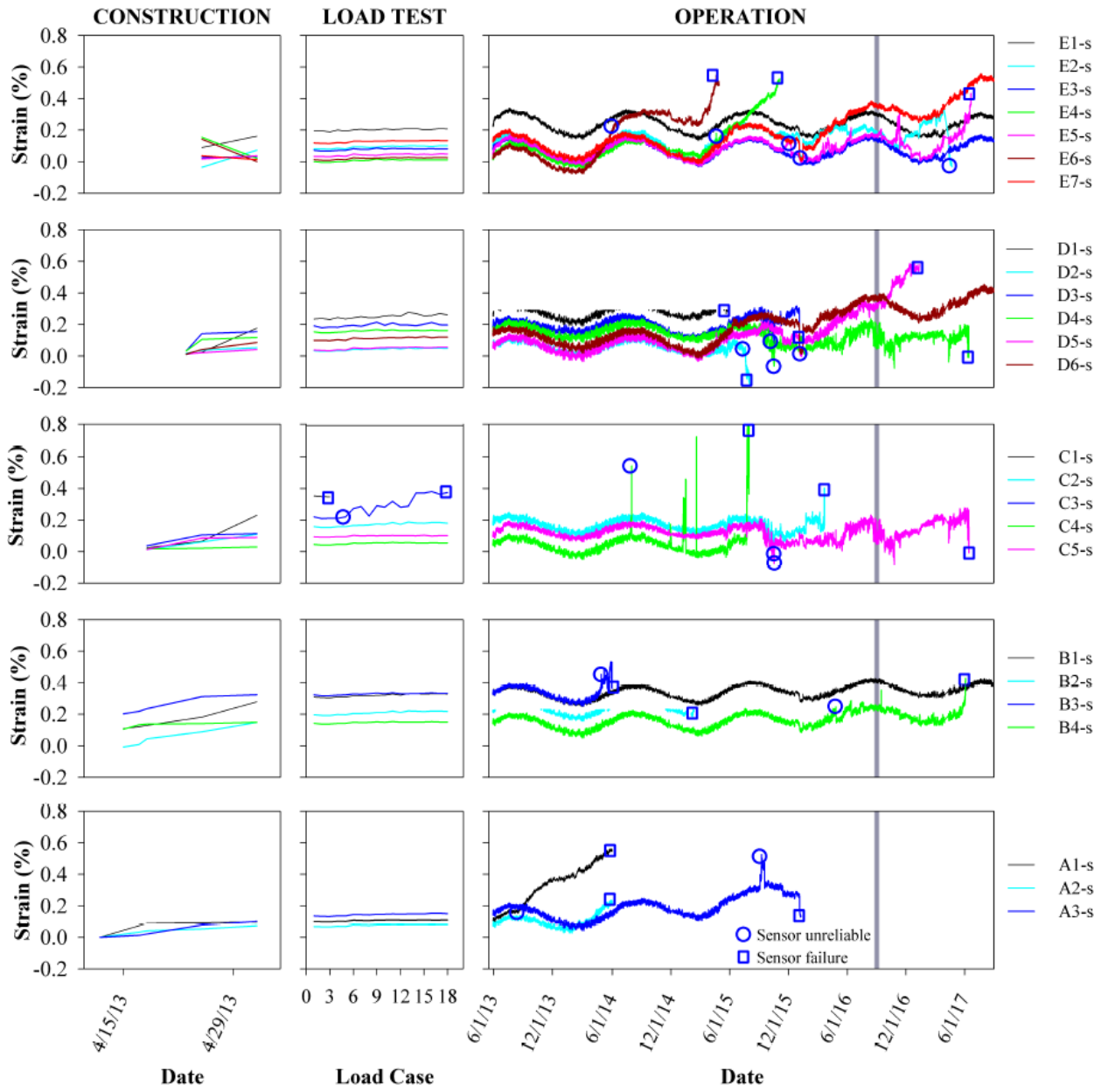

Figure 4.14 West abutment short strain gauge readings (uncorrected)

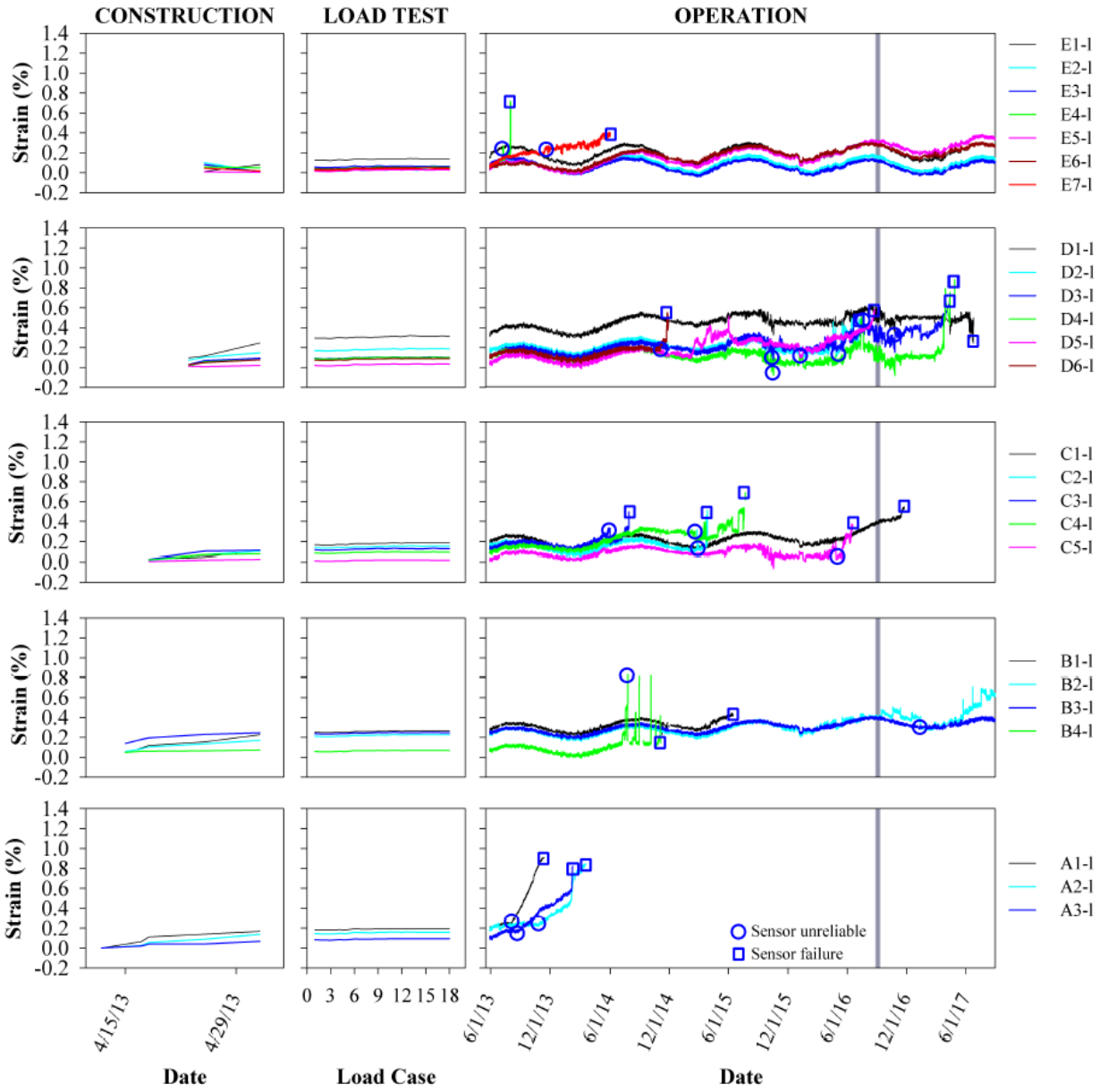

Figure 4.15 West abutment long strain gauge readings (uncorrected)

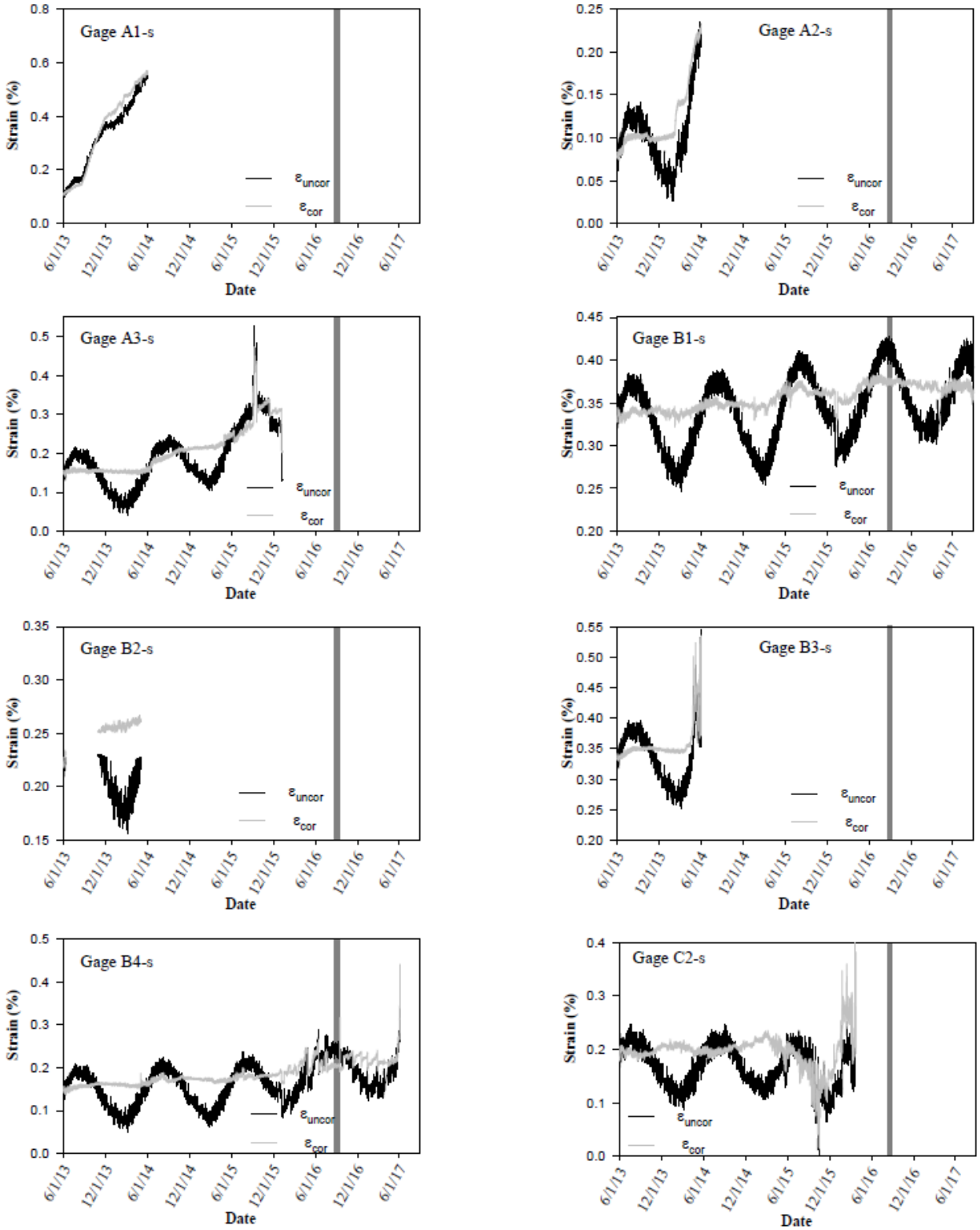

Figure 4.16 West abutment short strain gauge readings (corrected)

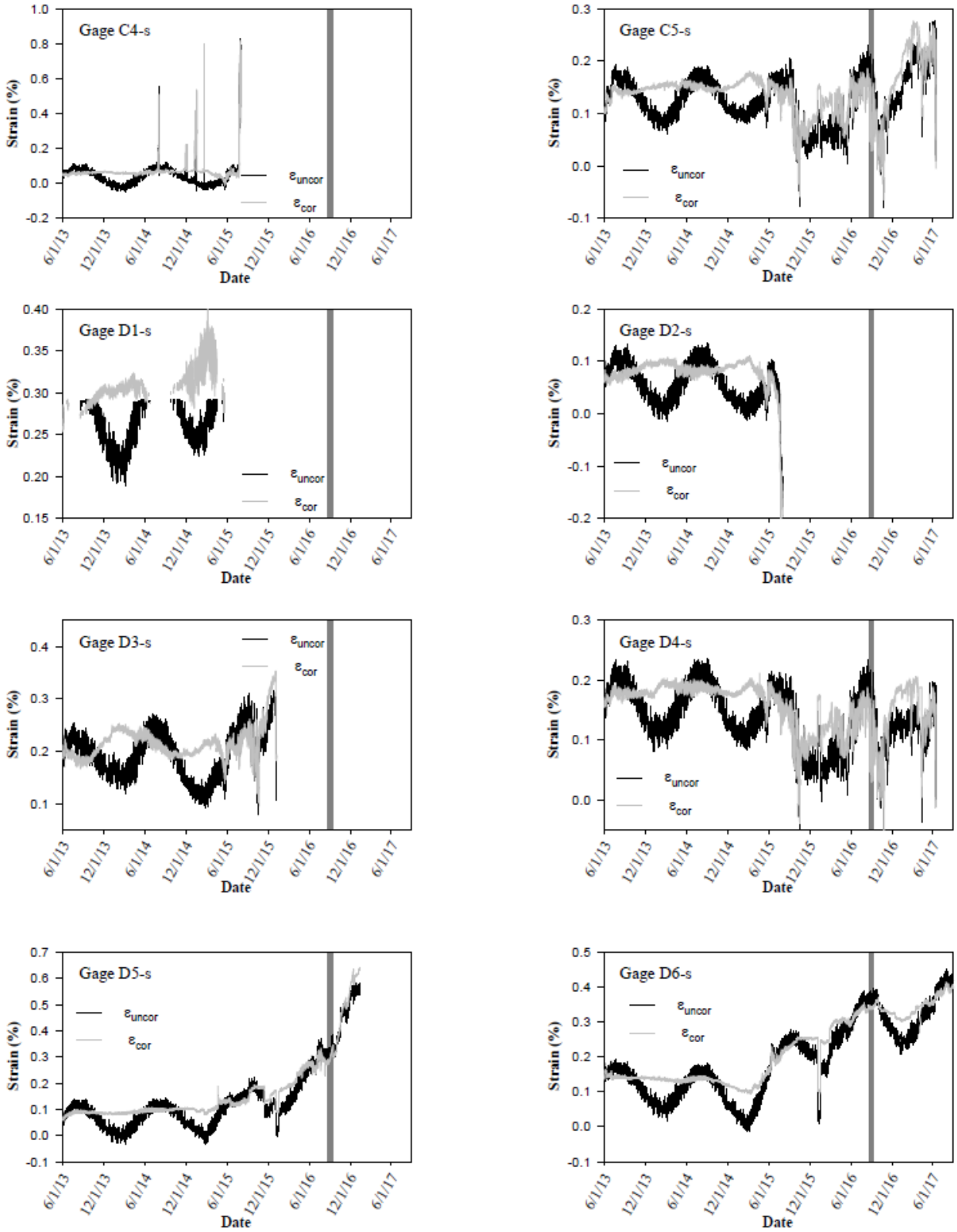

Figure 4.16 Continued

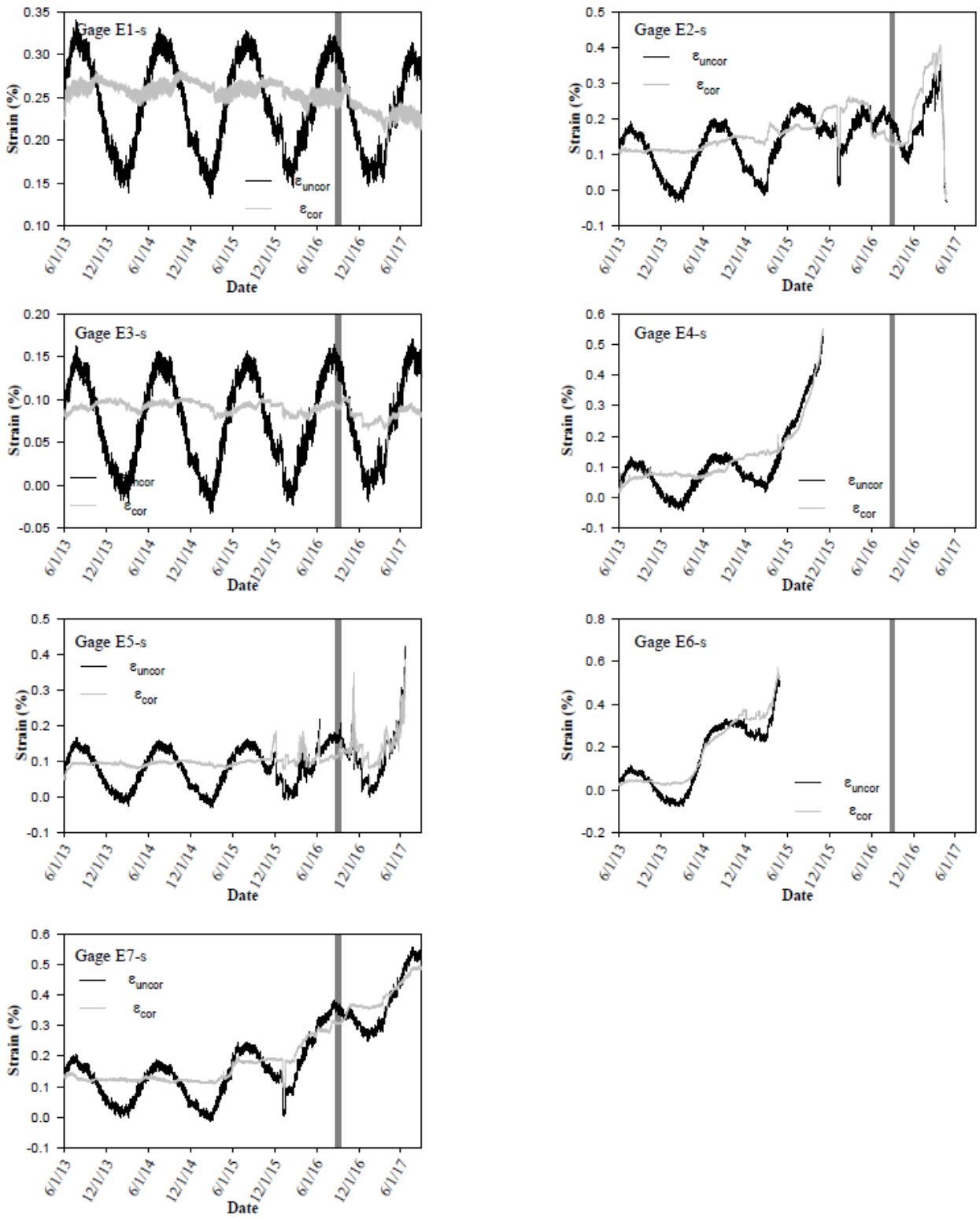

Figure 4.16 Continued

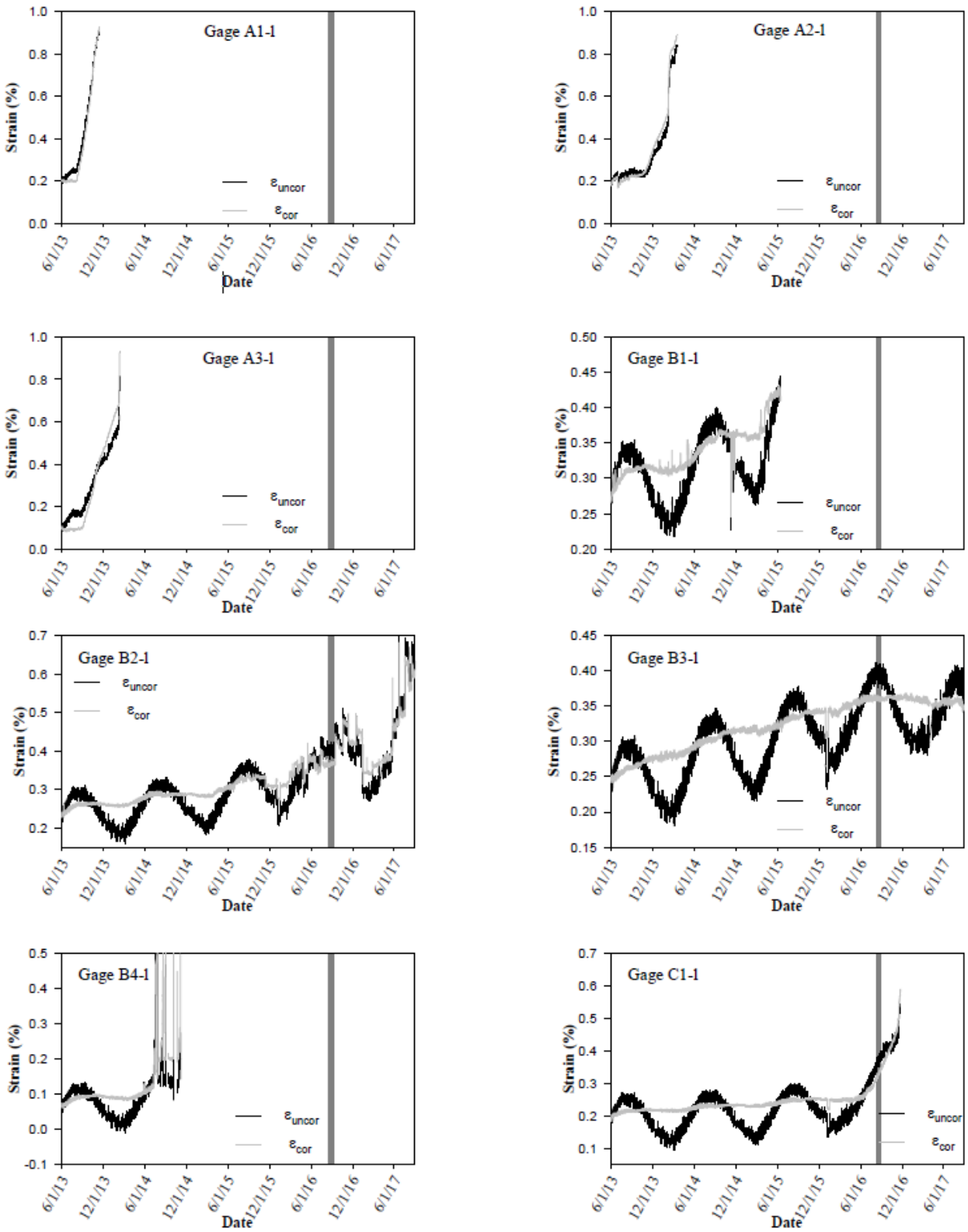

Figure 4.17 West abutment long strain gauge readings (corrected)

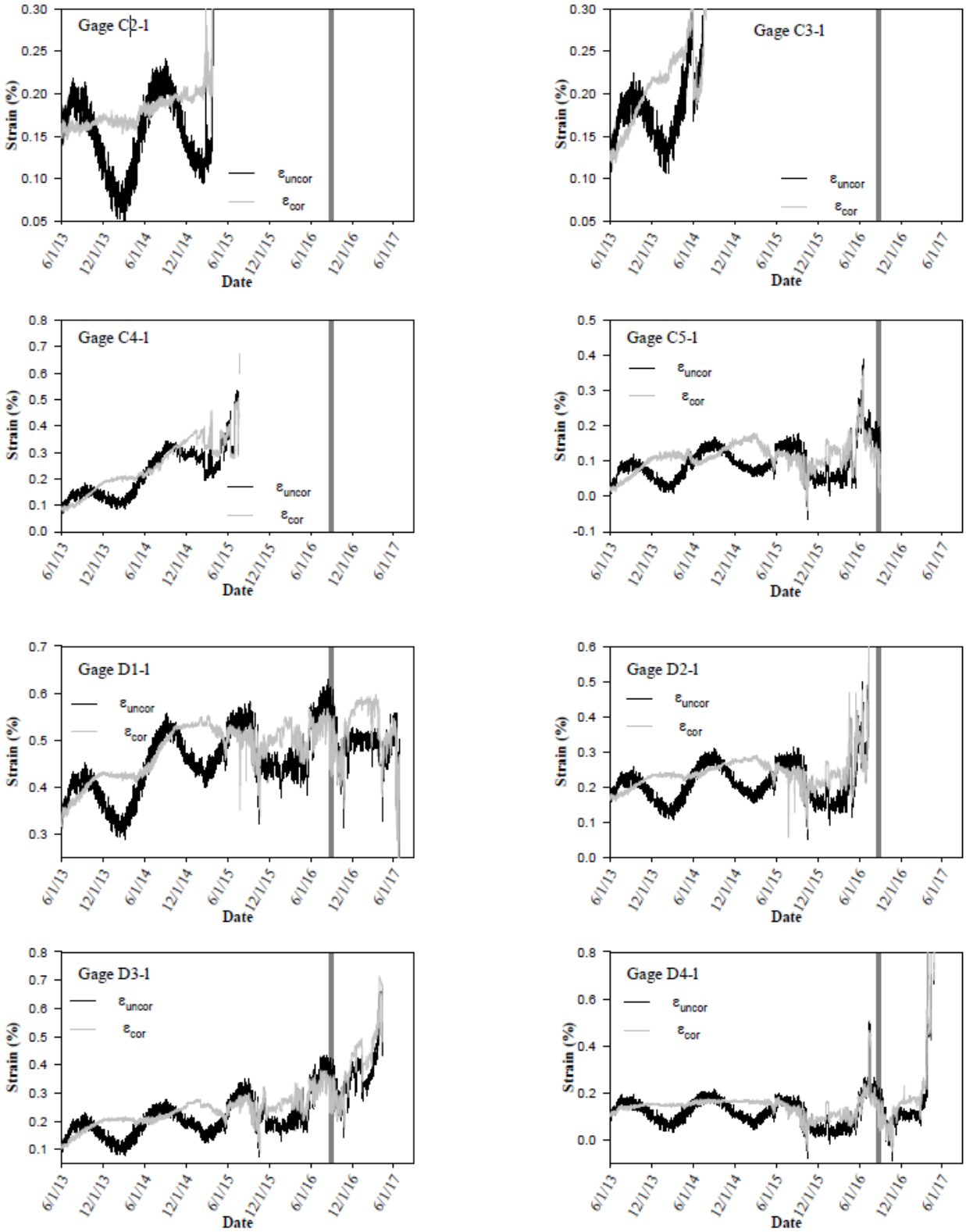

Figure 4.17 Continued

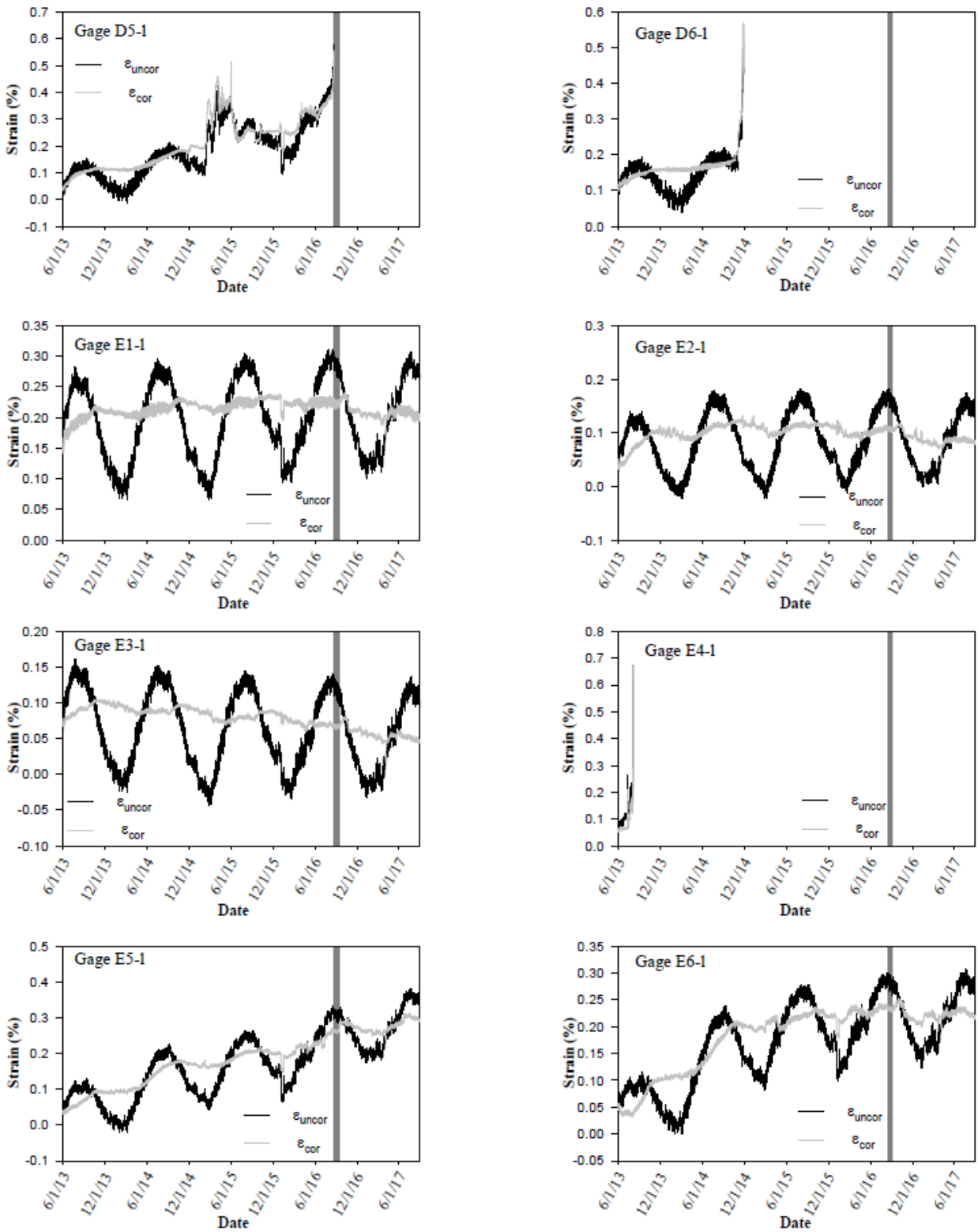

Figure 4.17 Continued

Comparing the long and short strain gauges at the same location to each other, no pattern was discovered. In some cases, the long strain gauges measured higher strains and in some other cases the short strain gauges did. Since no clear trend can be observed, no clear conclusion can be made on the strain reading difference with respect to gauge type.

Figure 4.18 and 4.19 show the strain gauge readings in the east abutment during construction, live load testing, and both monitoring periods for the short and long strain gauges respectively. Strain gauge readings in this abutment were generally less than 0.5% with some abnormal spikes in readings. These spikes can be from sensor unreliability but it is hard to determine their root cause conclusively since readings were only taken approximately every two weeks. Similar to the west abutment, the sensors that continued to perform into this current monitoring period showed consistent readings with the previous monitoring period. It should be noted that the temperature correction method could not be applied to sensors in the east abutment due to the sampling frequency. From these figures, it can be observed that the estimated amount of creep from the start of the first monitoring period to the end of the current monitoring period was approximately 0.1%, however, it is more difficult to accurately determine creep with a low sampling frequency.

As shown in these plots, the following strain gauges have failed or have been determined to be unreliable throughout the monitoring of this structure in the east and west abutments: A1-l, A1-s, A2-l, A2-s, A3-l, A3-s, B1-l, B2-l, B2-s, B3-s, B4-l, B4-s, C1-s, C1-l, C2-l, C2-s, C3-l, C3-s, C4-l, C4-s, C5-s, D1-s, D1-l, D2-l, D2-s, D3-l, D3-s, D4-s, D4-l, D5-l, D5-s, D6-l, D6-s, E4-l, E2-s, E4-s, E5-s, E6-s, E7-l, F1-s, F1-l, H3-s, H3-l, I4-s, and J7-s. This totals 45 out of 100 strain gauges. One can see that a higher number of unreliable and failed sensors are in the west abutment;

this is in part due to the fact that readings were taken more frequently in the west abutment over the east abutment so outlying data points can be picked up on more accurately.

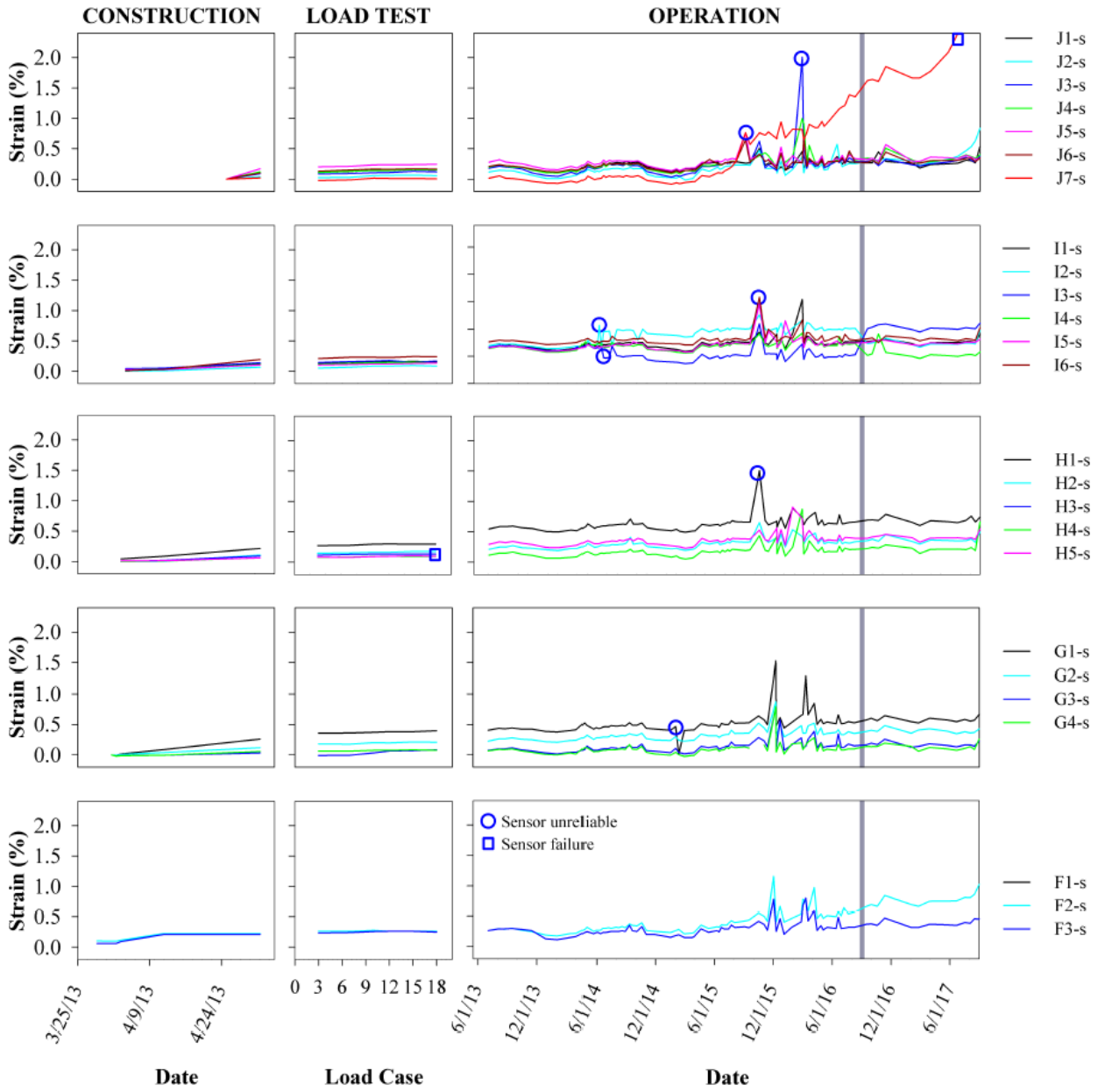

Figure 4.18 East abutment short strain gauge readings (uncorrected)

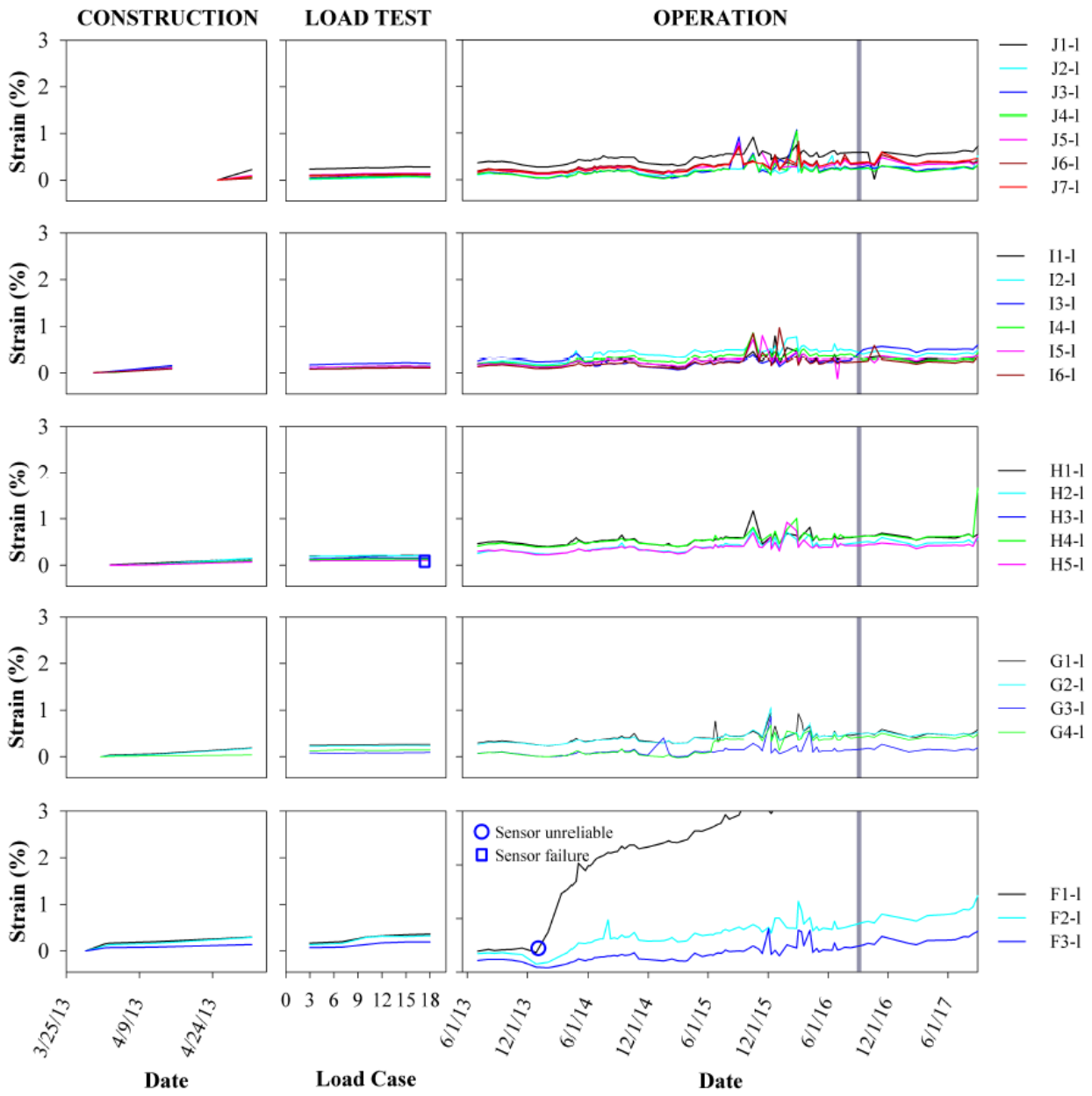

Figure 4.19 East abutment long strain gauge readings (uncorrected)

4.2.4 Under Bridge Strain Gauges

Ten long strain gauges were attached to the bottom of the bridge beams, at the middle of each beam, to monitor the deformations of the bridge. Five of the gauges stopped working at the very beginning of the first monitoring period. Figure 4.20 presents the recorded strains from the five gauges that continued to work. As discussed in the previous section, the measured strain is affected by temperature so these strain measurements were also corrected, using the same approach that is presented in Meehan and Talebi (2017). The corrected data shows nearly constant strains that are less than 0.5%. Gauge b3 stopped working during the first monitoring period. Gauges b2 and b8 show some slight signs of creep; this should continue to be monitored moving forward. Overall, measured strain readings from this current monitoring period are consistent with the readings measured in the first monitoring period.

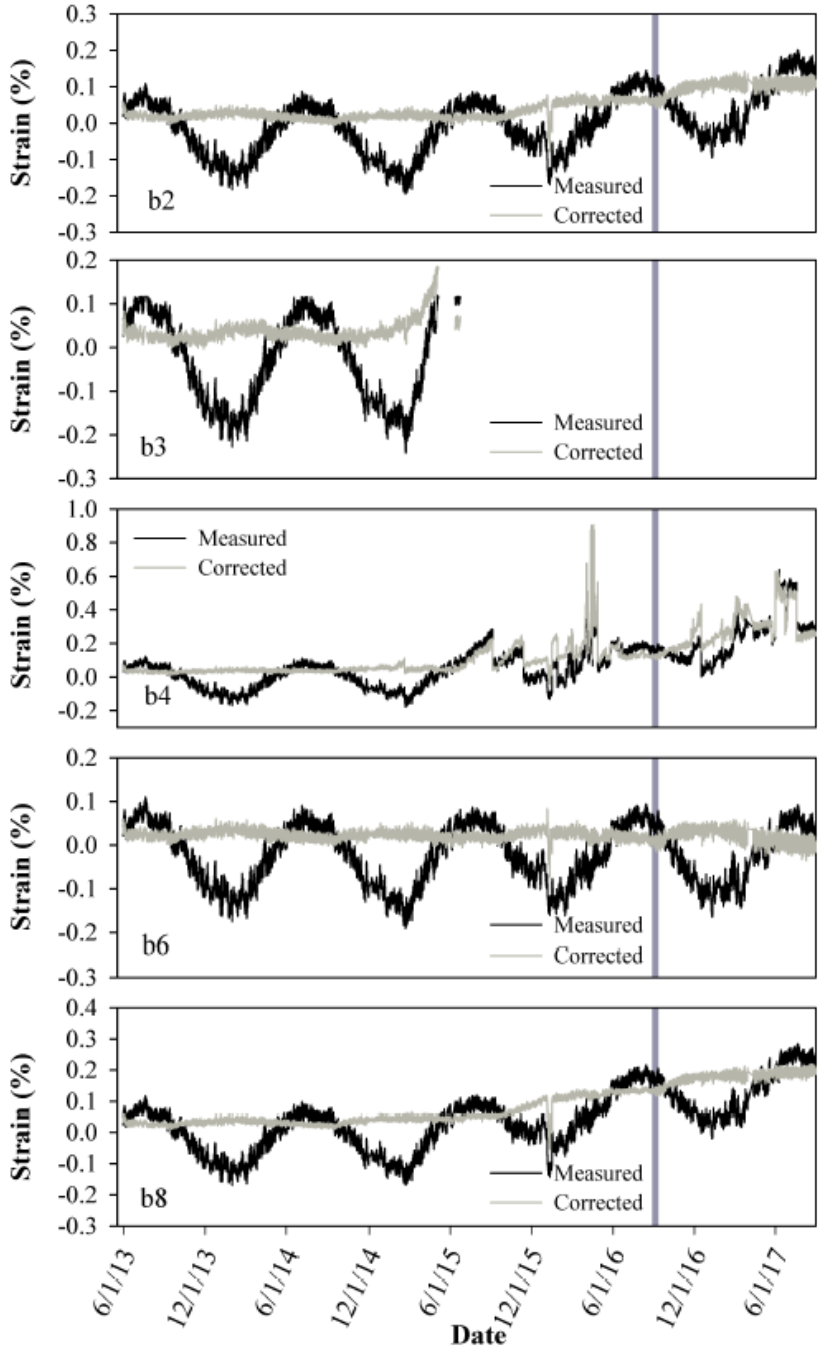

Figure 4.20 Under bridge strain gauge readings

4.2.5 Facing Wall Movements Measured by Surveying Targets

As discussed in Chapter 3, surveying targets were installed on each abutment facing wall to monitor lateral deflection and settlement of the facing wall. Fifteen targets were installed on each abutment facing wall. Surveying of these targets was performed by the Delaware Department of Transportation using a TOPCON Pulse Total Station, GPT-3000 series instrument, survey legs, tripod legs, prisms, and mini prisms. The measurement precision and resolution for the system was 6.0 mm and 0.3 mm respectively. Figures 4.21 and 4.22 show the lateral deflection of the installed targets on the middle section during live load testing and both monitoring periods of the east and west abutments, respectively. Figures 4.23 and 4.24 show the settlement of the installed targets on the middle section during live load testing and both monitoring periods of the east and west abutments, respectively. In Figures 4.21 through 4.24, the greyscale error band illustrates the measurement uncertainty associated with the surveying technique; the magnitude of this error band was determined based on the 6.0 mm precision. As shown, along the roadway centerline, measured deflections were between 0 and 10 mm while measured settlements were between 0 and 12 mm. Surveying data from this current monitoring period fell within this error band indicating that the structure is still performing well and that additional displacements of significance are not occurring over time.

Figures 4.25 through 4.40 display the measured deflection and settlement for cross-sections through the west and east facing walls that are offset from the roadway centerline. The corresponding data for the same elevation at the roadway centerline are also presented in these figures for comparison. The measured values for these targets are similar to the measured values along the roadway centerline which demonstrates that the overall horizontal and vertical movements of the facing wall was very low for both abutments. The measured deflection and

settlements for the targets offset from the roadway centerline show consistent trends from the surveying that was performed in the previous monitoring period.

The maximum measured settlement and maximum lateral wall deflection were both approximately 13 mm. Generally speaking however, measurements of settlement and displacement were much lower than this, and exhibited noise due to accuracy limitations of the surveying approach that was utilized. Clearly, with all of the measured settlements and lateral deflections being this small, it can be concluded that a very low amount of overall deformation of the abutment occurred.

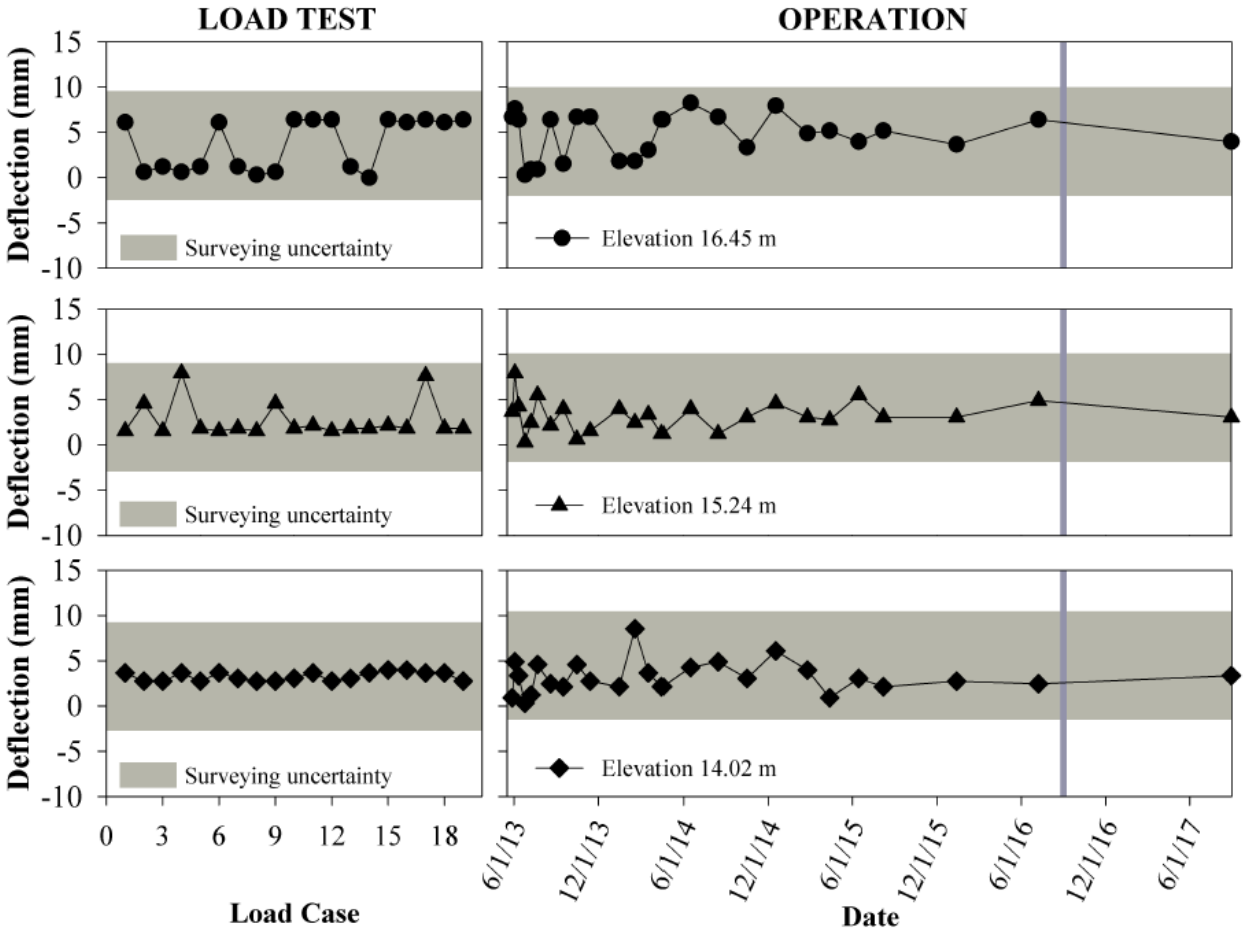

Figure 4.21 Lateral deflection of the east facing wall at the abutment centerline

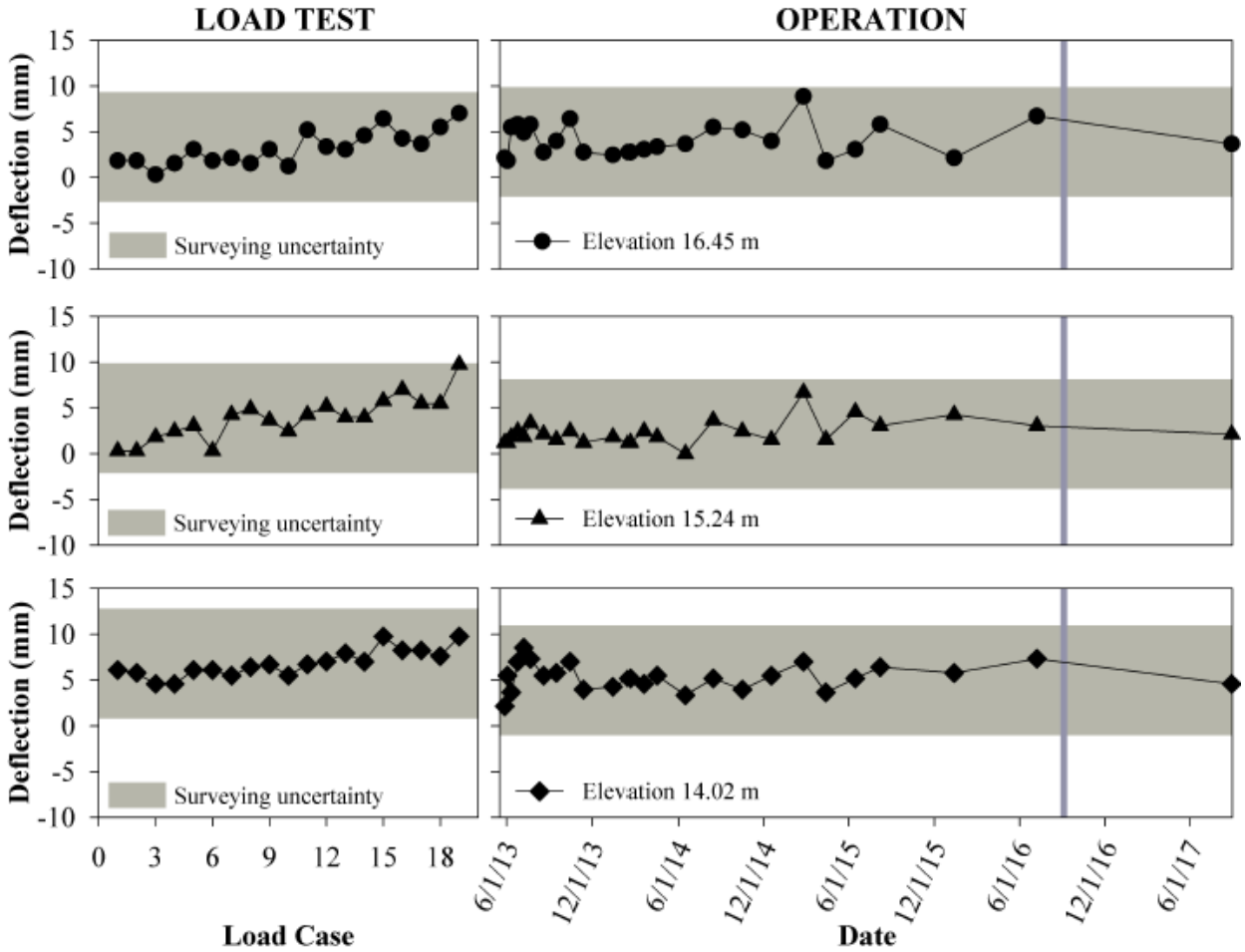

Figure 4.22 Lateral deflection of the west facing wall at the abutment centerline

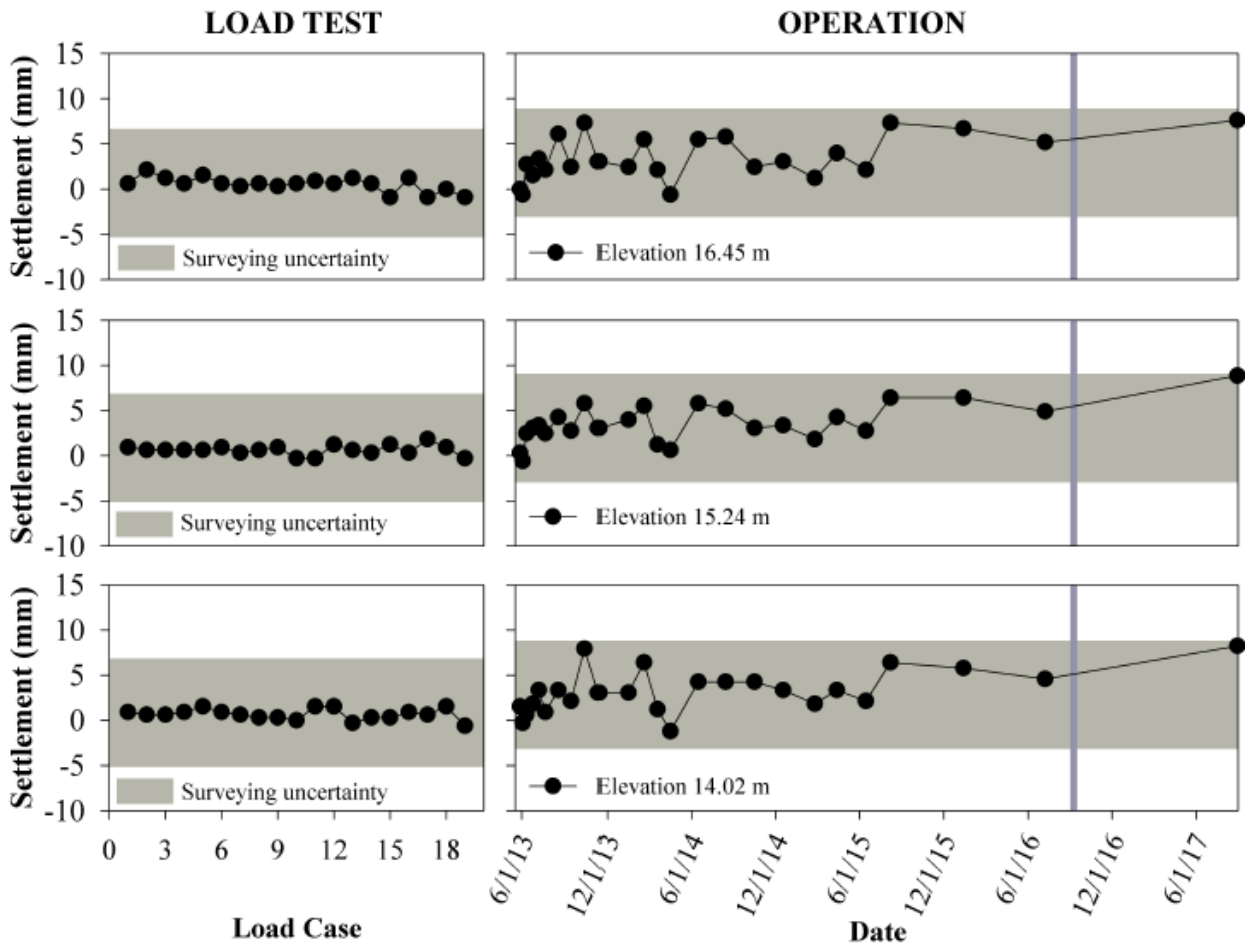

Figure 4.23 Settlement of the east facing wall at the abutment centerline

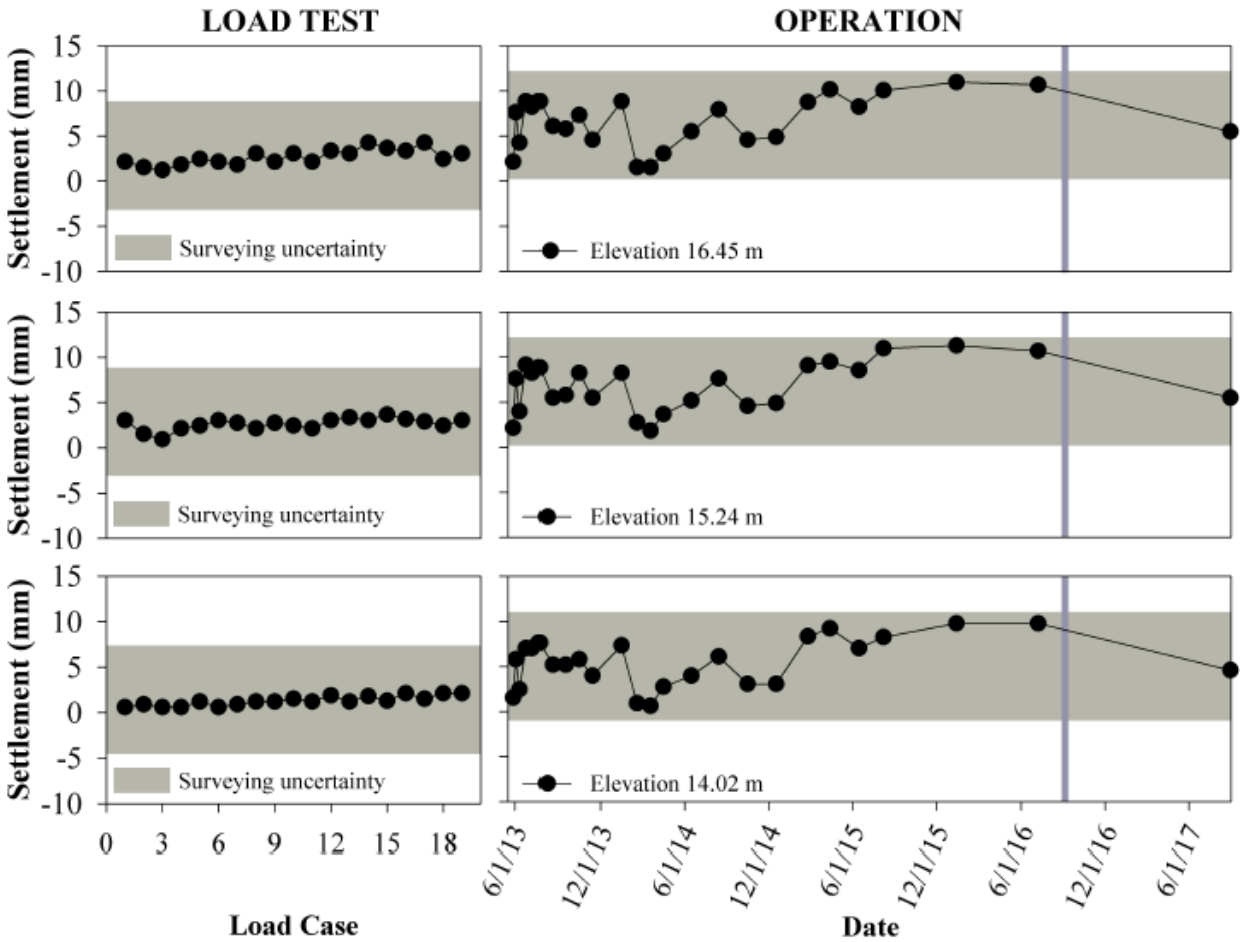

Figure 4.24 Settlement of the west facing wall at the abutment centerline

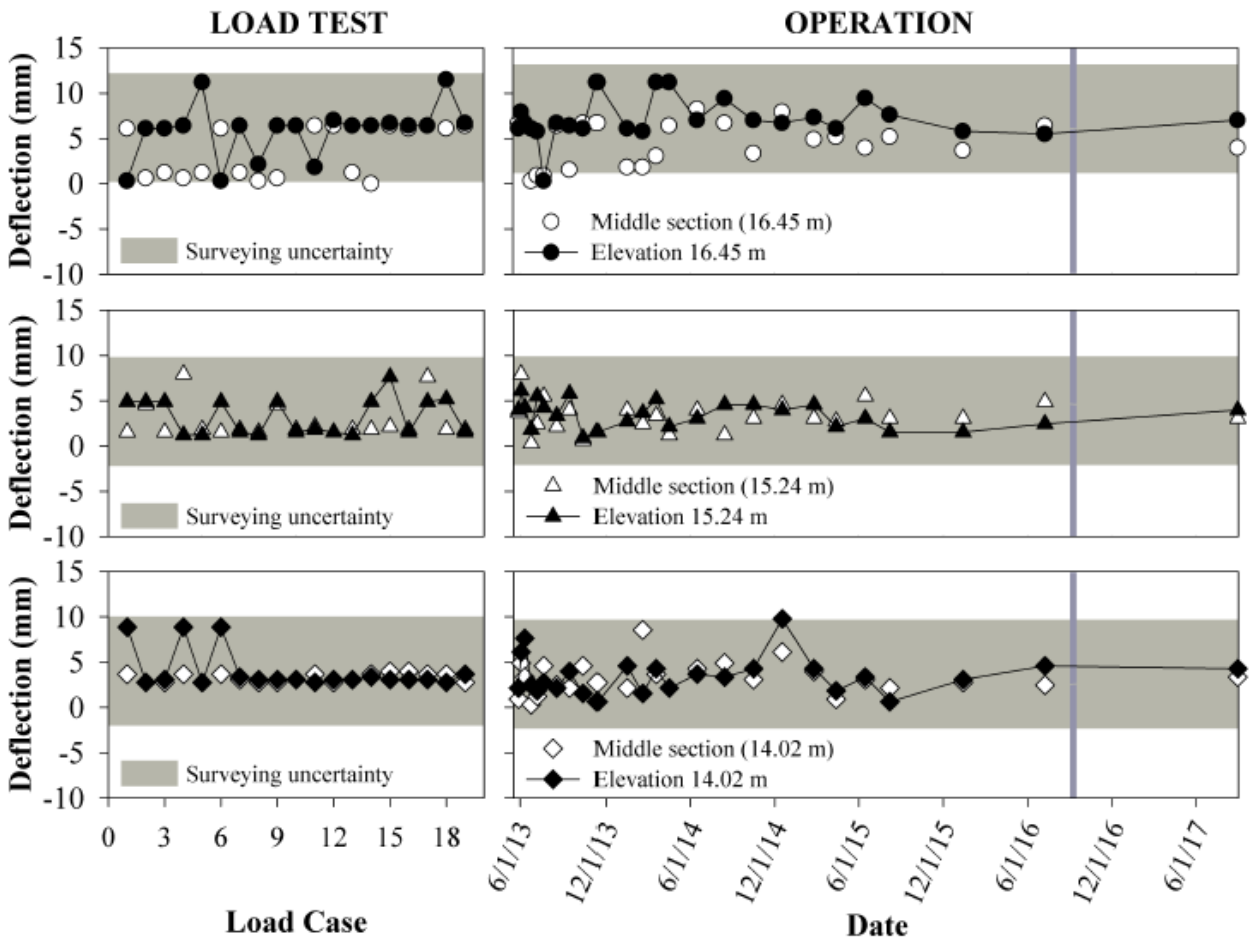

Figure 4.25 Lateral deflection of the east facing wall at 5.6 m offset from the abutment centerline, in the upstream direction

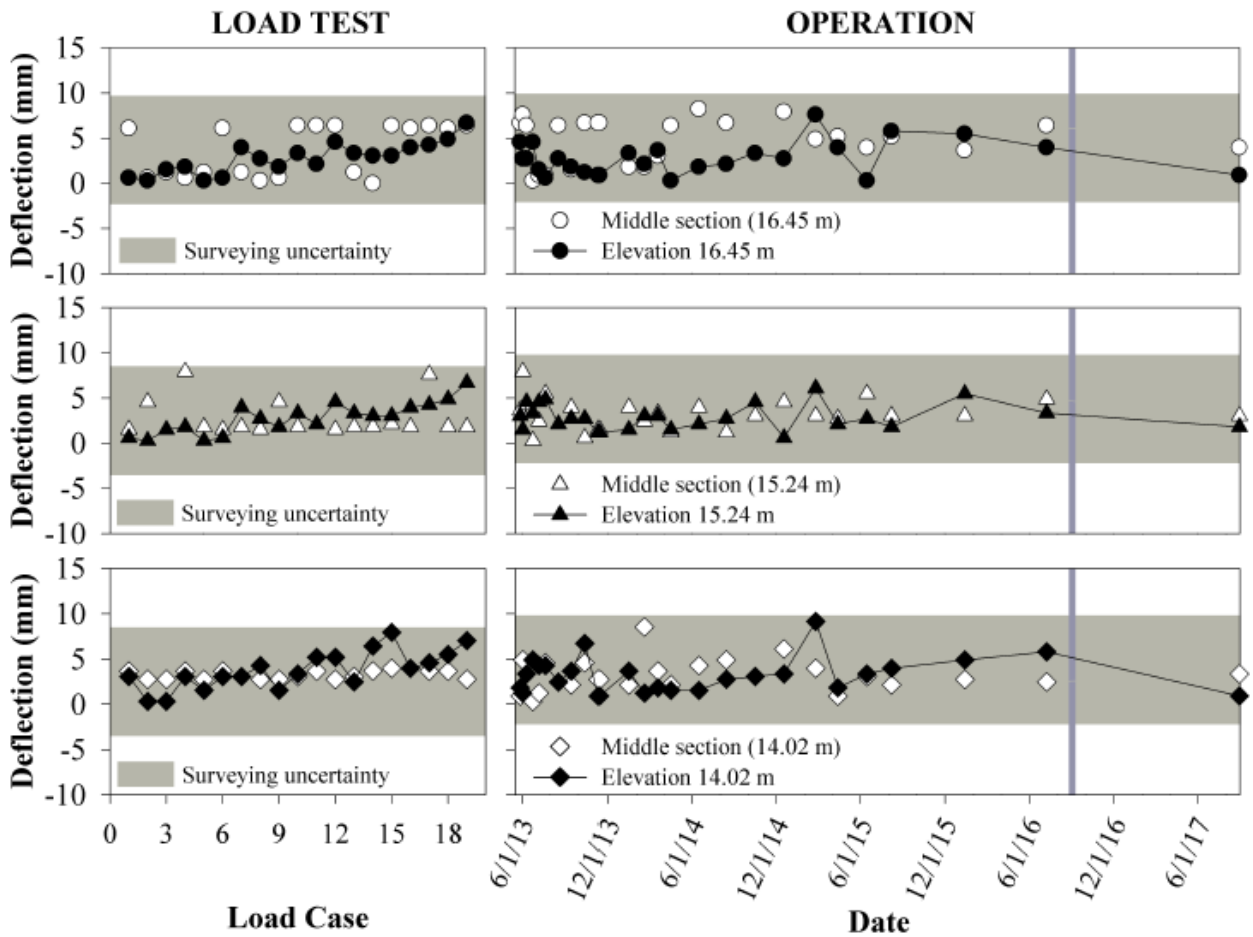

Figure 4.26 Lateral deflection of the west facing wall at 5.6 m offset from the abutment centerline, in the upstream direction

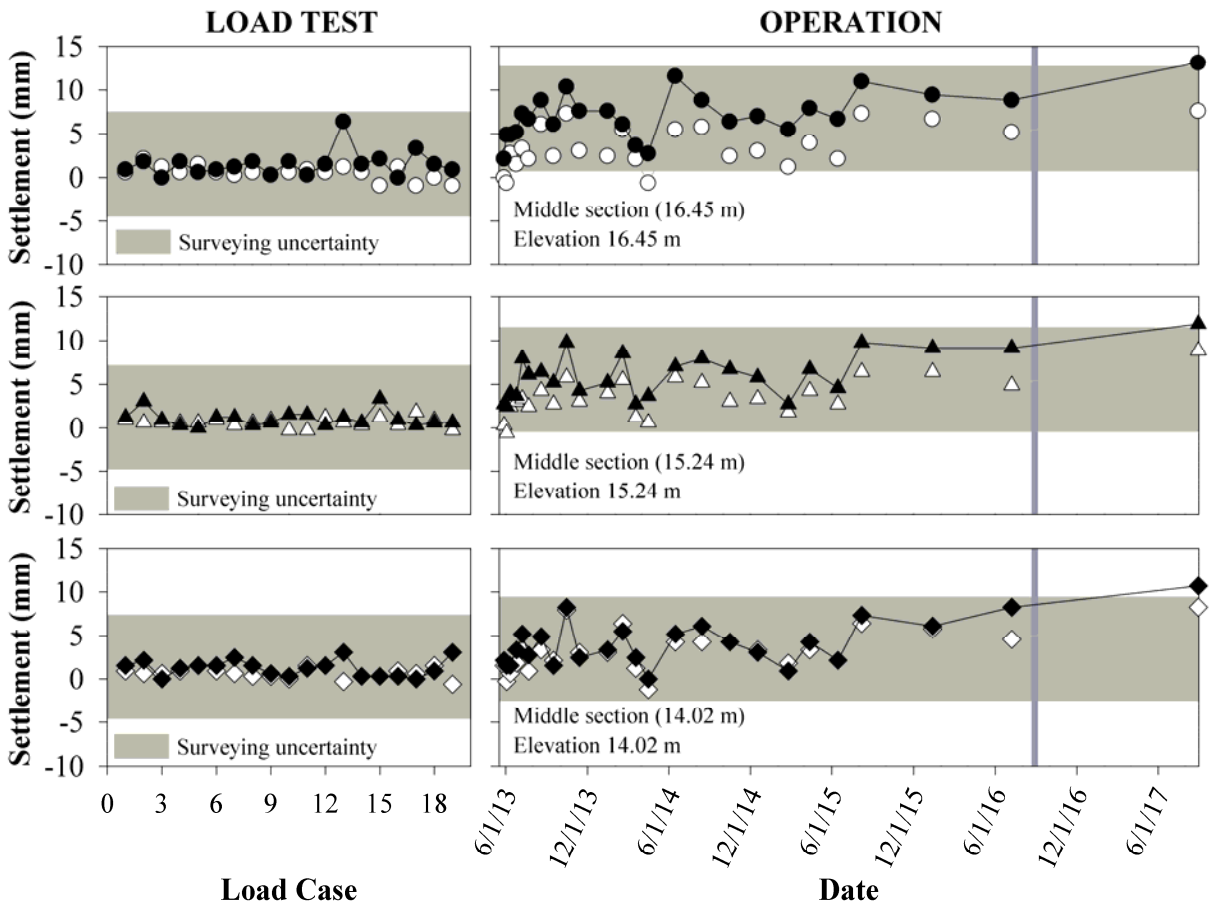

Figure 4.27 Settlement of the east facing wall at 5.6 m offset from the abutment centerline, in the upstream direction

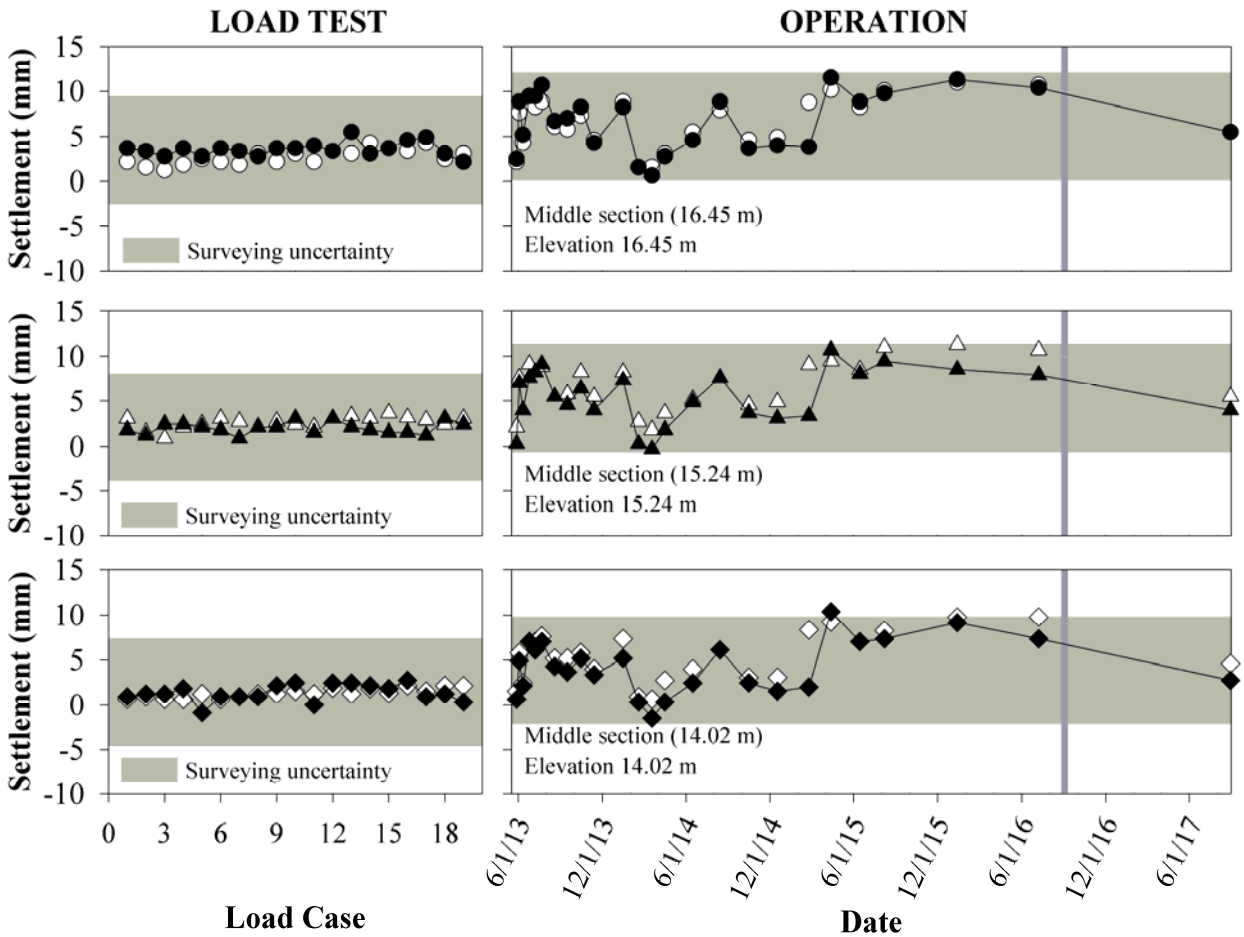

Figure 4.28 Settlement of the west facing wall at 5.6 m offset from the abutment centerline, in the upstream direction

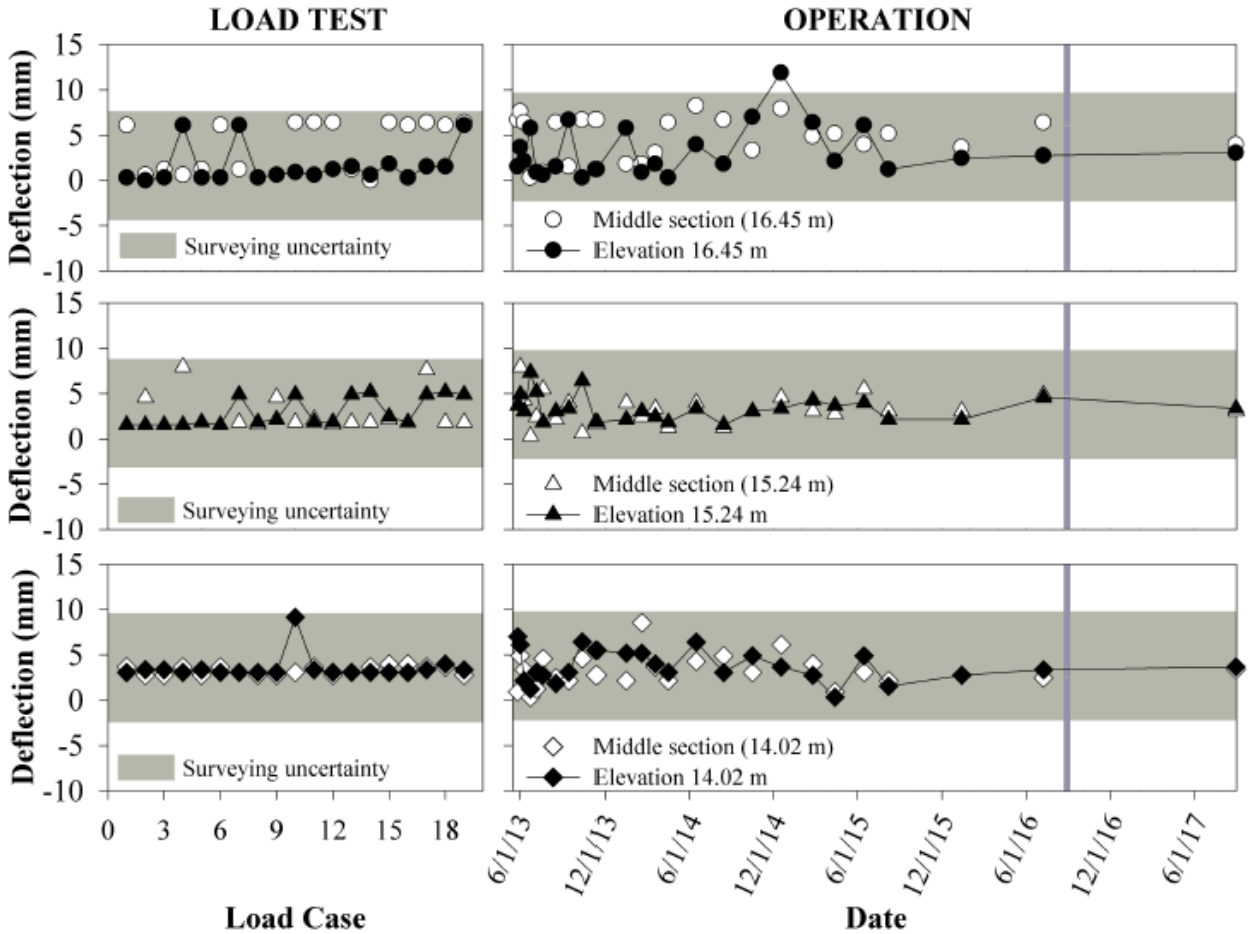

Figure 4.29 Lateral deflection of the east facing wall at 2.8 m offset from the abutment centerline, in the upstream direction

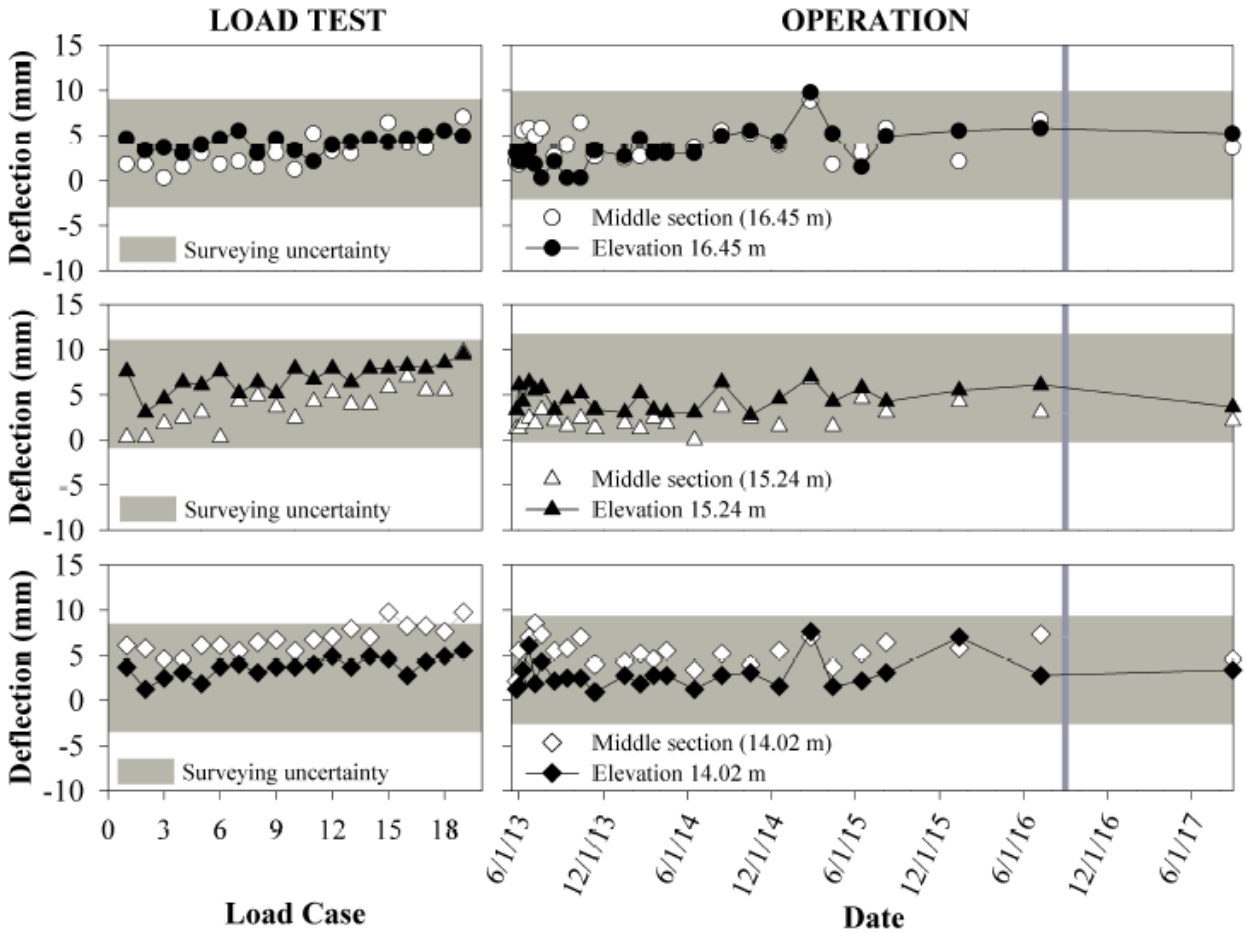

Figure 4.30 Lateral deflection of the west facing wall at 2.8 m offset from the abutment centerline, in the upstream direction

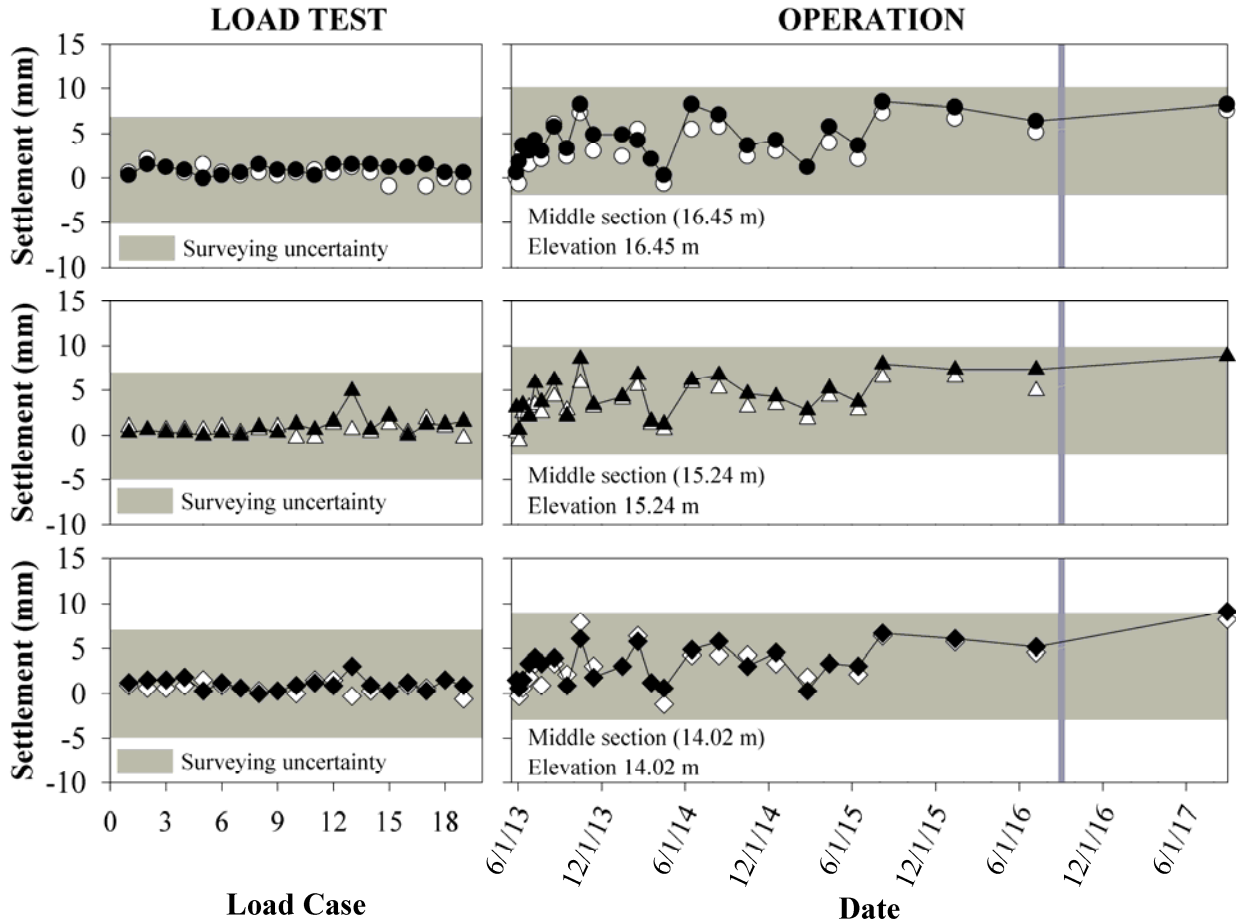

Figure 4.31 Settlement of the east facing wall at 2.8 m offset from the abutment centerline, in the upstream direction

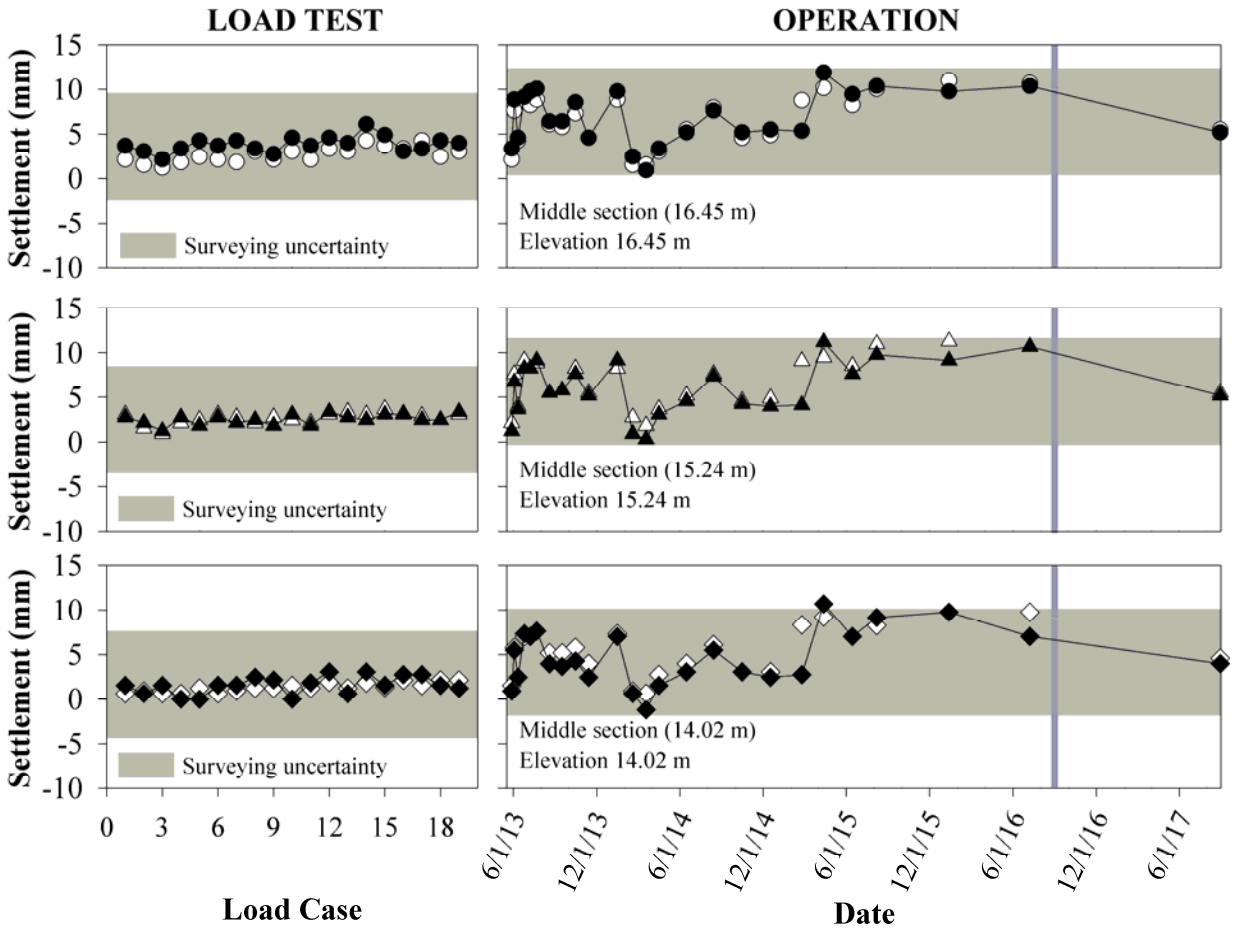

Figure 4.32 Settlement of the west facing wall at 2.8 m offset from the abutment centerline, in the upstream direction

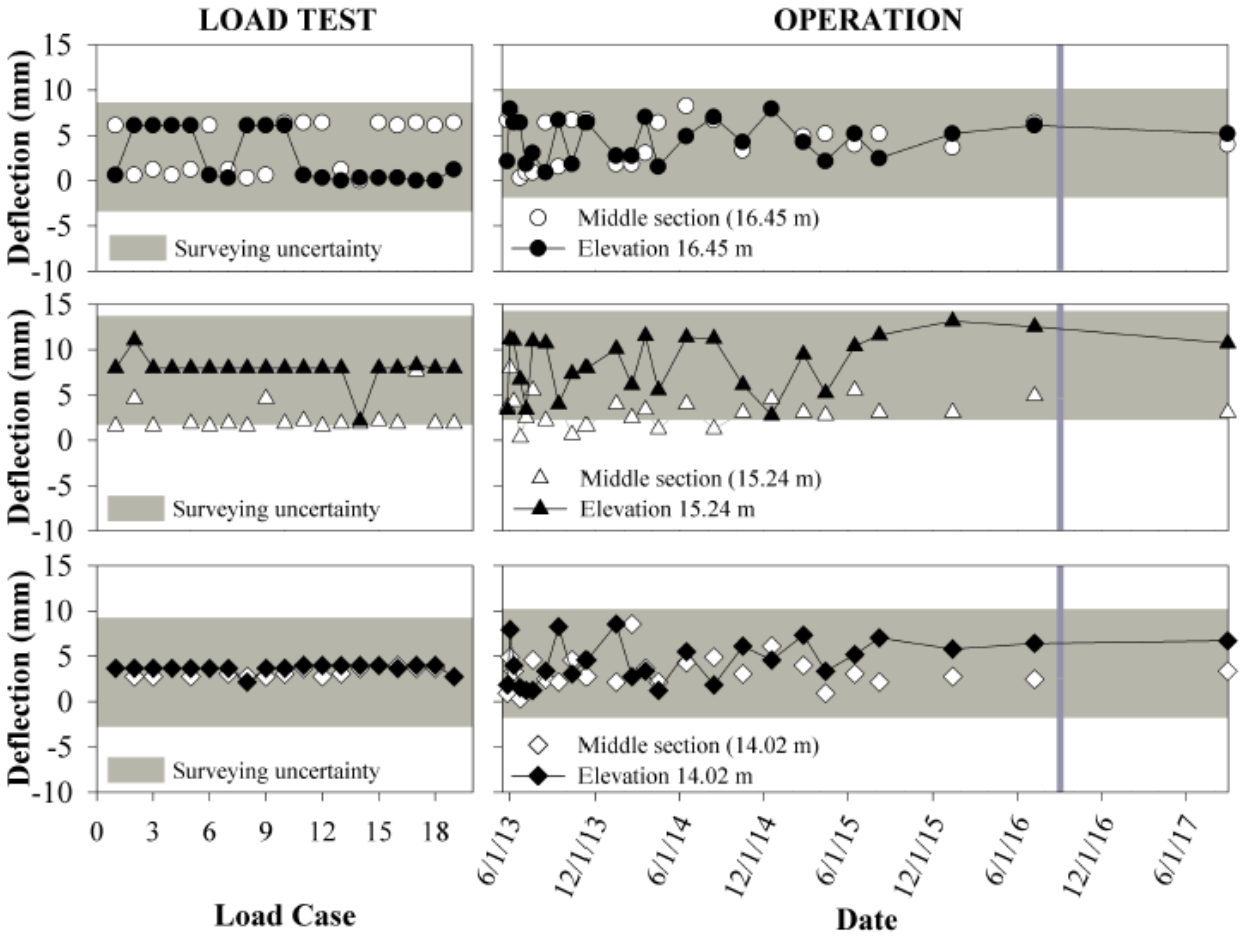

Figure 4.33 Lateral deflection of the east facing wall at 2.8 m offset from the abutment centerline, in the downstream direction

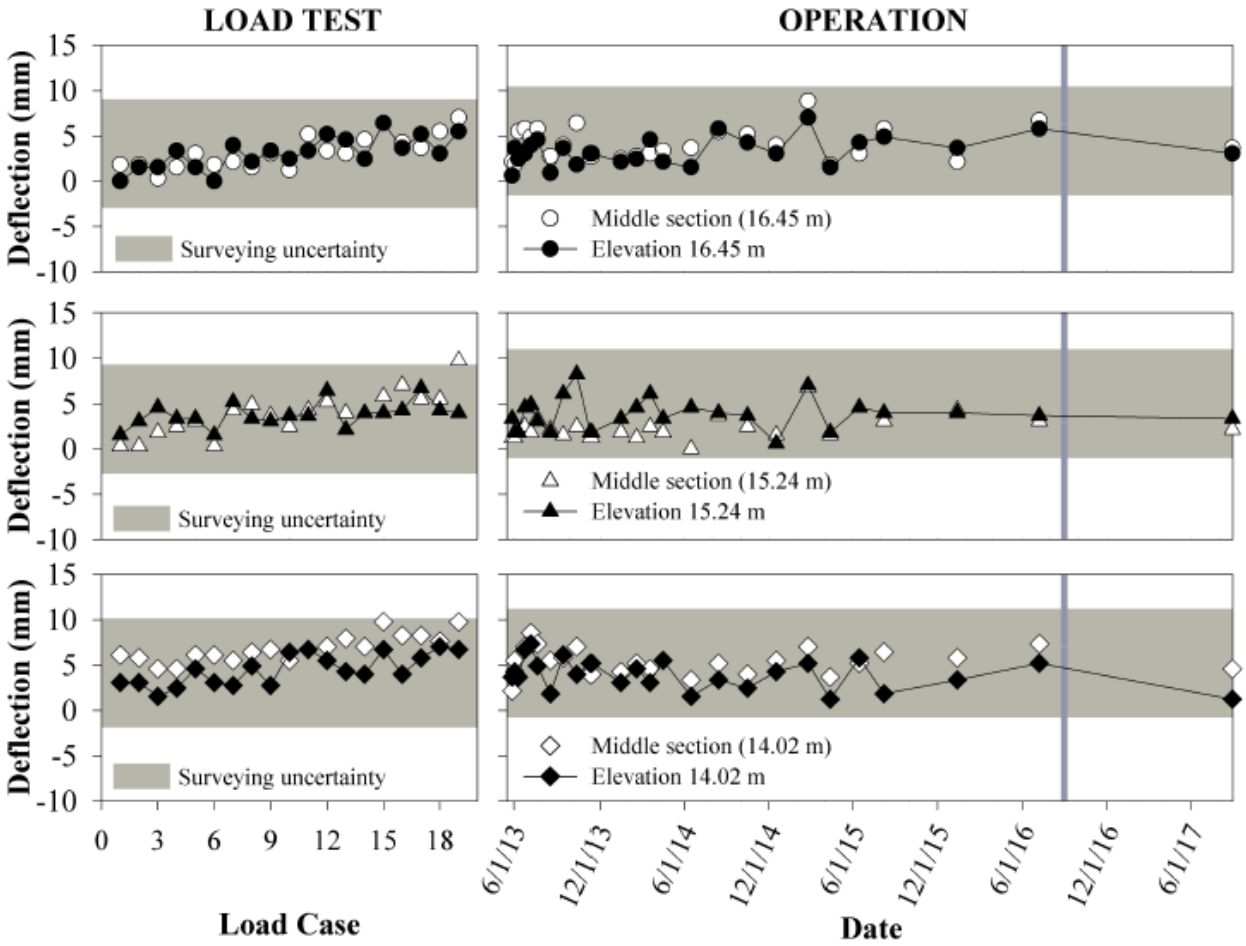

Figure 4.34 Lateral deflection of the west facing wall at 2.8 m offset from the abutment centerline, in the downstream direction

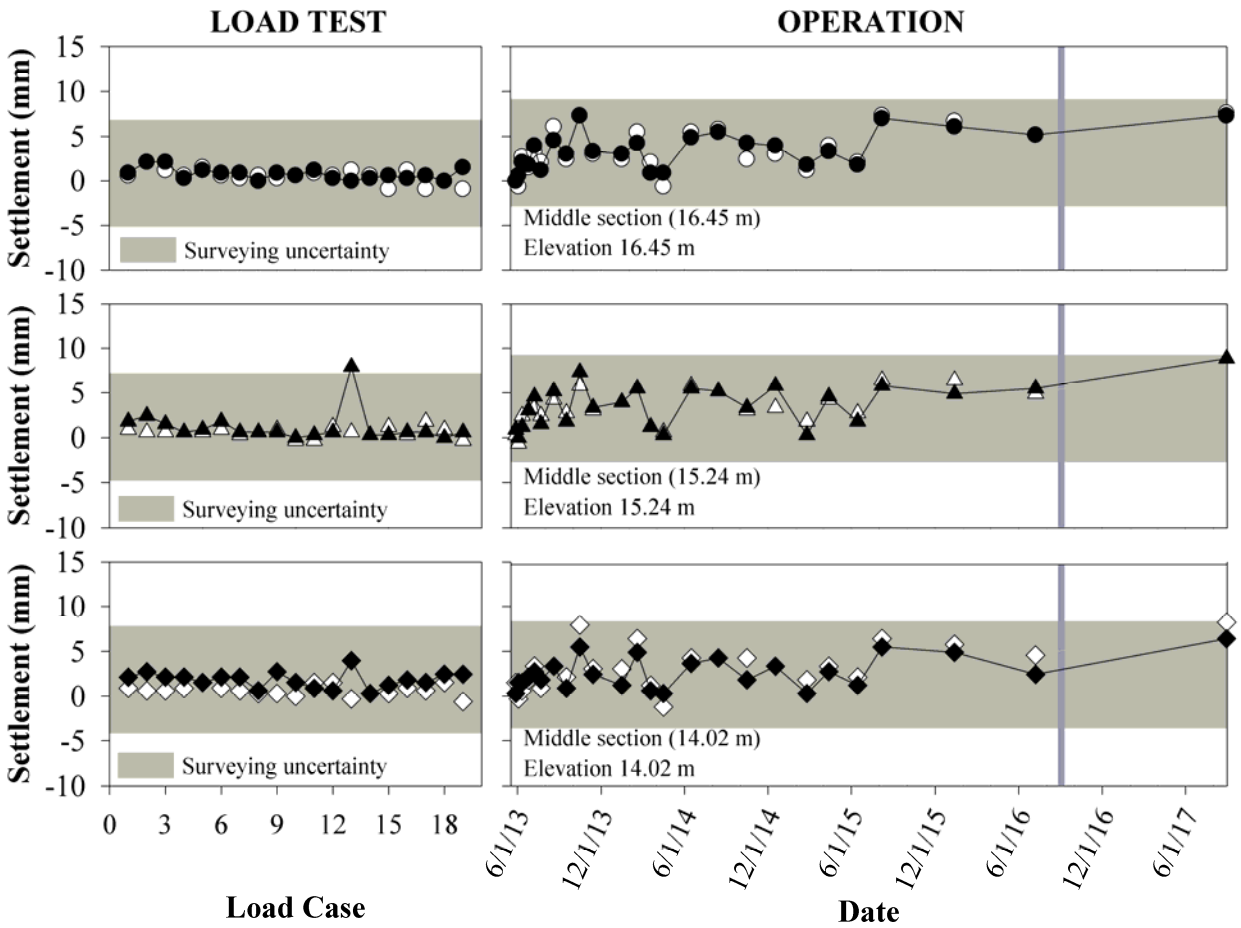

Figure 4.35 Settlement of the east facing wall at 2.8 m offset from the abutment centerline, in the downstream direction

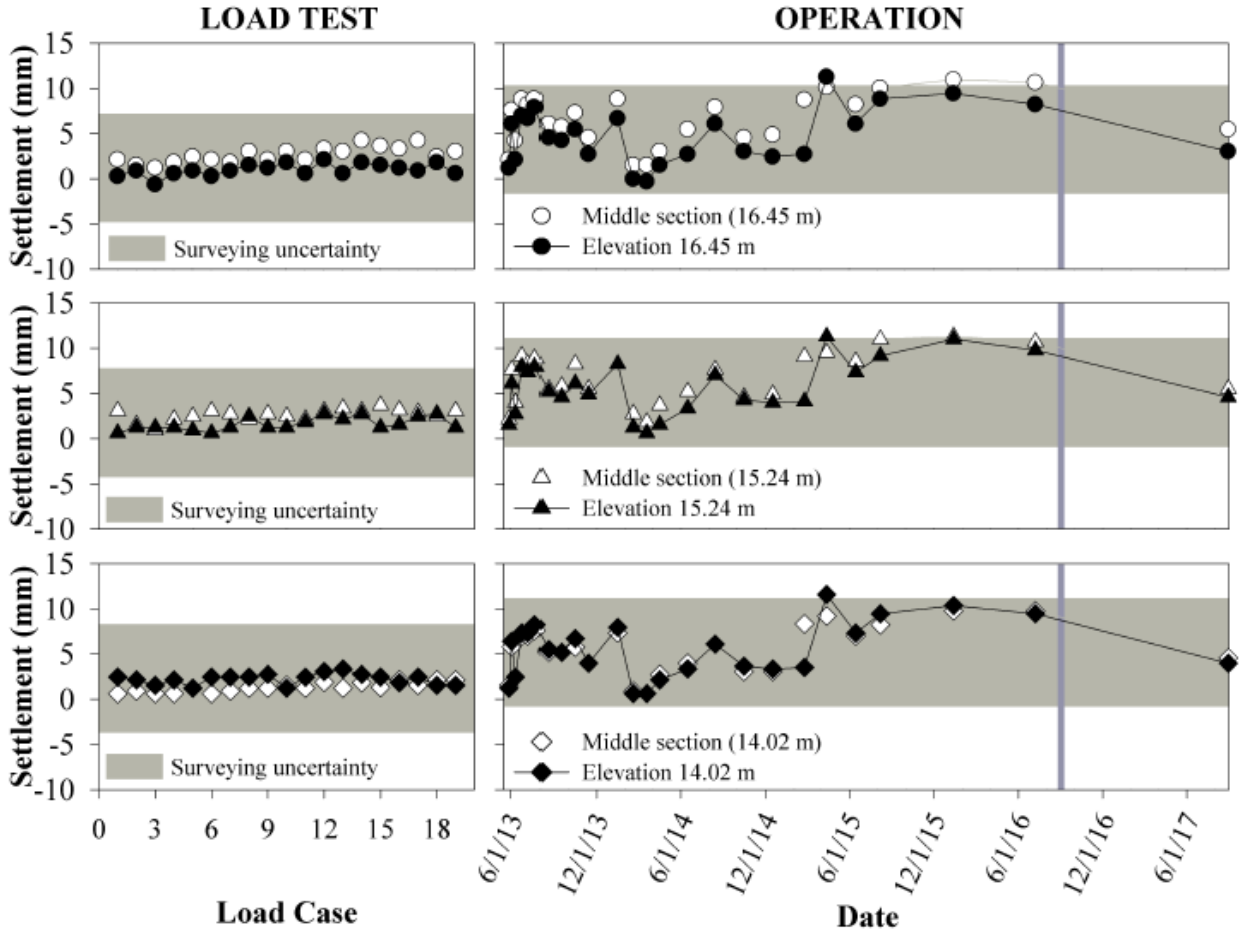

Figure 4.36 Settlement of the west facing wall at 2.8 m offset from the abutment centerline, in the downstream direction

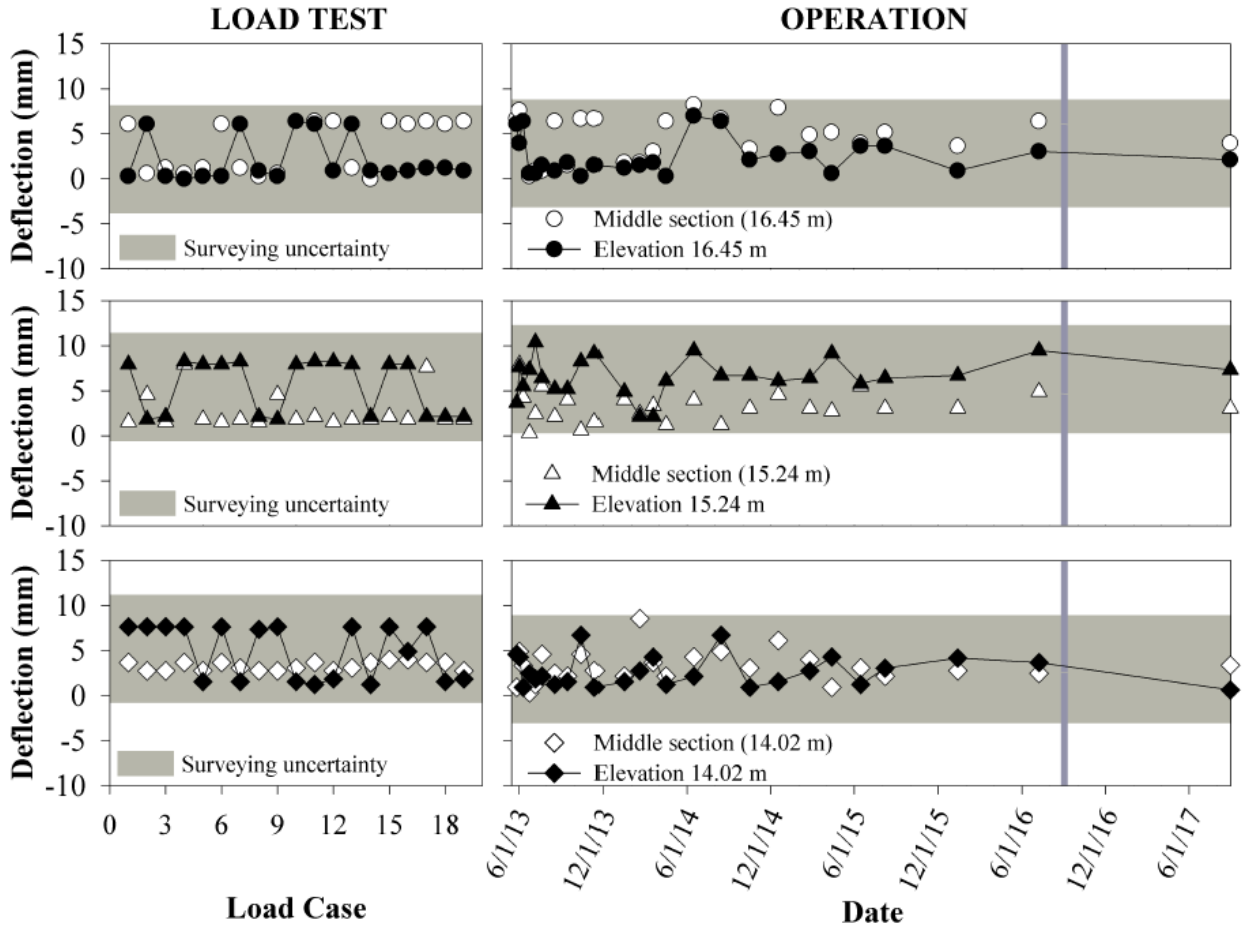

Figure 4.37 Lateral deflection of the east facing wall at 5.6 m offset from the abutment centerline, in the downstream direction

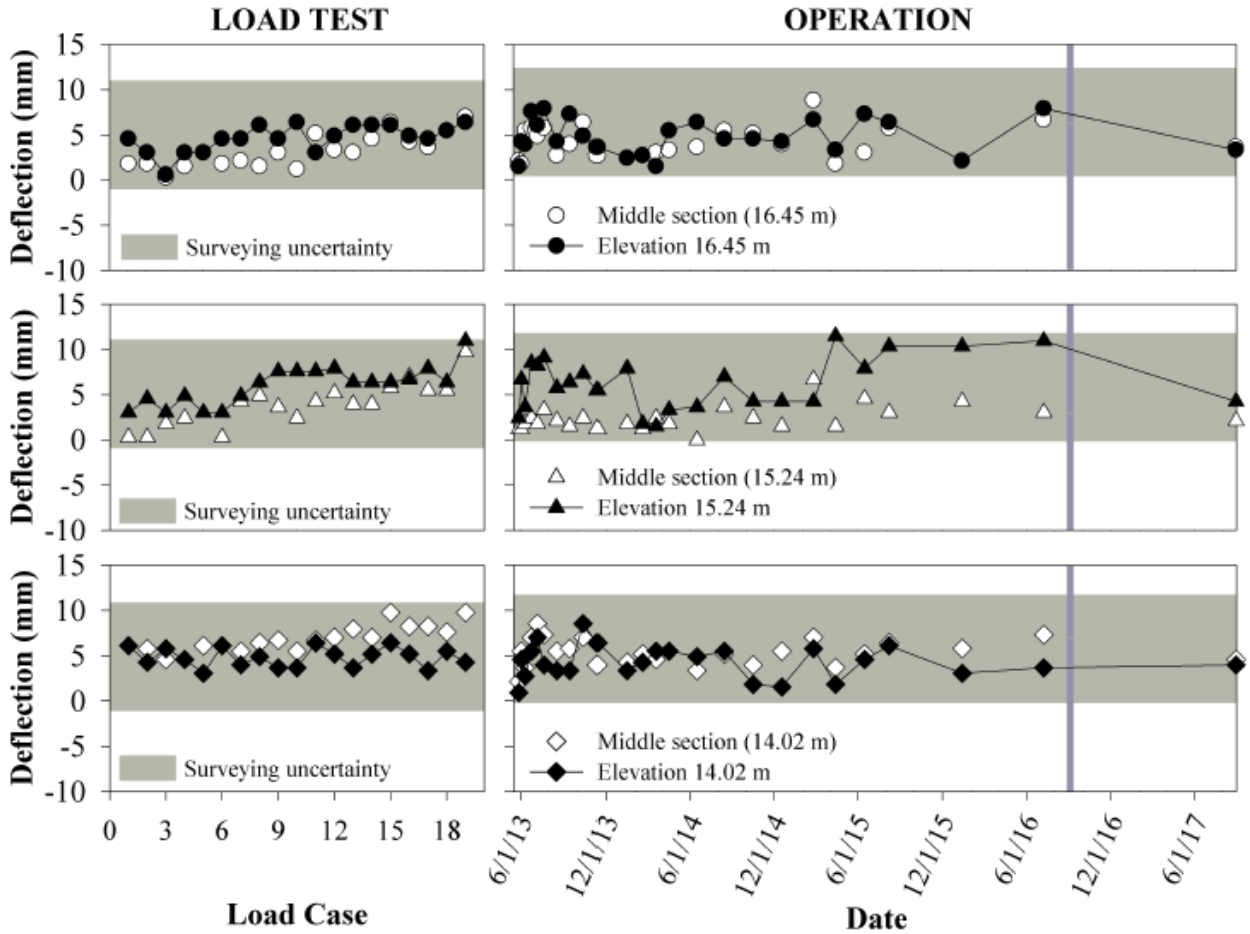

Figure 4.38 Lateral deflection of the west facing wall at 5.6 m offset from the abutment centerline, in the downstream direction

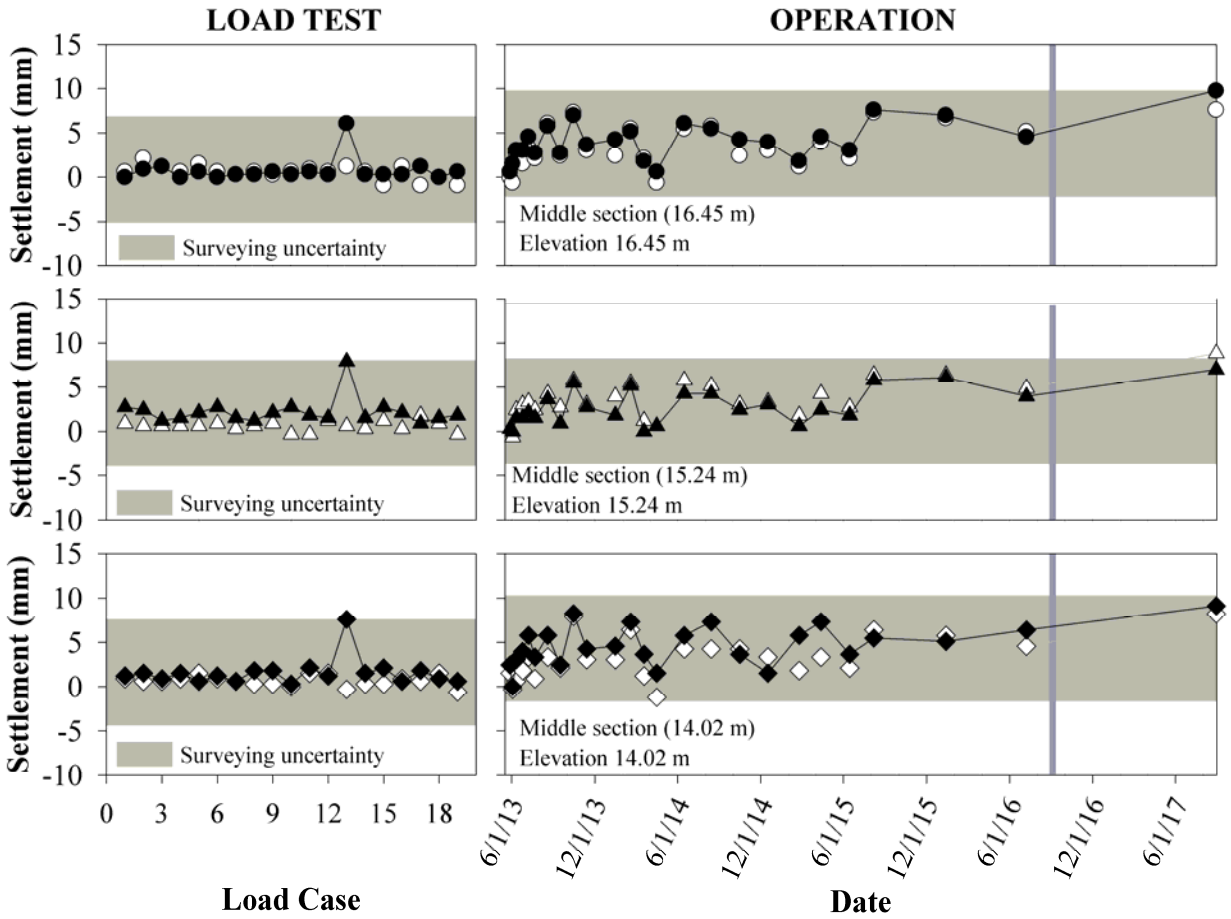

Figure 4.39 Settlement of the east facing wall at 5.6 m offset from the abutment centerline, in the downstream direction

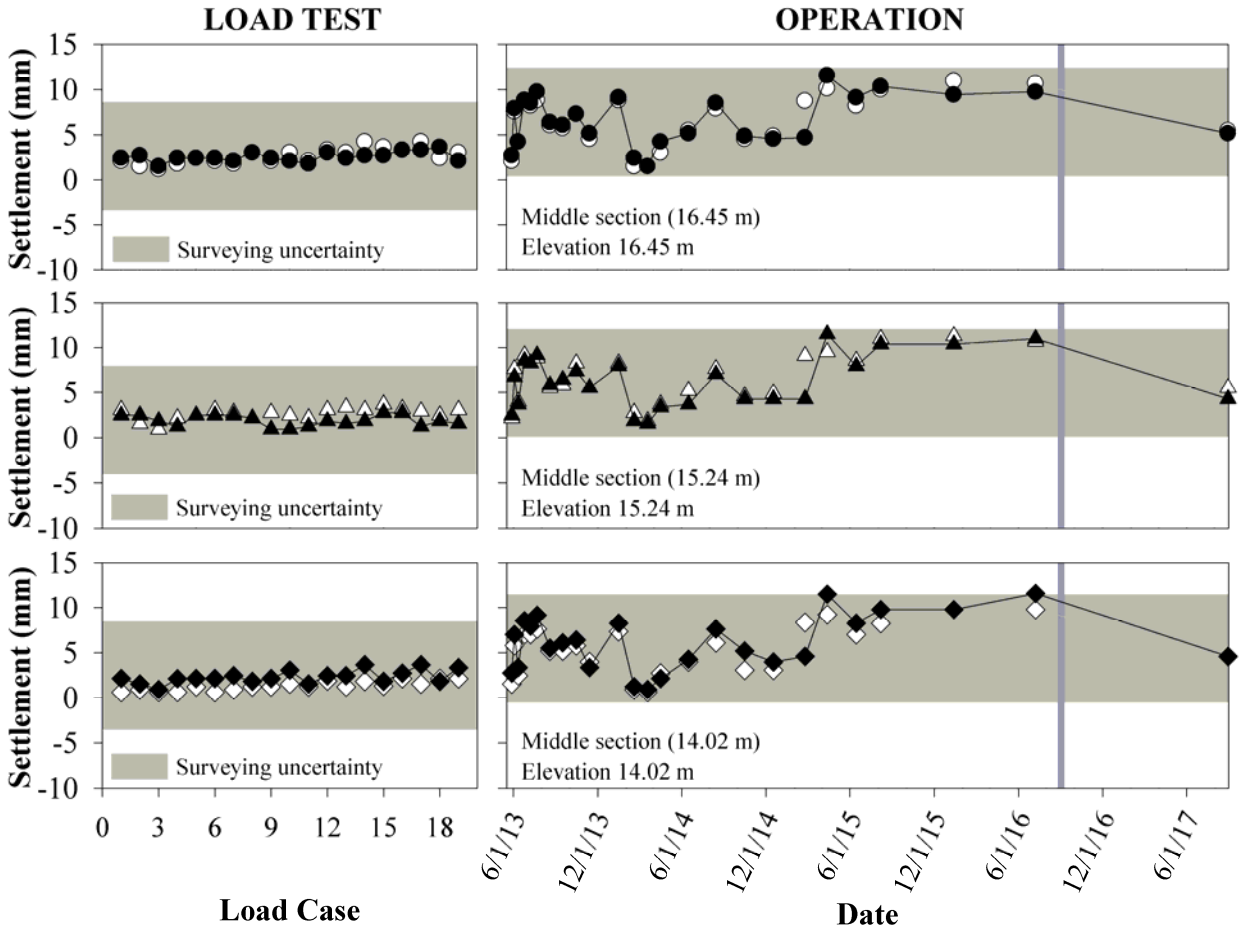

Figure 4.40 Settlement of the west facing wall at 5.6 m offset from the abutment centerline, in the downstream direction

Contour plots of the east and west facing wall lateral deflection for both monitoring periods are presented in Figures 4.41 and 4.42 respectively. As discussed in Chapter 3, there was not a continuous trend over time when surveying would be conducted. As time went on and less movement was seen, surveying was conducted less frequently. Figures 4.43 and 4.44 show the contour plots of facing wall settlement for both monitoring periods for the east and west abutments, respectively. Figures 4.41 through 4.44 show that the maximum lateral deflections and settlements were both approximately 13 mm, and also that most measured values were significantly less than that amount (generally in the 5 to 10 mm range).

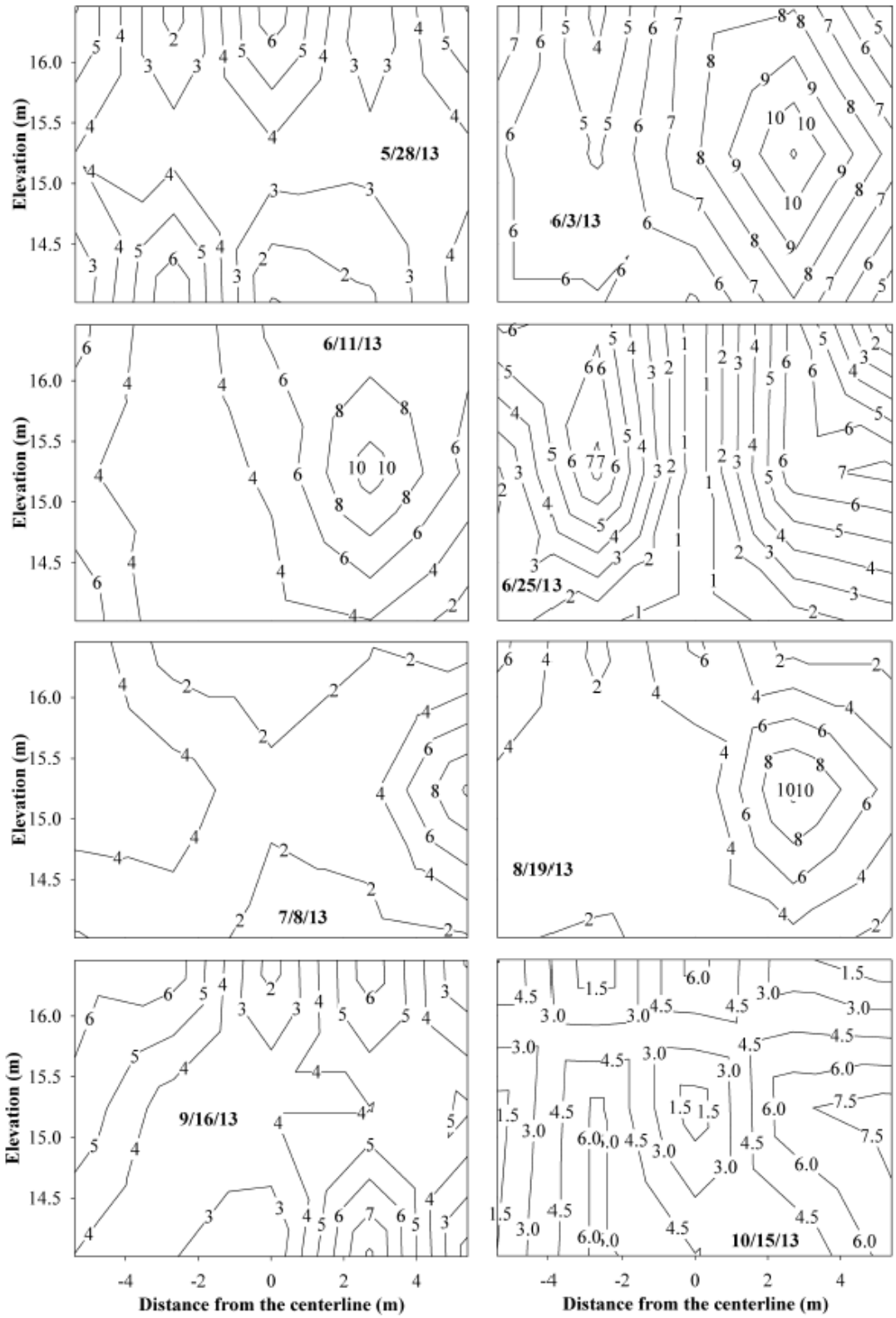

Figure 4.41 Contour plots of the east facing wall deflection over both monitoring periods

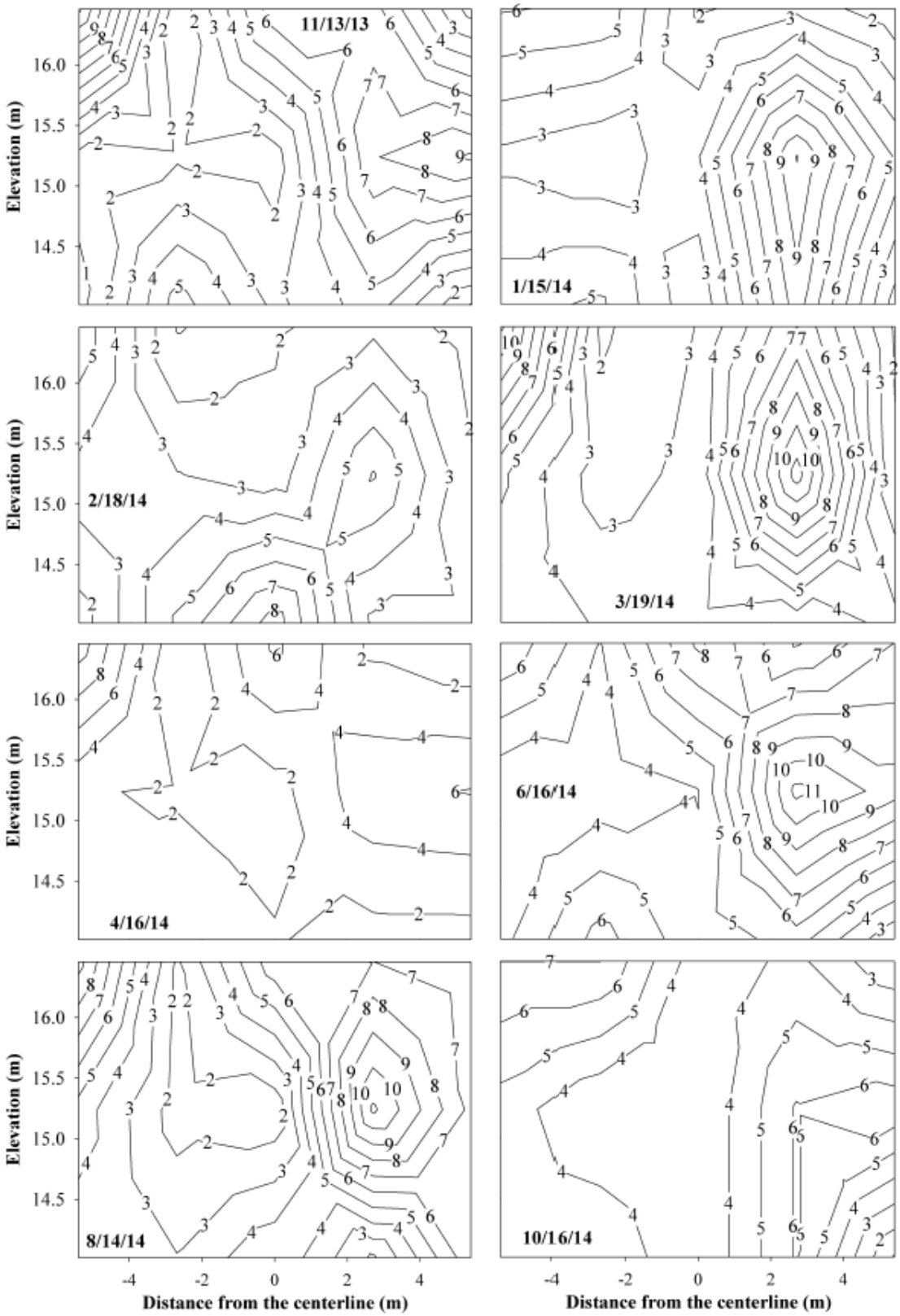

Figure 4.41 Continued

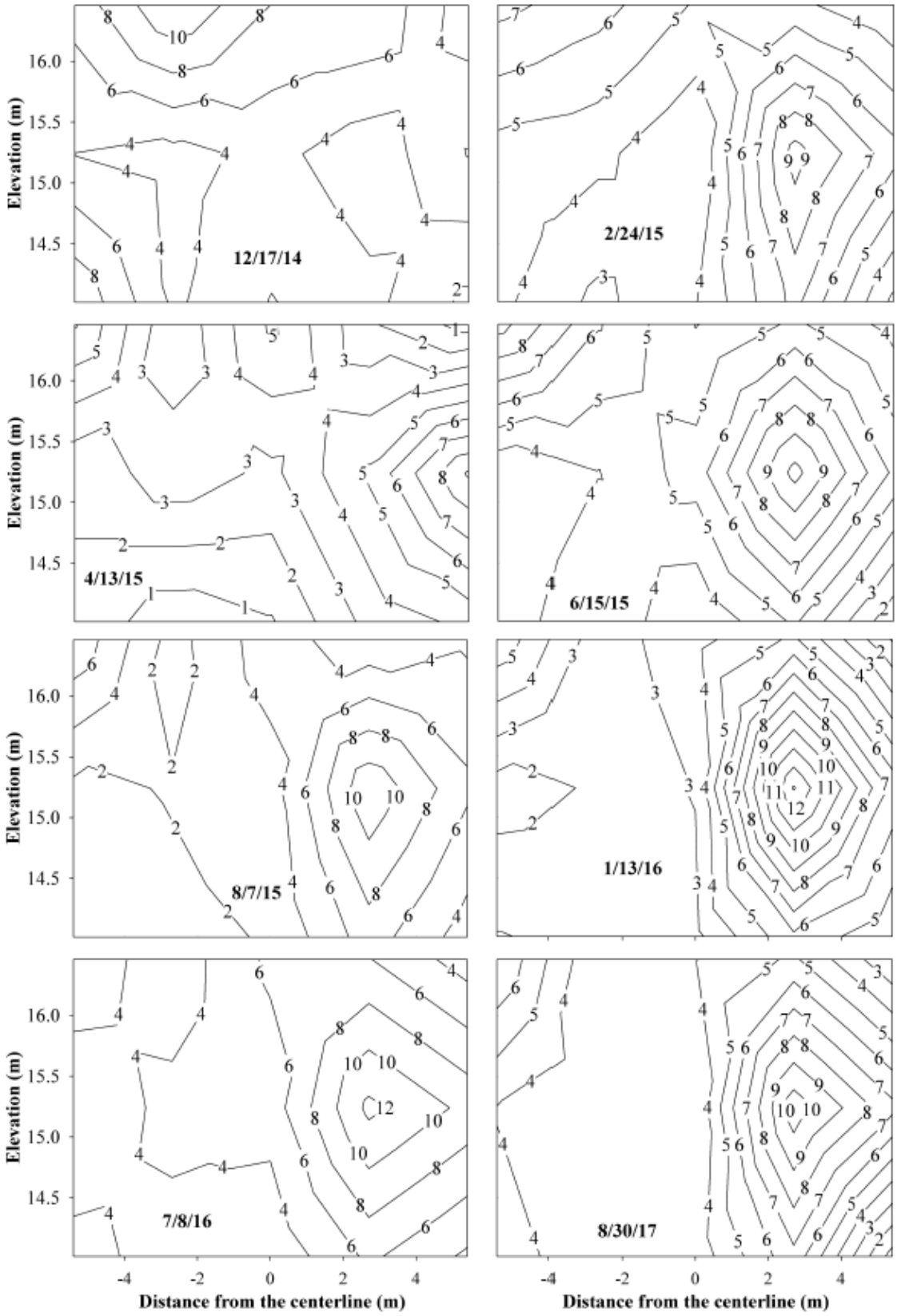

Figure 4.41 Continued

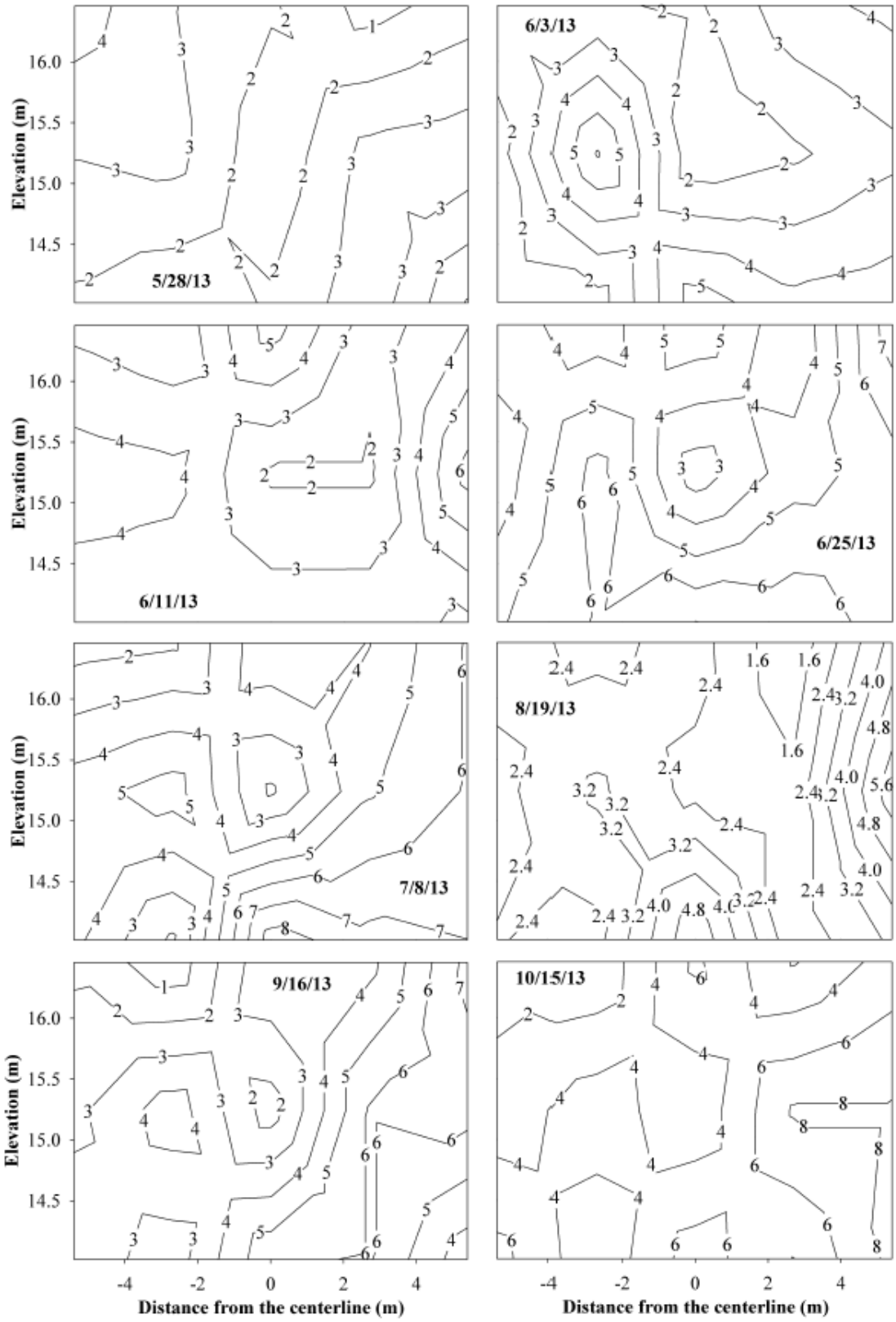

Figure 4.42 Contour plots of the west facing wall deflection over both monitoring periods

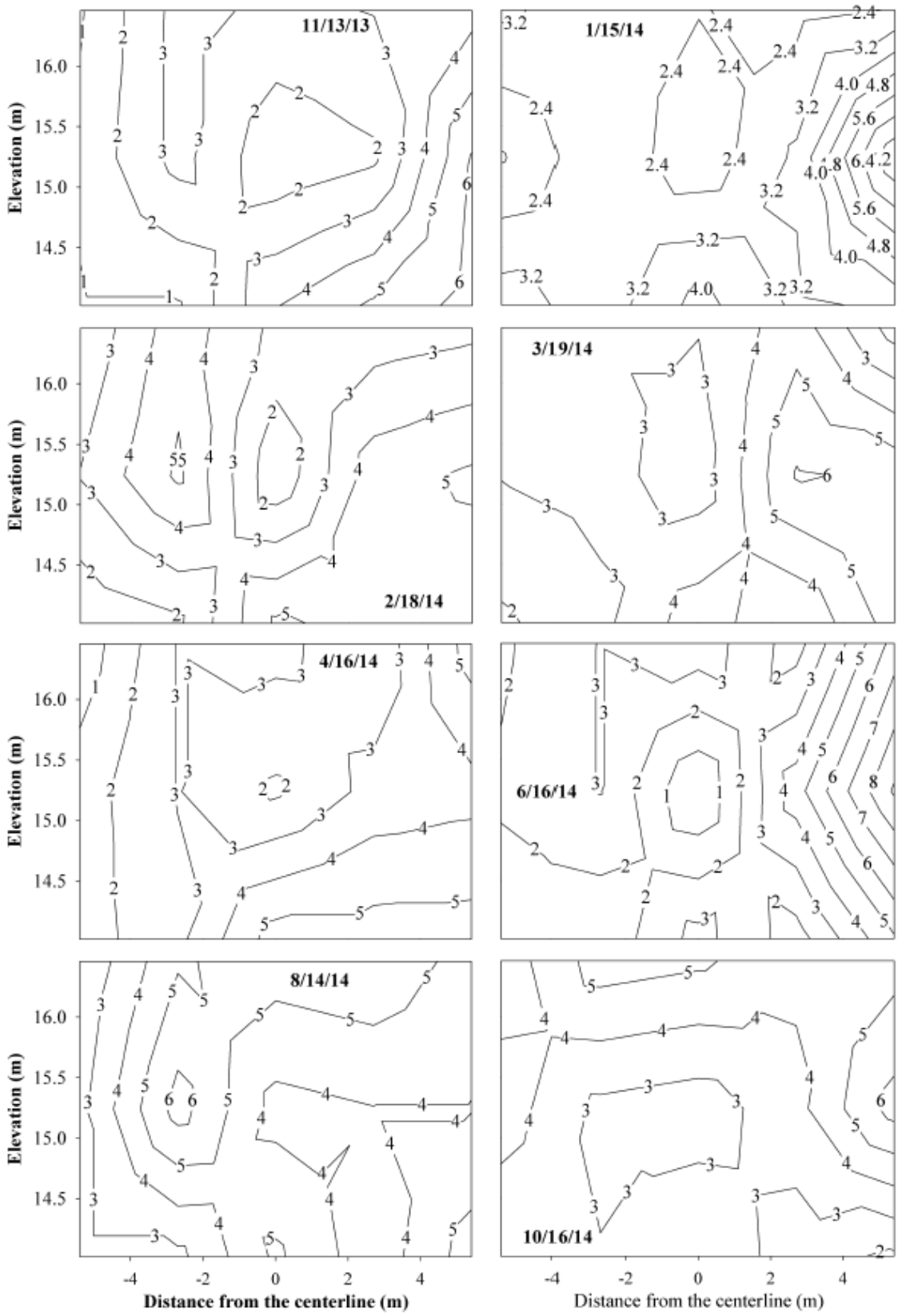

Figure 4.42 Continued

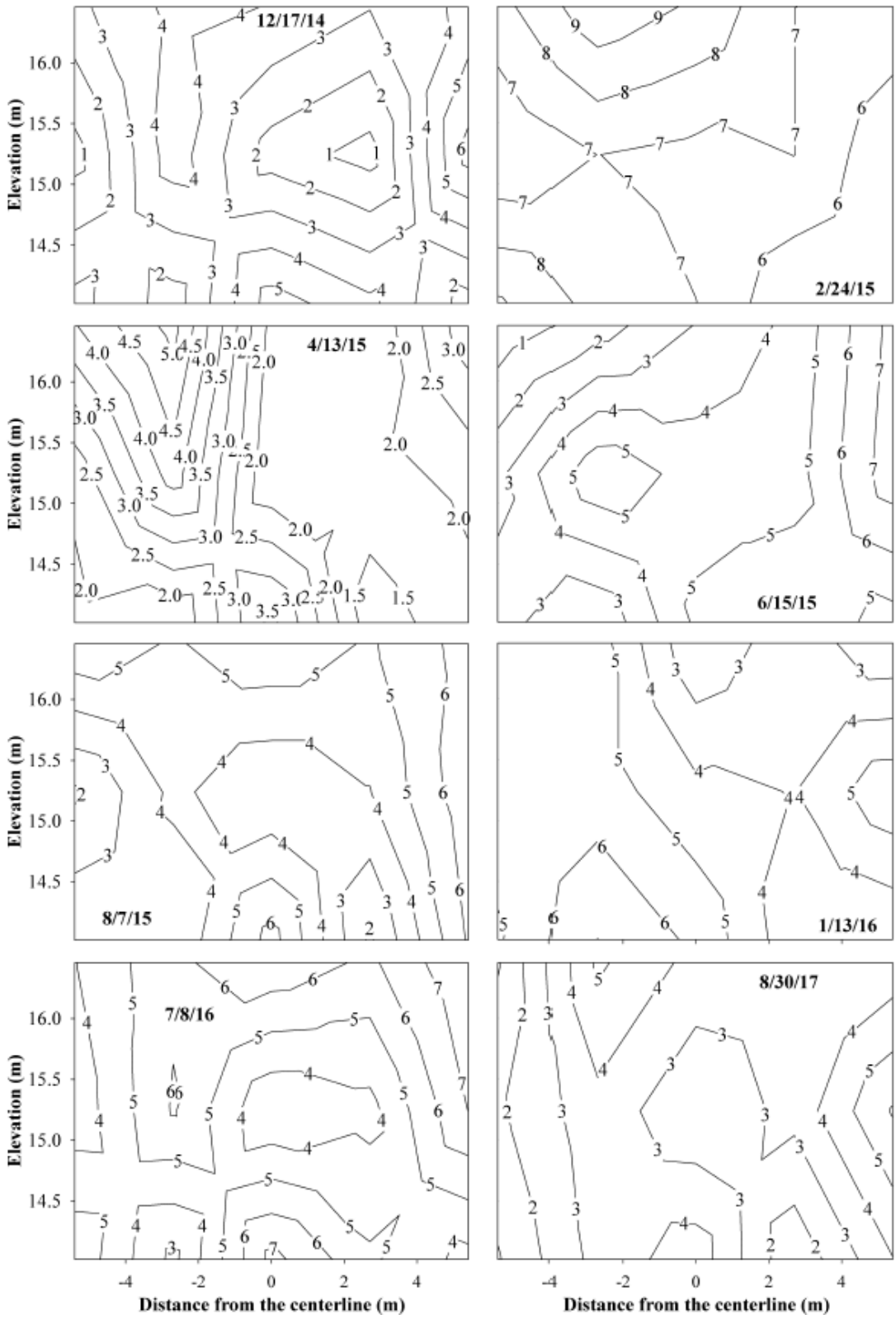

Figure 4.42 Continued

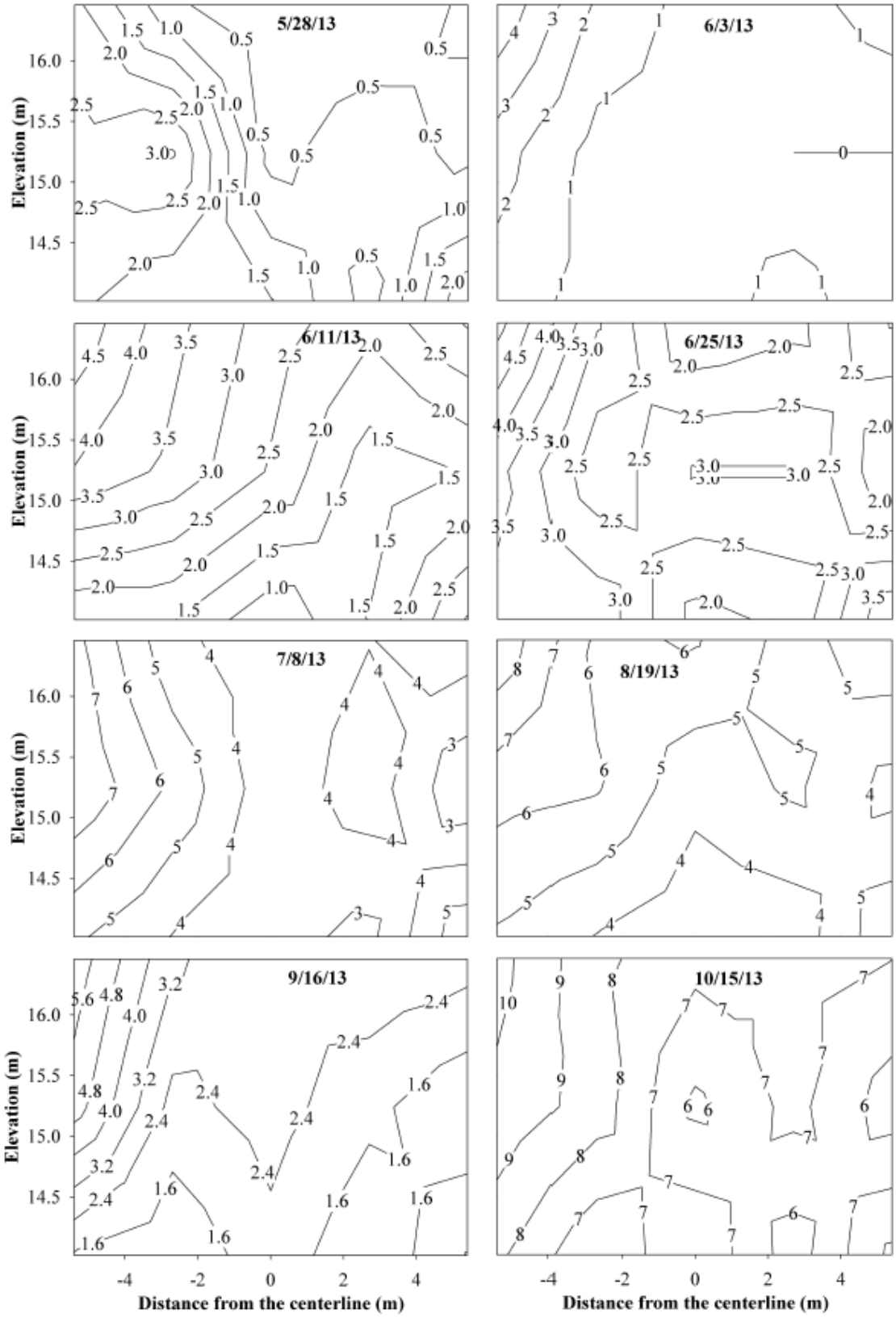

Figure 4.43 Contour plots of the east facing wall settlement over both monitoring periods

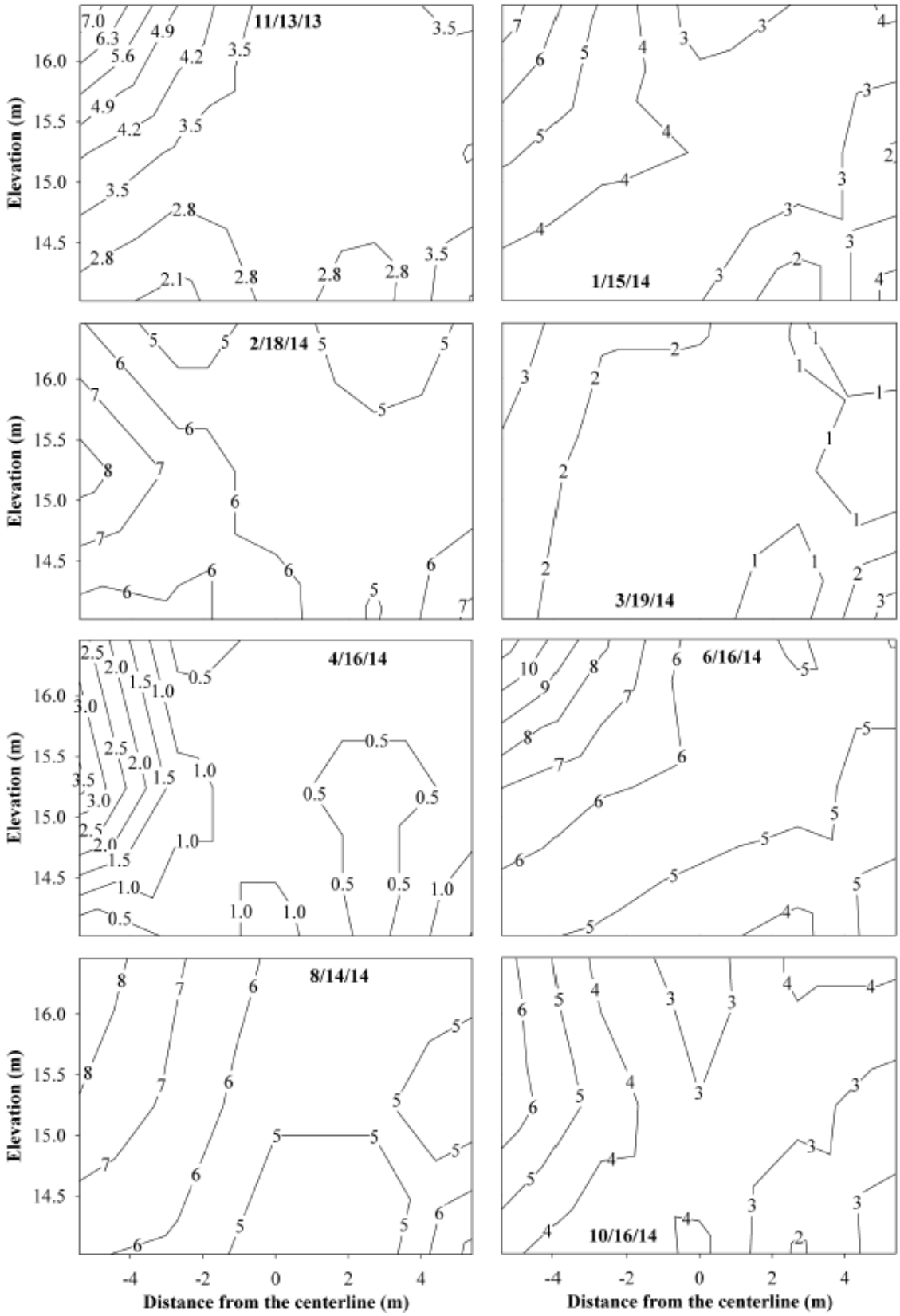

Figure 4.43 Continued

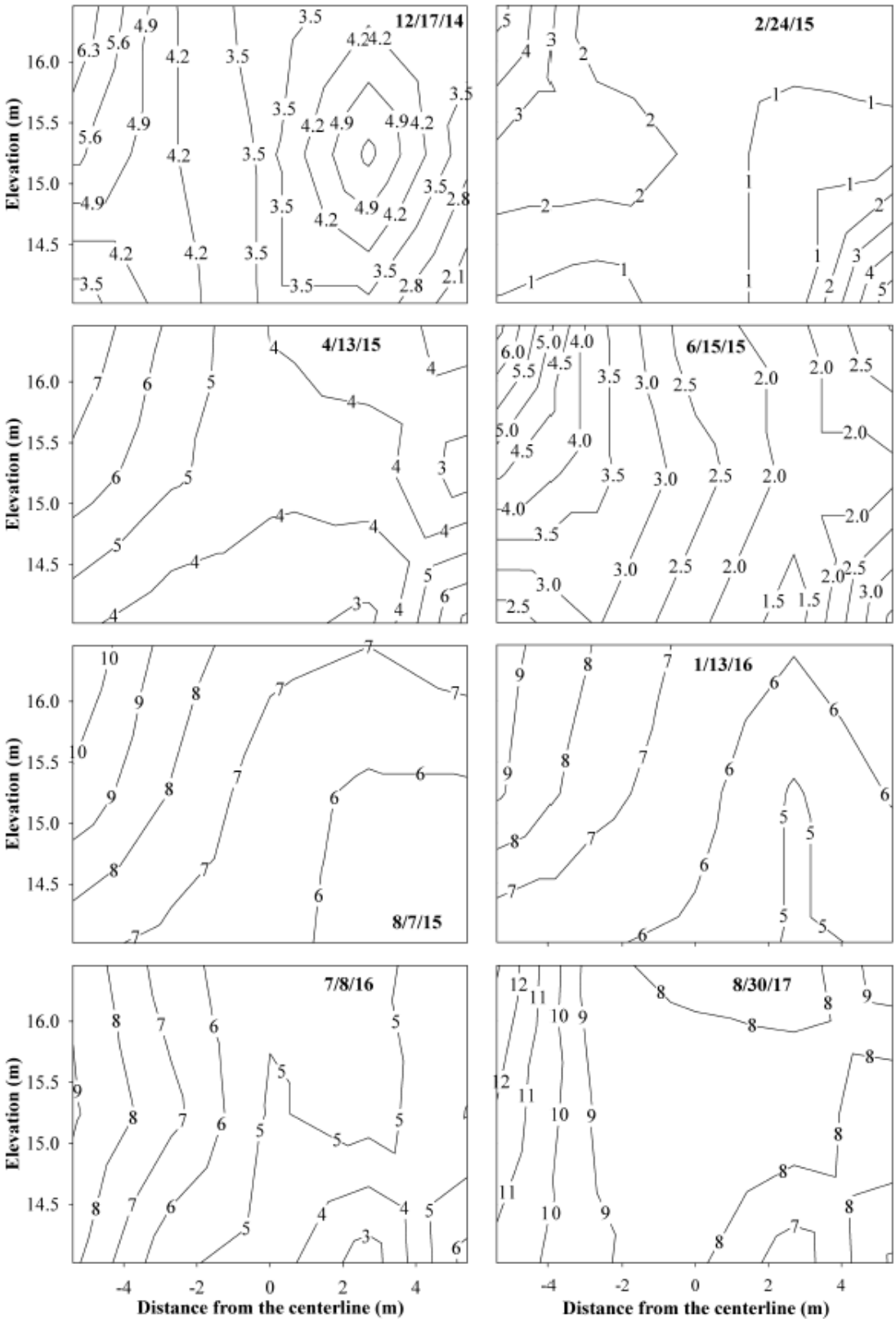

Figure 4.43 Continued

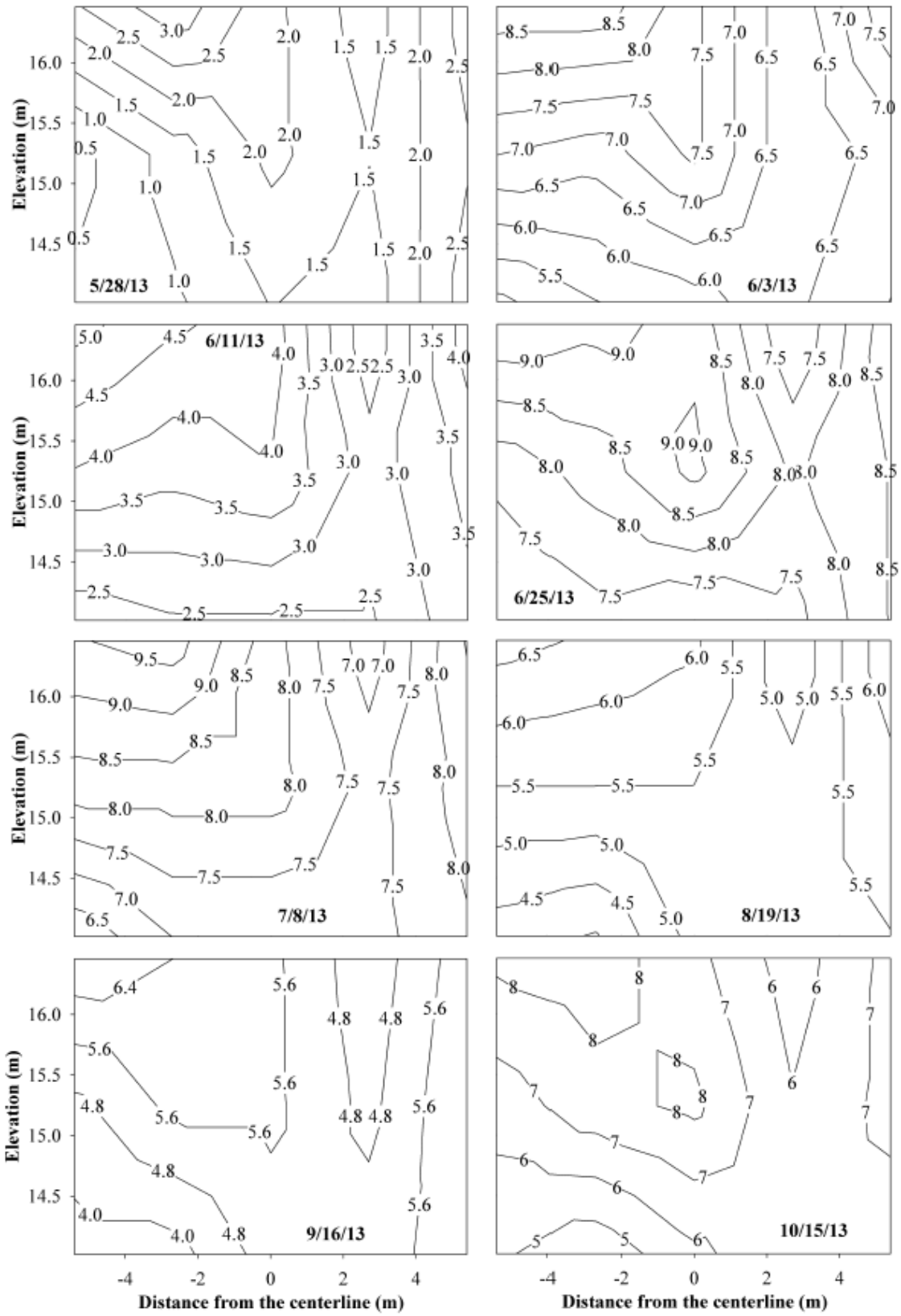

Figure 4.44 Contour plots of the west facing wall settlement over both monitoring periods

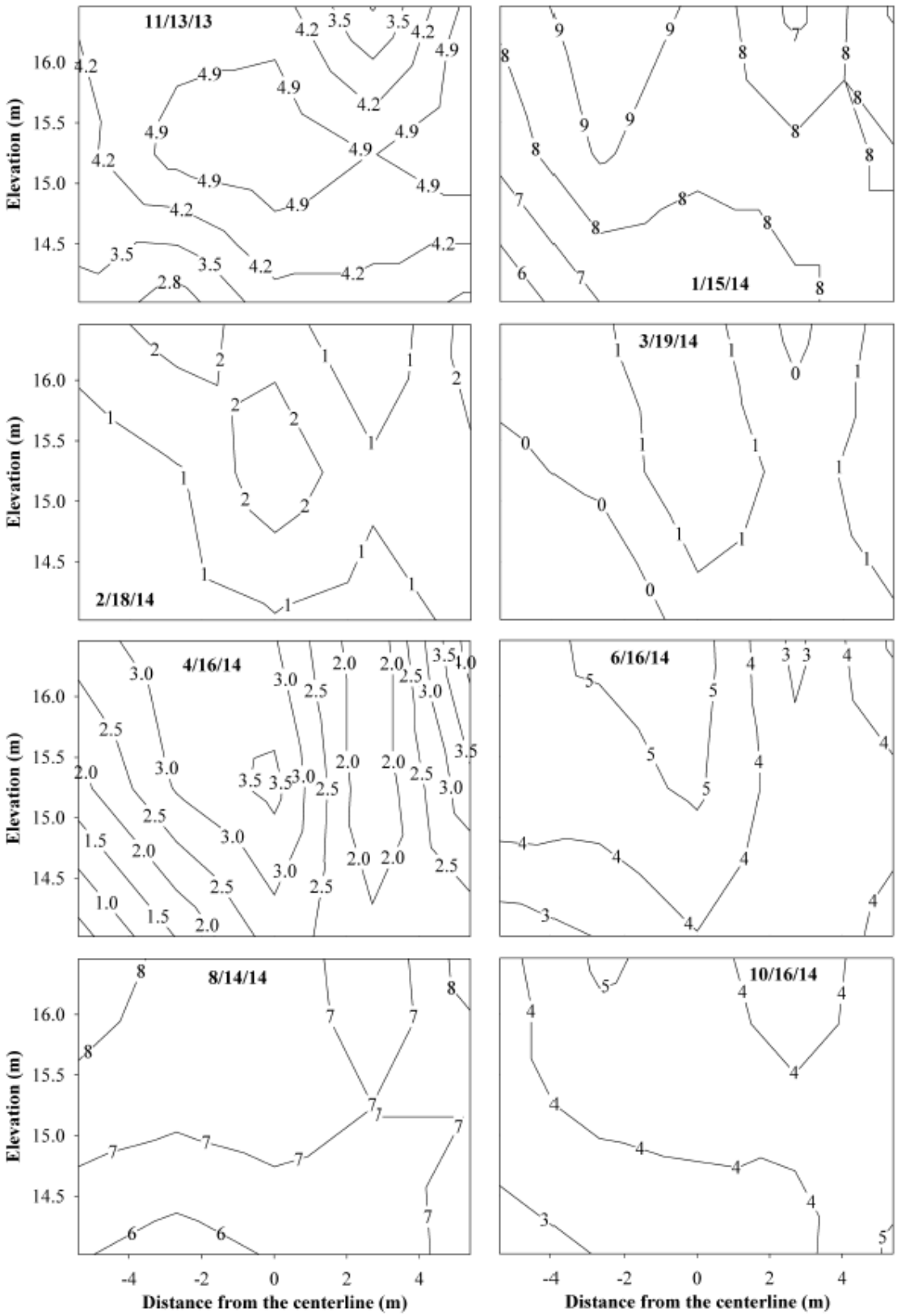

Figure 4.44 Continued

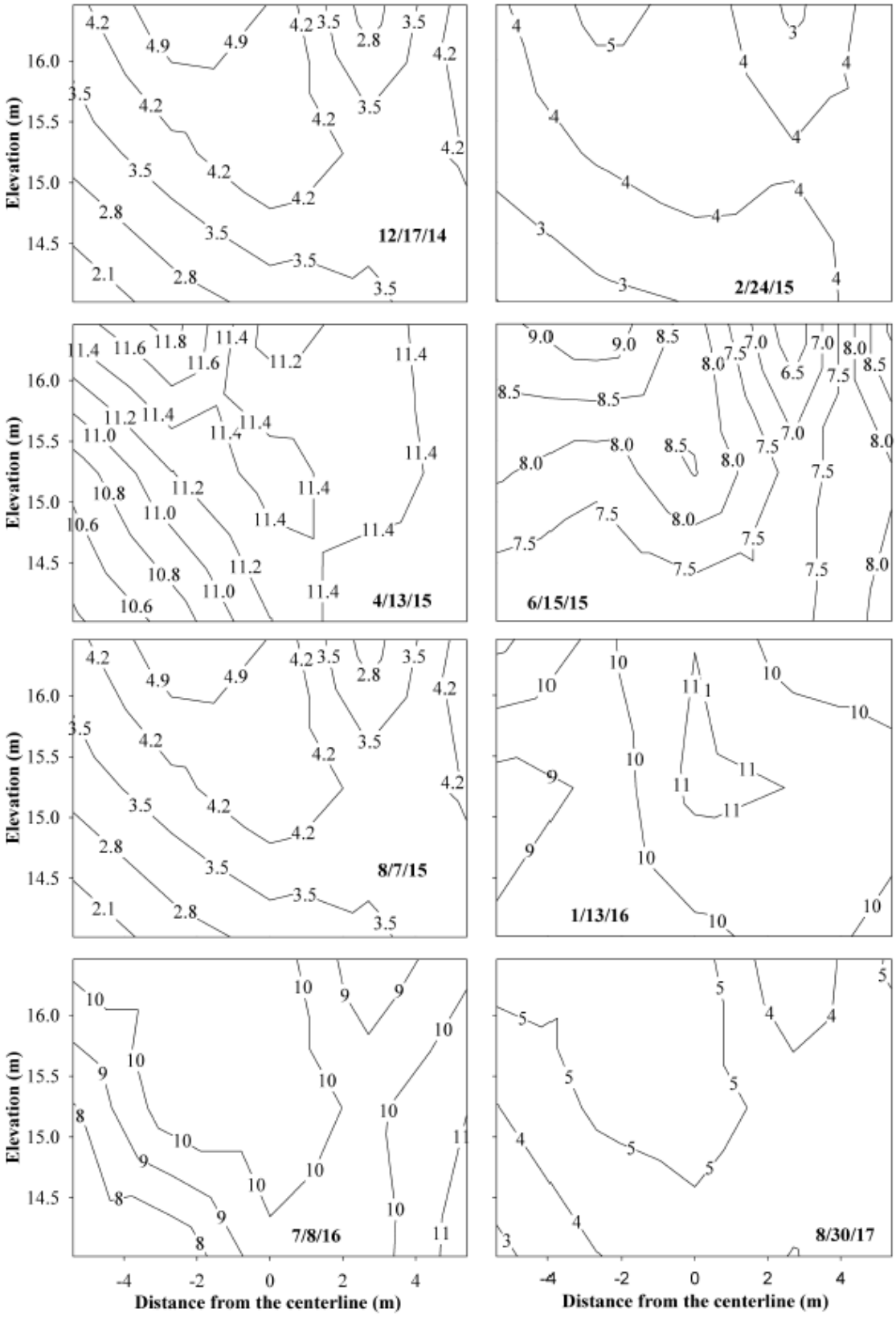

Figure 4.44 Continued

According to the GRS-IBS Interim Implementation guide, the maximum vertical strain should be limited to 0.5% of the height of the structure over the in-service life of the structure (Adams et al. 2011). With a wall height of 4.8 m and a maximum measured settlement of 13 mm, the maximum vertical strain of the GRS abutment was determined to be 0.27%; this is less than the recommended allowable vertical strain.

According to the GRS-IBS Interim Implementation guide, the maximum lateral strain should not exceed 1% (Adams et al. 2011). The calculated maximum lateral strain was 1.18% which is slightly larger than the limit given. Talebi (2016) states that the precision of the surveying operation should be taken into account when interpreting these results as the average deflection was approximately 4 mm. Using 4 mm as the deflection gives a horizontal strain of 0.4% which is in good agreement with the horizontal strains measured by the strain gauges.

Due to the magnitude of the error associated with the surveying operation in comparison with the small deformations being recorded, interpretation of the data was difficult. A regression analysis was used to estimate the actual facing wall deformation over both monitoring periods for each target. Figure 4.45 and 4.46 show the changes in abutment wall lateral deflection over both monitoring periods for the west and east walls respectively. The maximum calculated regression line slope was 0.0032 mm per day. This is equivalent to 1.17 mm per year. The average of the calculated regression line slopes was 0.00064 mm per day (0.23 mm per year). Over both monitoring periods total, 4.25 years, this slope implies that a total of 0.9775 mm of lateral deflection has occurred over this time. Using this lateral deflection to calculate lateral strain, it is determined that the lateral strain is in fact 0.09%. This is in good agreement with the average creep strain measured by the abutment strain gauges of approximately 0.1%. After the first monitoring

period, the average slope was determined to be 0.38 mm per year so there are no signs that there is an increase in lateral deflection over this current monitoring period.

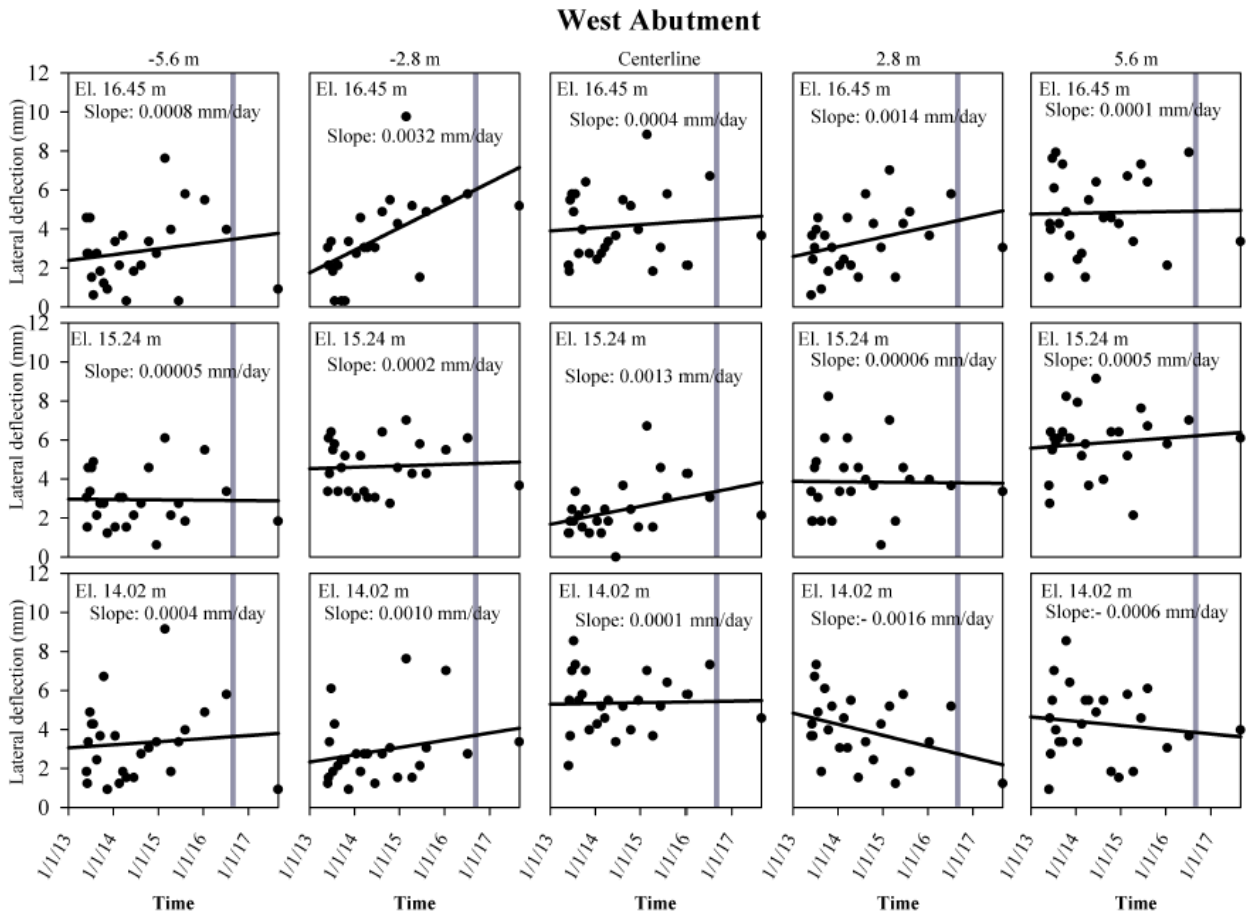

Figure 4.45 Changes in the west abutment wall lateral deflection over both monitoring periods

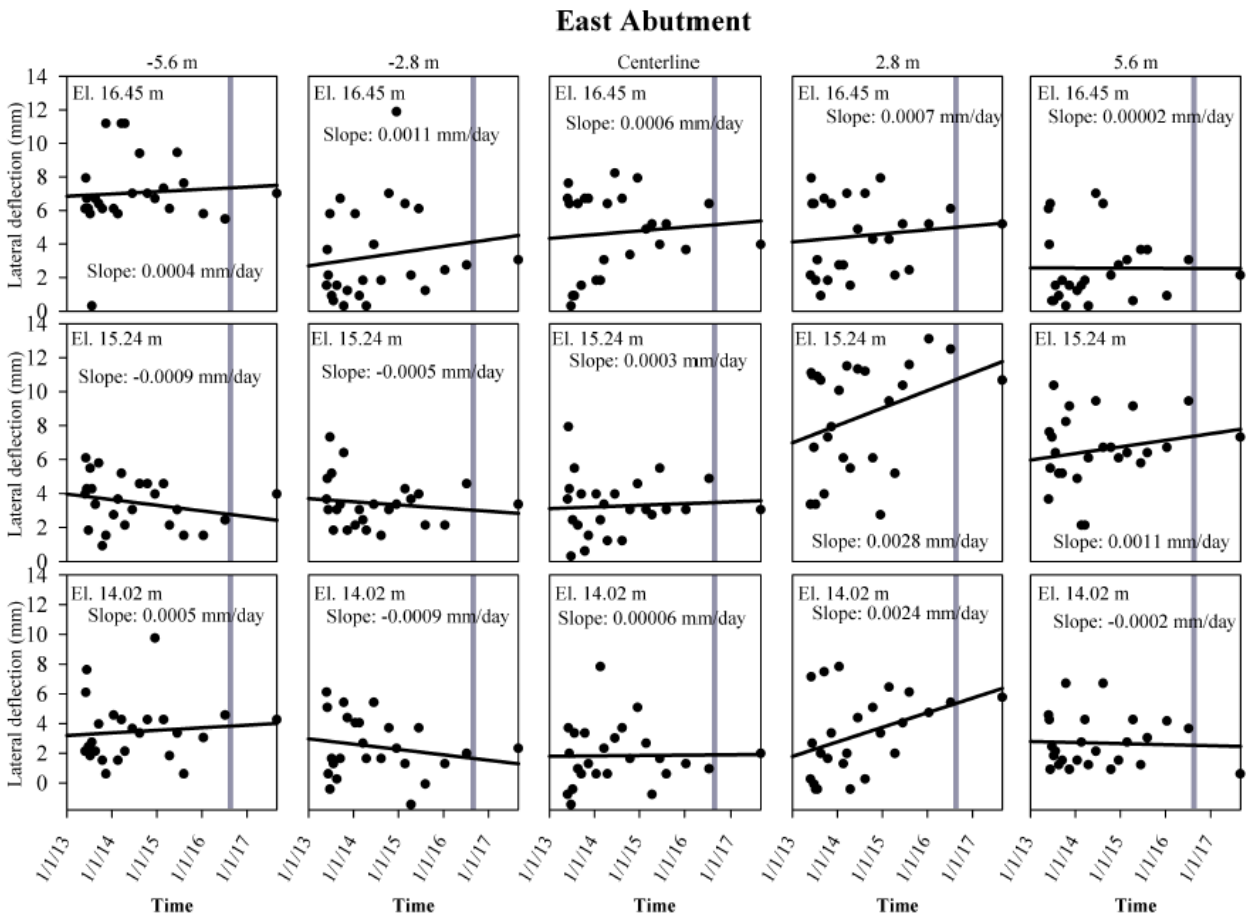

Figure 4.46 Changes in the east abutment wall lateral deflection over both monitoring periods

A regression analysis was also used to estimate the facing wall settlement over both monitoring periods for each target. Figures 4.47 and 4.48 show the changes in abutment wall settlement over both monitoring periods for the west and east walls respectively. A maximum regression line slope of 0.0039 mm per day (1.42 mm per year) was calculated. The average of the calculated regression line slopes was 0.0025 mm (0.91 mm per year). Over both monitoring periods, this implies a total average settlement of 3.868 mm has occurred. This shows an increase in approximately 0.5 mm from what was calculated after the first monitoring period.

Estimated slopes of 0.91 mm per year for settlement and 0.23 mm per year for lateral deflection combined with maximum settlement and lateral deflection values of approximately 13 mm suggest there is very little overall deformation of this structure.

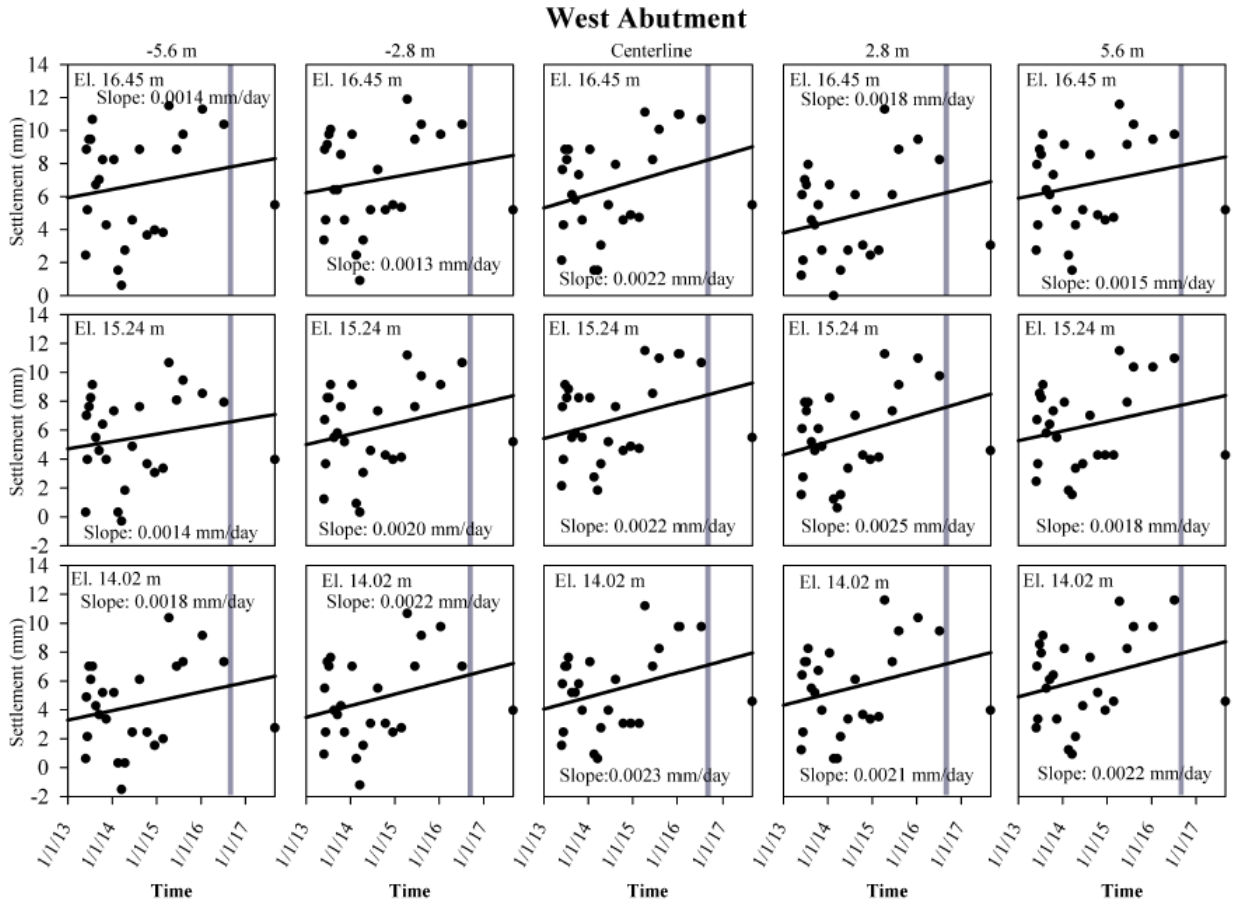

Figure 4.47 Changes in the west abutment wall settlement over both monitoring periods

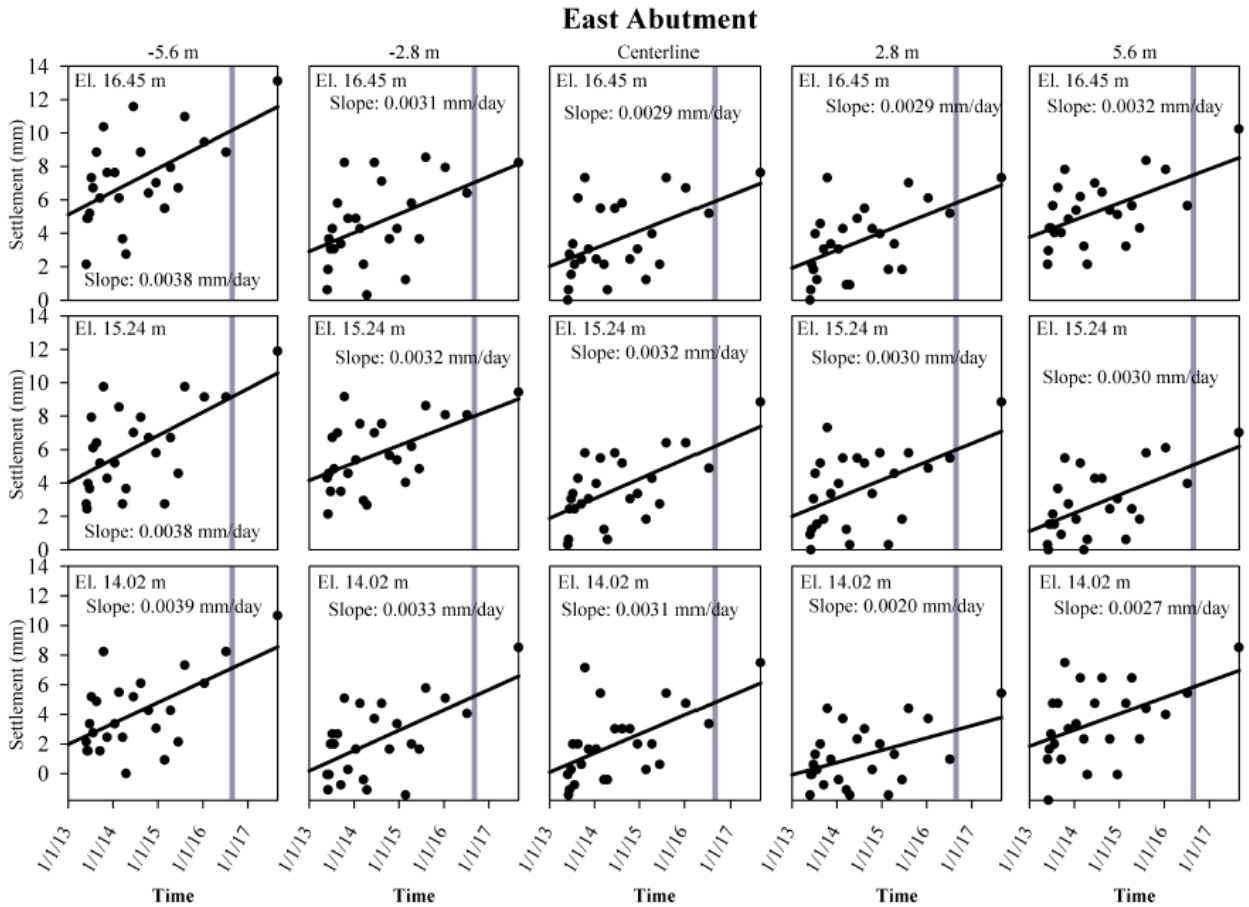

Figure 4.48 Changes in the east abutment wall settlement over both monitoring periods

4.2.6 Inclinometer Sensors

As discussed in Chapter 3, four in-place inclinometer sensors were installed in the clay foundation to measure its displacement. Figure 4.49 and 4.50 present the foundation deformation during construction, live load testing, and both monitoring periods in the E-W and N-S direction respectively. Significantly more noise is seen in the N-S direction relative to the E-W direction since for "biaxial" in-place inclinometer sensors, the A direction readings are always more stable than the B direction because the wheels are on the same plane as the A direction (Talebi 2016). Readings from this monitoring period for lateral deflection in the E-W direction are very consistent with what was observed in the first monitoring period; however, there was a sudden and unexpected shift for sensors In-1 and In-2 at the end of this current monitoring period. This observed movement is not expected to be a significant issue over time since the overall magnitude of movements is still very small, and the movements appear to have stabilized after this point. Some creep deformation in this direction was also observed but only on the order of about 1.0 mm. A maximum deflection of approximately 14 mm was seen in the E-W direction.

For the N-S direction, significantly more variation was seen during this monitoring period than the previous, although it seemed to start at the end of the first monitoring period, around August of 2016; this should continue to be monitored. Typically, the large spikes dissipate after some time. A maximum deflection of approximately 15 mm was seen in this direction and slightly more creep developed, approximately 2 mm, compared to the E-W direction. Overall, with maximum deflections of 14 and 15 mm and with creep on the magnitude of 2 mm, it can be determined that no significant movement has occurred in the clay foundation.

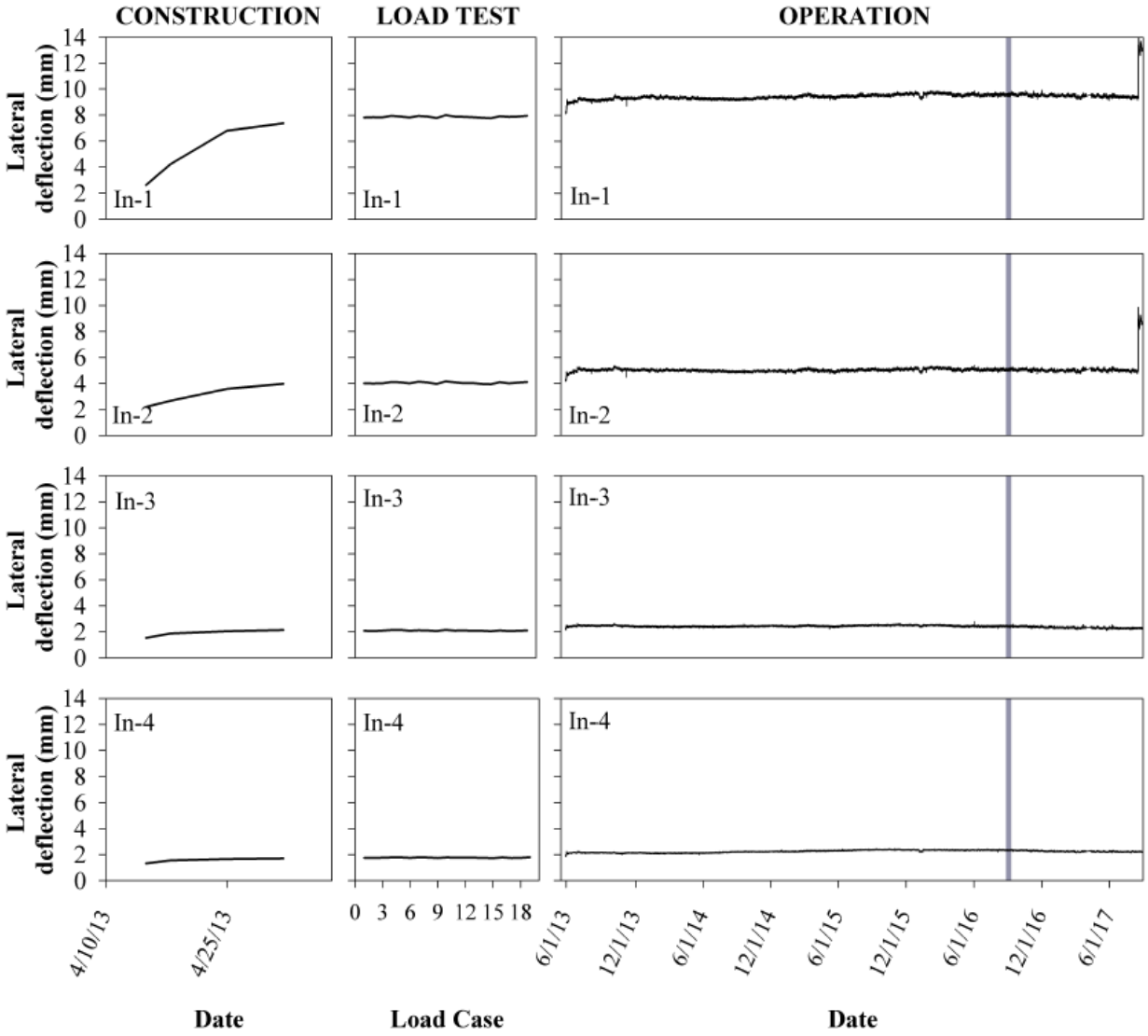

Figure 4.49 Lateral deflection in the E-W direction recorded by the inclinometer sensors

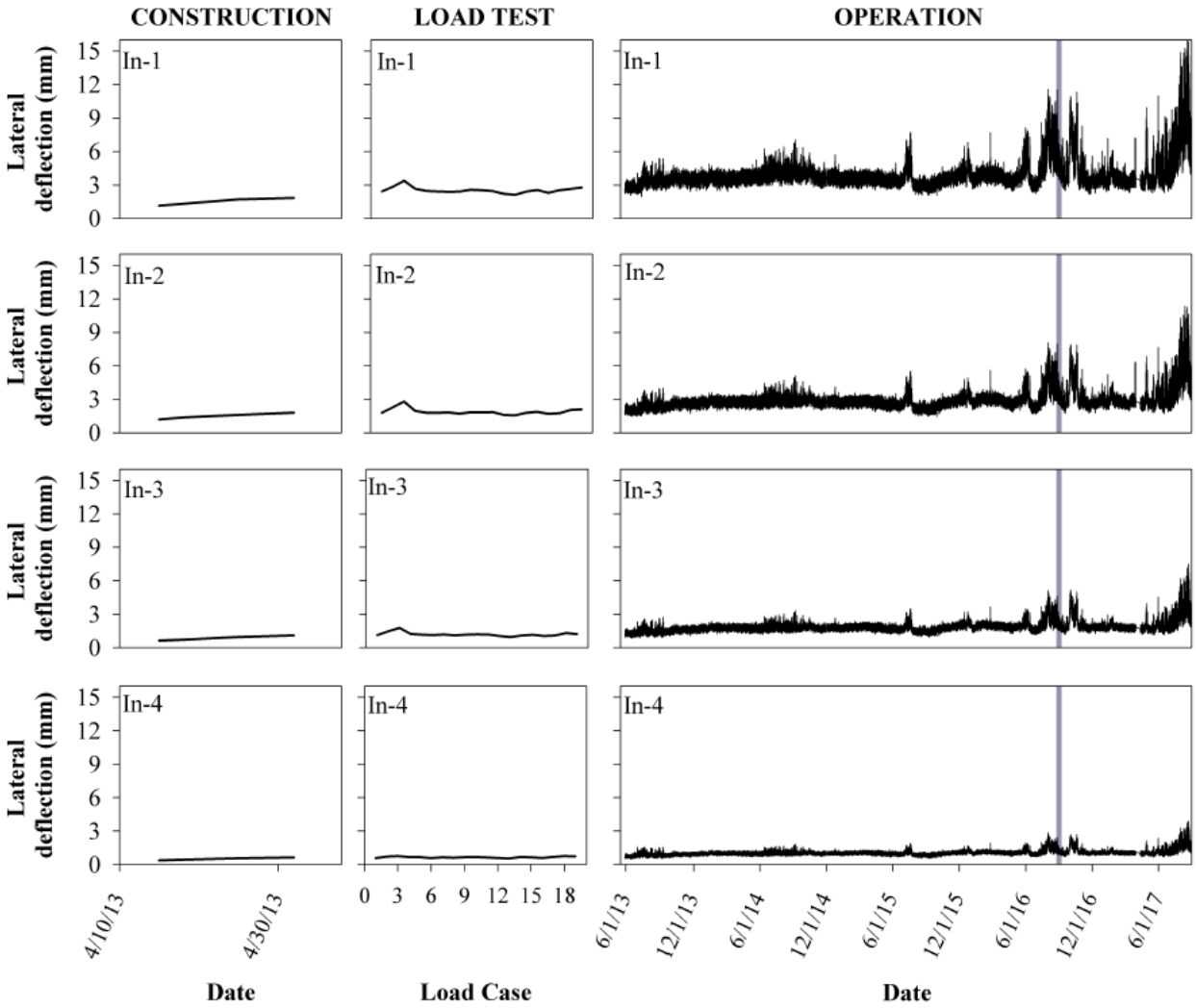

Figure 4.50 Lateral deflection in the N-S direction recorded by the inclinometer sensors

Initial and final foundation deflection readings in the E-W direction for both monitoring periods and the current monitoring period are presented in Figure 4.51 and 4.52 respectively. As mentioned above, sensors In-1 and In-2 showed abnormal readings at the end of this current monitoring period so the final readings show a large difference from the initial. This should continue to be monitored. Figures 4.53 and 4.54 show the initial and final foundation deflection readings in the N-S direction for both monitoring periods and the current monitoring period respectively. Again, as mentioned above significant variation was seen at the end of this

monitoring period and this is expected to dissipate over time so these figures show a large difference between the initial and final readings.

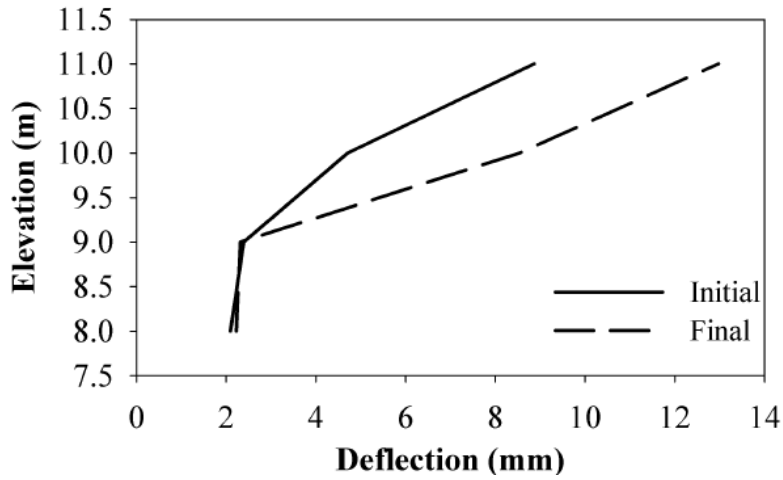

Figure 4.51 Initial and final foundation deflection in the E-W direction for both monitoring periods

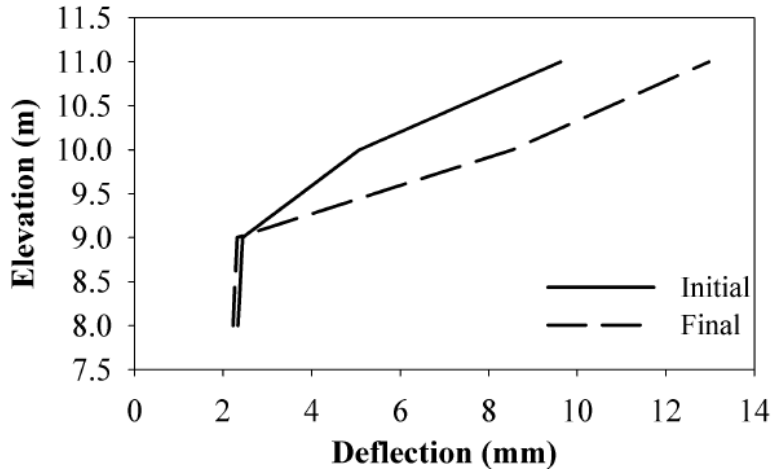

Figure 4.52 Initial and final foundation deflection in the E-W direction for the current monitoring period

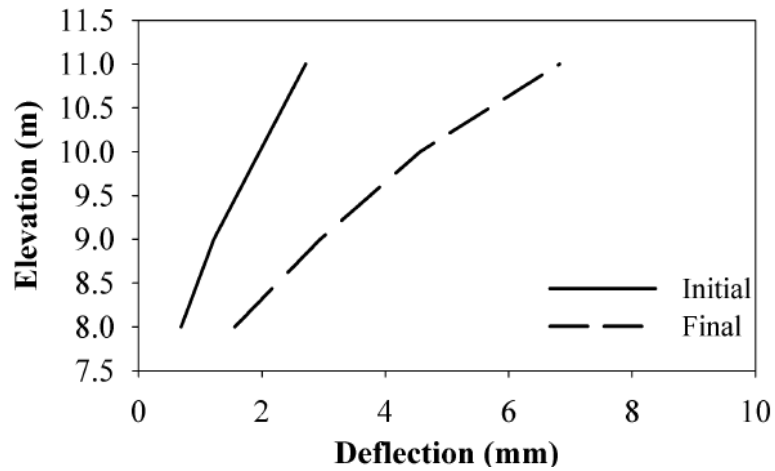

Figure 4.53 Initial and final foundation deflection in the N-S direction for both monitoring periods

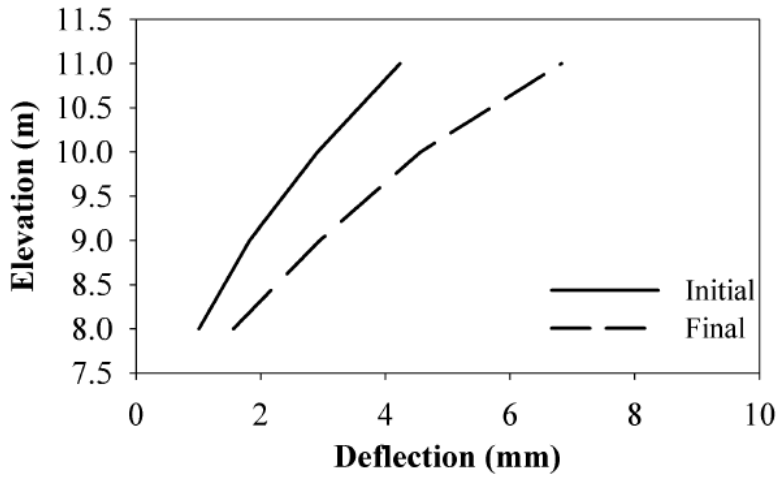

Figure 4.54 Initial and final foundation deflection in the N-S direction for the current monitoring period

4.2.7 Foundation Pressure Cells

Readings from the four-vibrating wire static pressure cells installed beneath the GRS-IBS foundation were collected during construction, live load testing, and both monitoring periods as shown in Figure 4.55. The most recent monitoring period shows consistent readings with what was observed in the previous monitoring period. The vibrating wire pressure cells only measure total stress, which is a combination of effective stress and pore-water pressure. To combat this, data from the piezometers was used to calculate effective stresses for both monitoring periods, as shown in Figure 4.56. As stated in Talebi (2016) it is important to calculate the effective pressure because the long-term stability of the soil is governed by effective stress.

In both figures, a significant amount of noise can be seen and the data also fluctuated seasonally. Figures 4.57 and 4.58 present the minimum, average, and maximum recorded effective pressure for both monitoring periods combined and this current monitoring period respectively. As expected, a larger scatter of data is shown for both monitoring periods (Figure 4.57), since data is being observed for approximately 51 months compared to just the current monitoring period of 12 months. Histograms of the measured effective pressure for both monitoring periods combined and the most recent monitoring period are shown in Figures 4.59 and 4.60, respectively. Similar trends can be seen in both figures in regards to shape of the distribution, spread of the data, and average. As discussed in Talebi (2016) and Talebi et al. (2017), the pressure distribution beneath the foundation was not uniform. This is shown in Figures 4.57 and 4.58 as the maximum pressure was observed at the location of sensor S2, which was installed beneath the facing wall; the minimum occurred at the location of sensor S1, which was installed at the toe of the foundation.

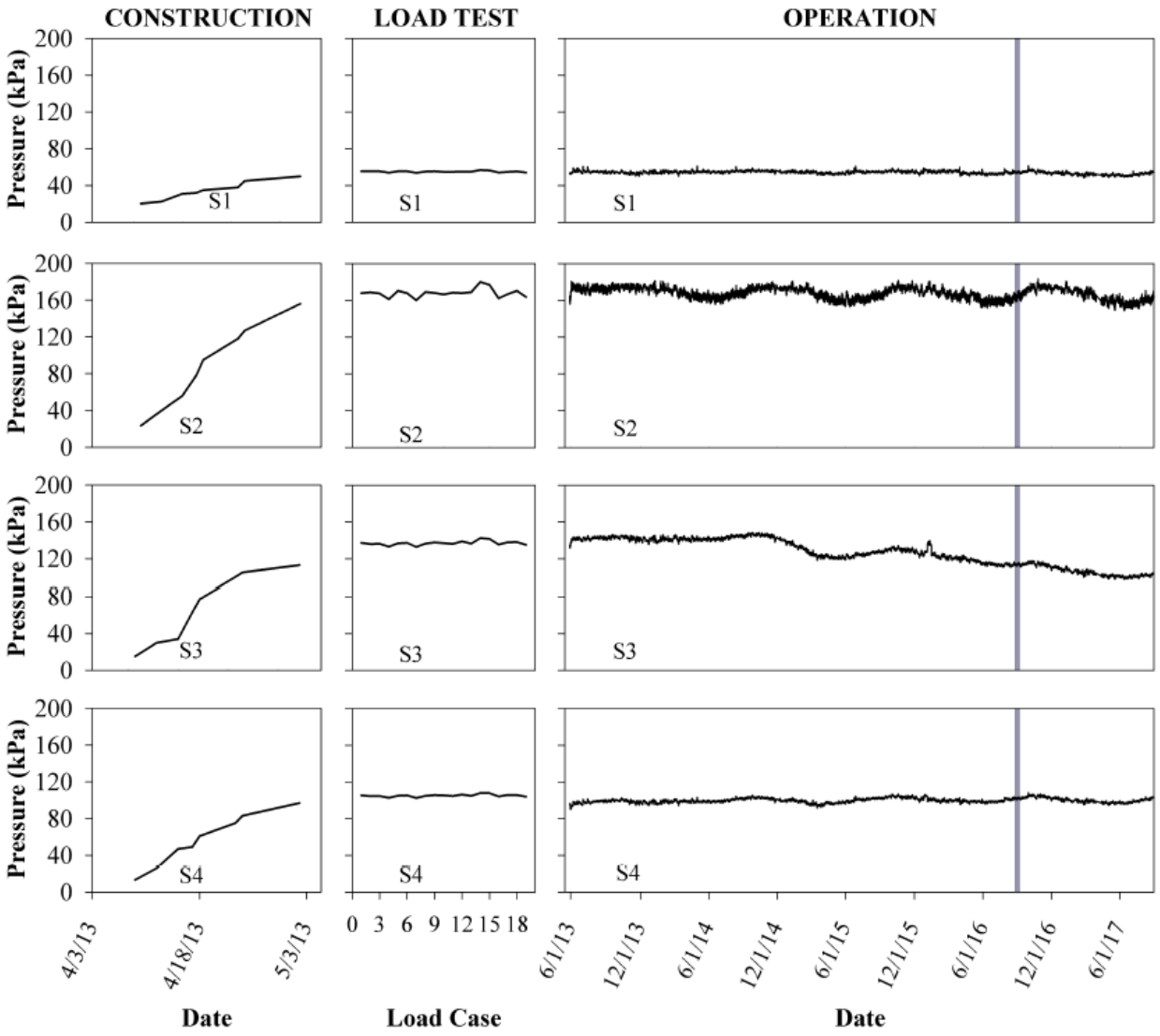

Figure 4.55 Measured total pressures

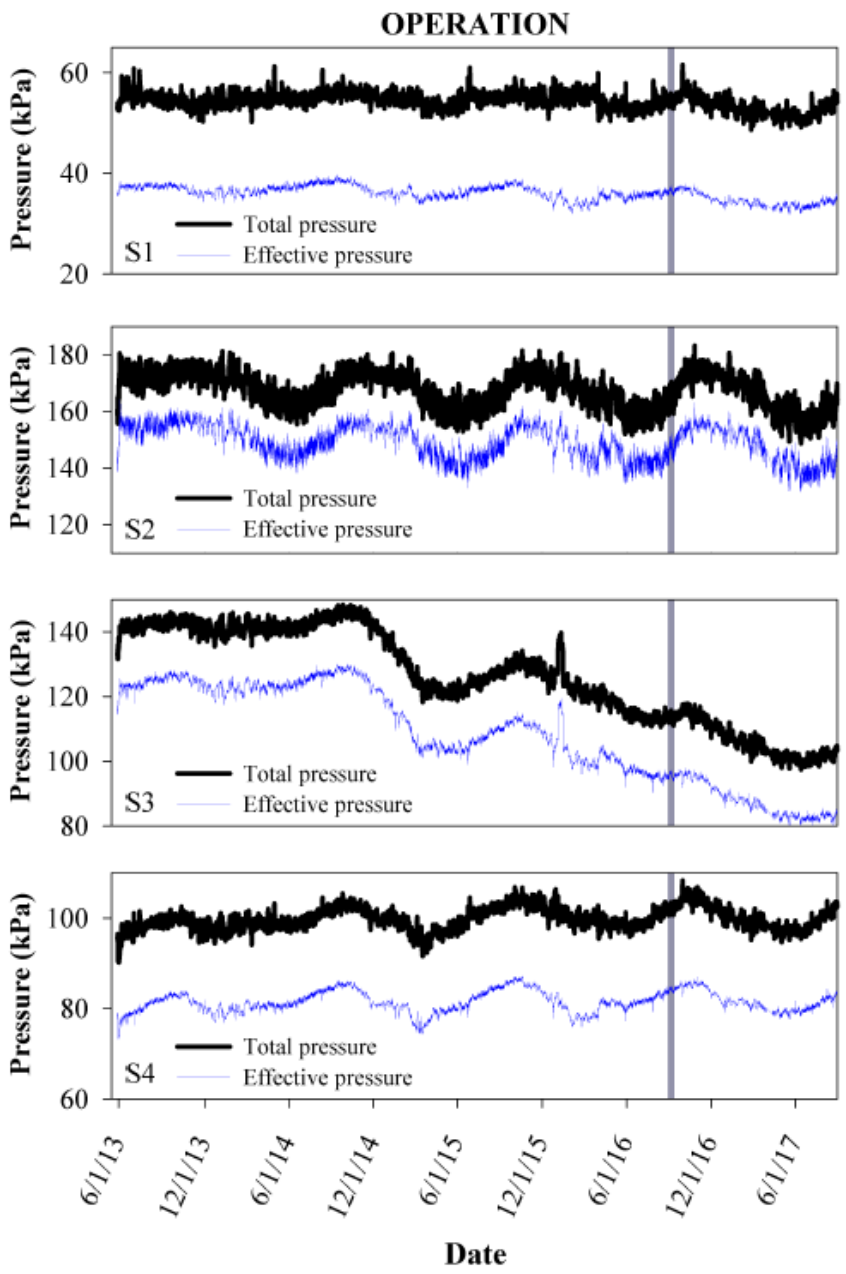

Figure 4.56 Measured total and effective pressures

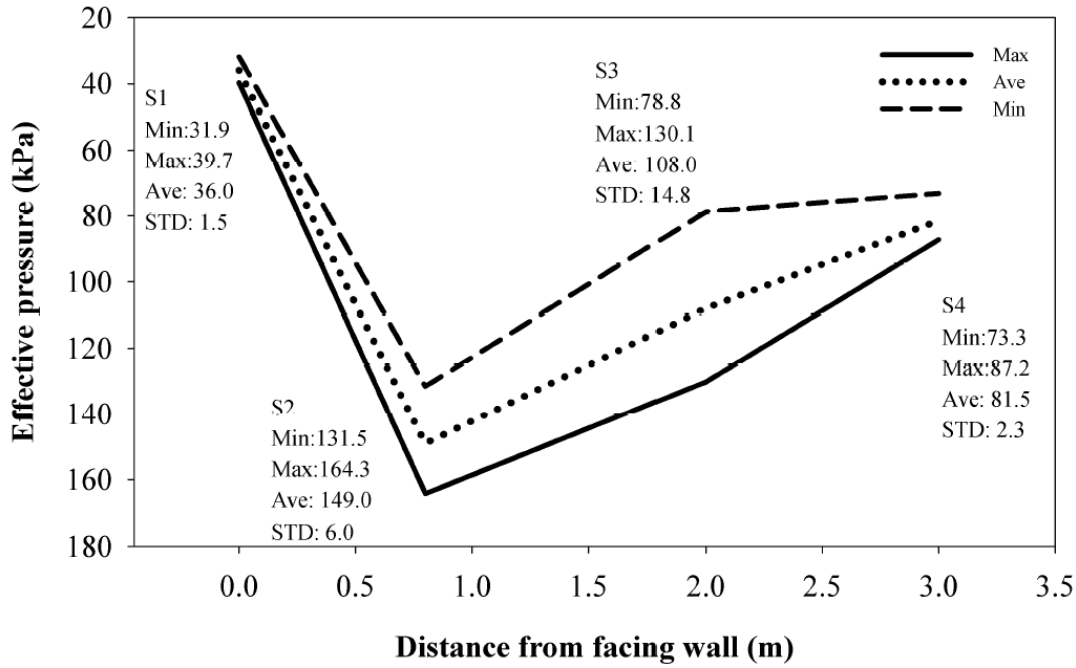

Figure 4.57 Changes in effective pressure distribution beneath the RSF for both monitoring periods

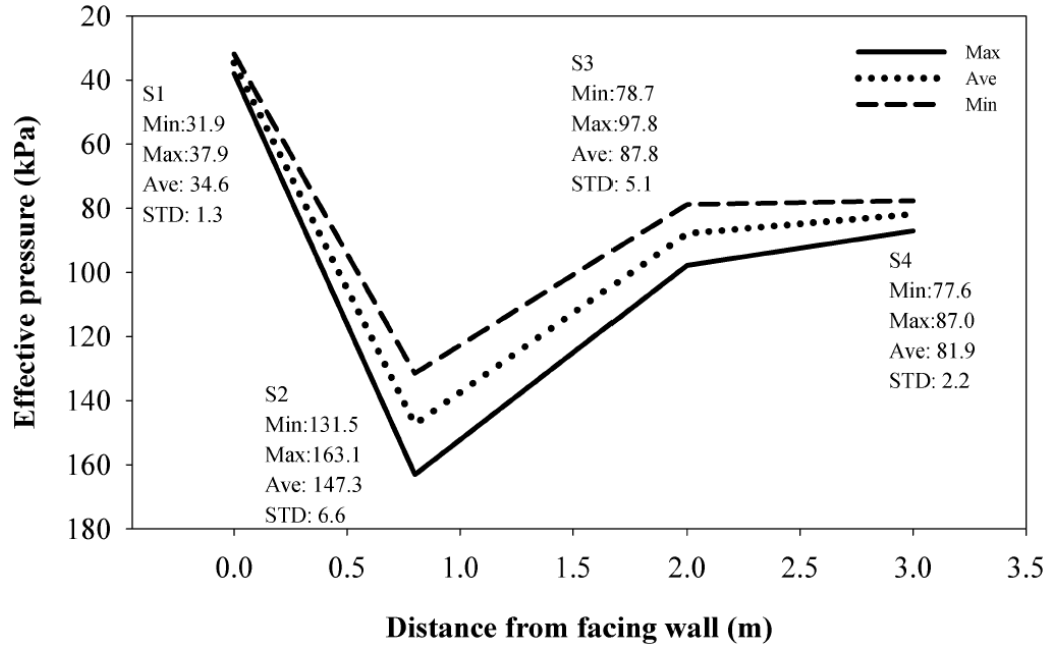

Figure 4.58 Changes in effective pressure distribution beneath the RSF for the current monitoring period

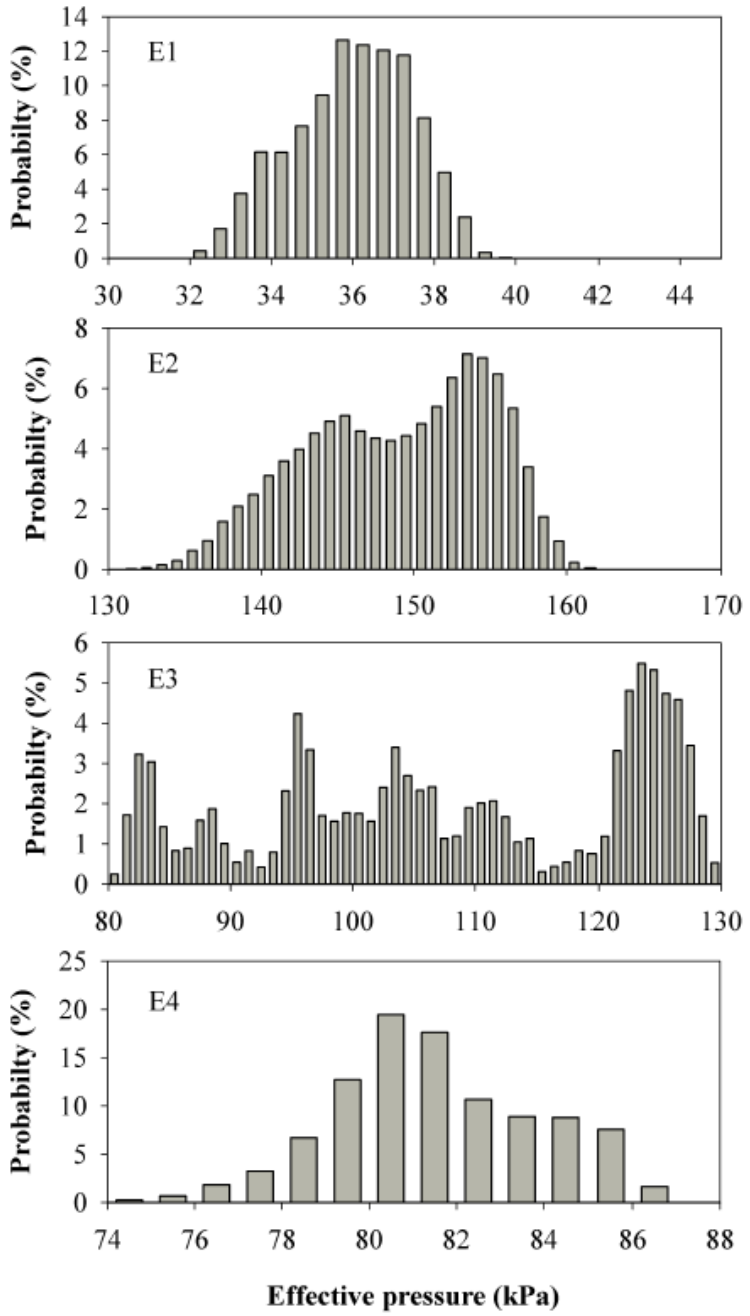

Figure 4.59 Histogram of effective pressure for both monitoring periods

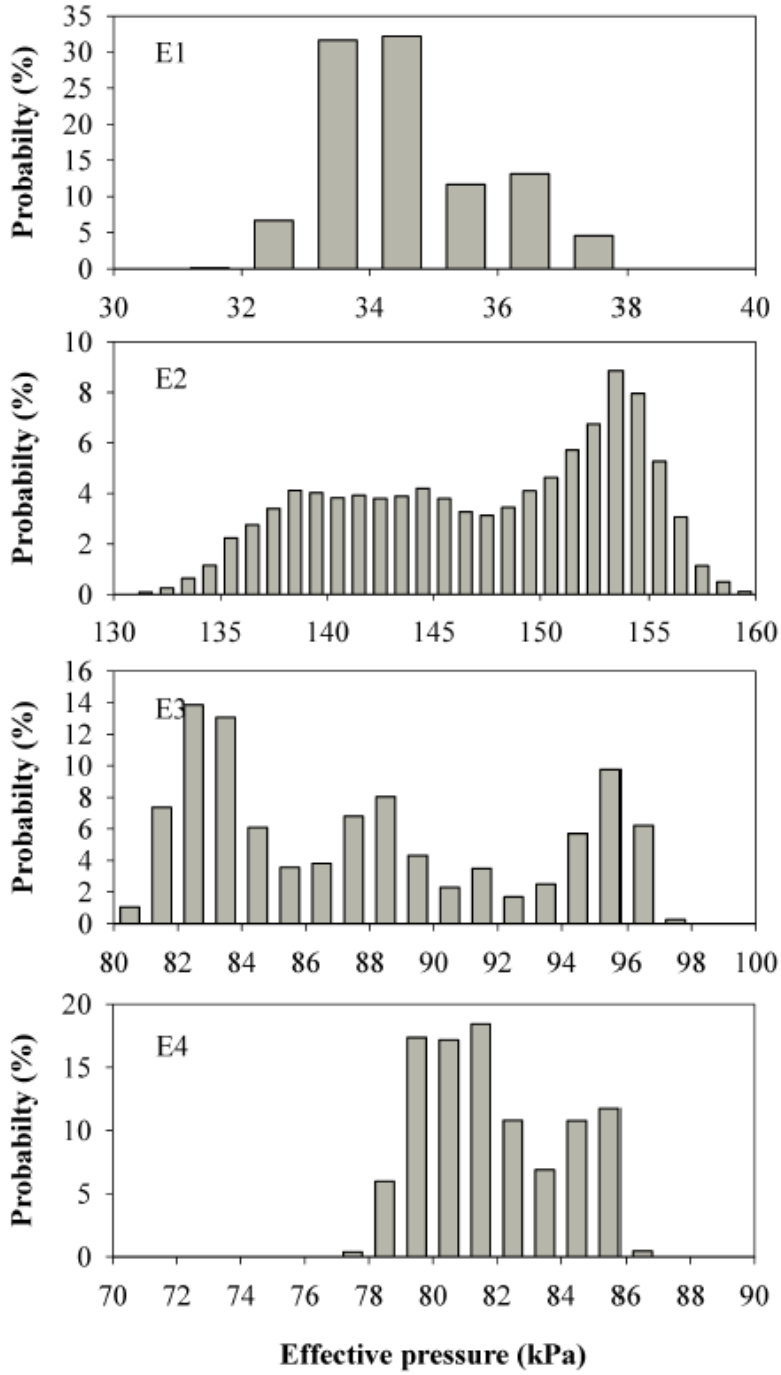

Figure 4.60 Histogram of effective pressure for the current monitoring period

Talebi (2016) also discusses in depth about how readings from the vibrating wire pressure cells are influenced by ground temperature. It is described how the trends for measured pressure and cell temperature are similar as one can see the seasonal fluctuations in Figure 4.55. A

regression analysis was initially conducted to investigate the correlation between the effective pressure and cell temperature. Talebi (2016) concluded that a direct correlation exists; increases in cell temperature corresponds to an increase in cell pressure and vice versa. This analysis also showed the slope of the correlation changes in hot and cold weather and the slope is higher when the temperature increases; the results show that the cells respond differently to the temperature changes in hot and cold weather. The overall conclusion was that the cell temperature change can significantly affect the pressure reading. For more details see section 9.2.7.1 of Talebi (2016).

The pressure cells utilized in this project are also affected by air temperature; this appears as the noise in Figure 4.56 (Talebi 2016). Through regression analysis, it was concluded that the daily correlation coefficient between the air temperature and foundation pressure was mostly negative, thus indicating an inverse relationship (Talebi 2016).

The factor of safety against foundation bearing capacity failure did not change over this current monitoring period as the maximum applied pressure recorded was during the first monitoring period; the factor of safety is still approximately 3.1; this is a conservative assumption because it assumes the maximum applied pressure is applied continuously at all times (Talebi 2016).

4.2.8 Abutment Pressure Cells

Three pressure cells were also installed in the west abutment to measure induced pressures as described in Chapter 3. These pressure cells are capable of measuring instantaneous pressures produced by live loads on the road provided a data logger with high frequency of data collection is used. The greater noise seen in these sensors is attributed to their use of foil strain gauge technology instead of vibrating wire strain gauge technology within the cell's pressure transducer,

which is much more susceptible to changes in ambient temperature conditions. Figure 4.61 displays the changes in abutment pressure during construction, live load testing, and both monitoring periods. Readings for the current monitoring period are nearly identical to the previous monitoring period. This is further illustrated by the histograms of abutment pressures for both monitoring periods and the current monitoring period as shown in Figures 4.62 and 4.63, respectively. The histograms show very similar shape, range, and average. This is reiterated in the minimum, average, and maximum plots shown in Figures 4.64 and 4.65 for both monitoring periods and the current monitoring period, respectively. Similar to the readings from the foundation pressure cells, the pressure changes seasonally. These fluctuations imply that temperature influences the measured values from the pressure cells.

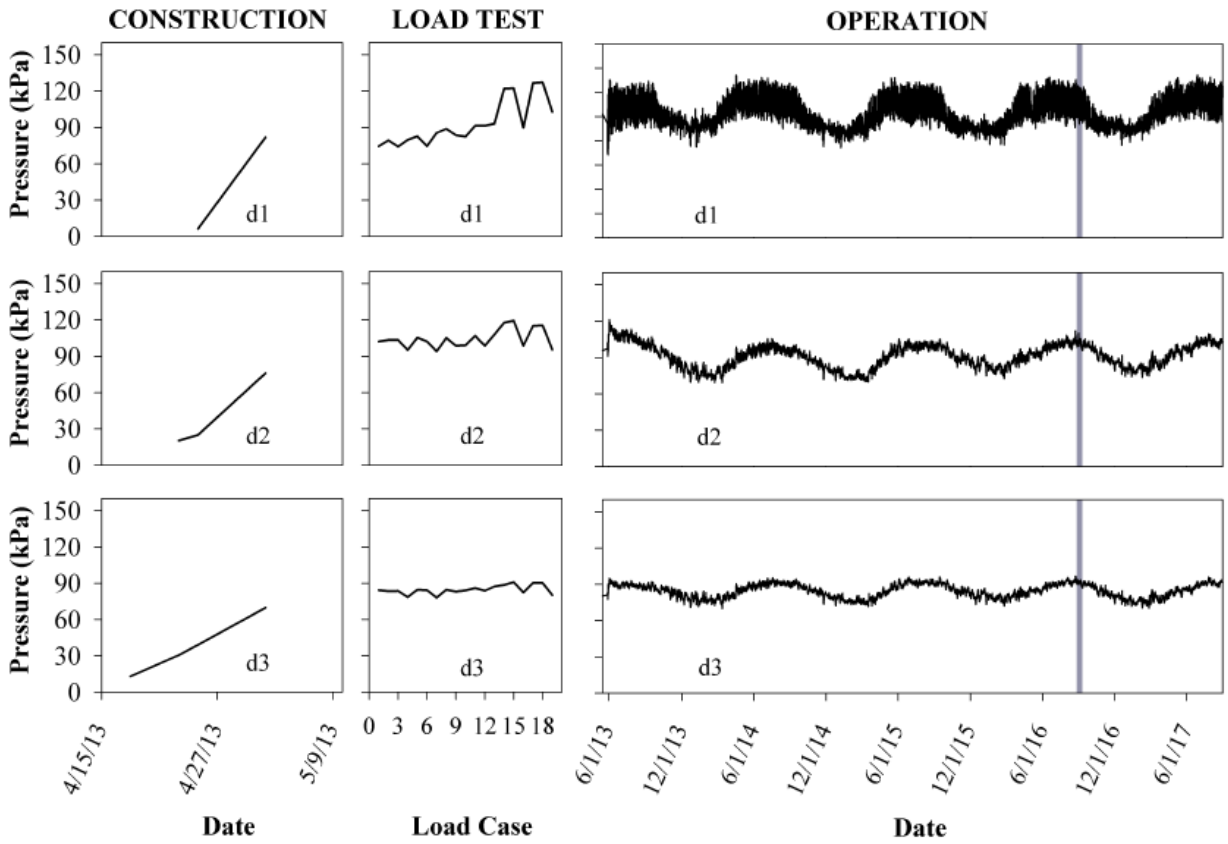

Figure 4.61 Measured abutment pressures

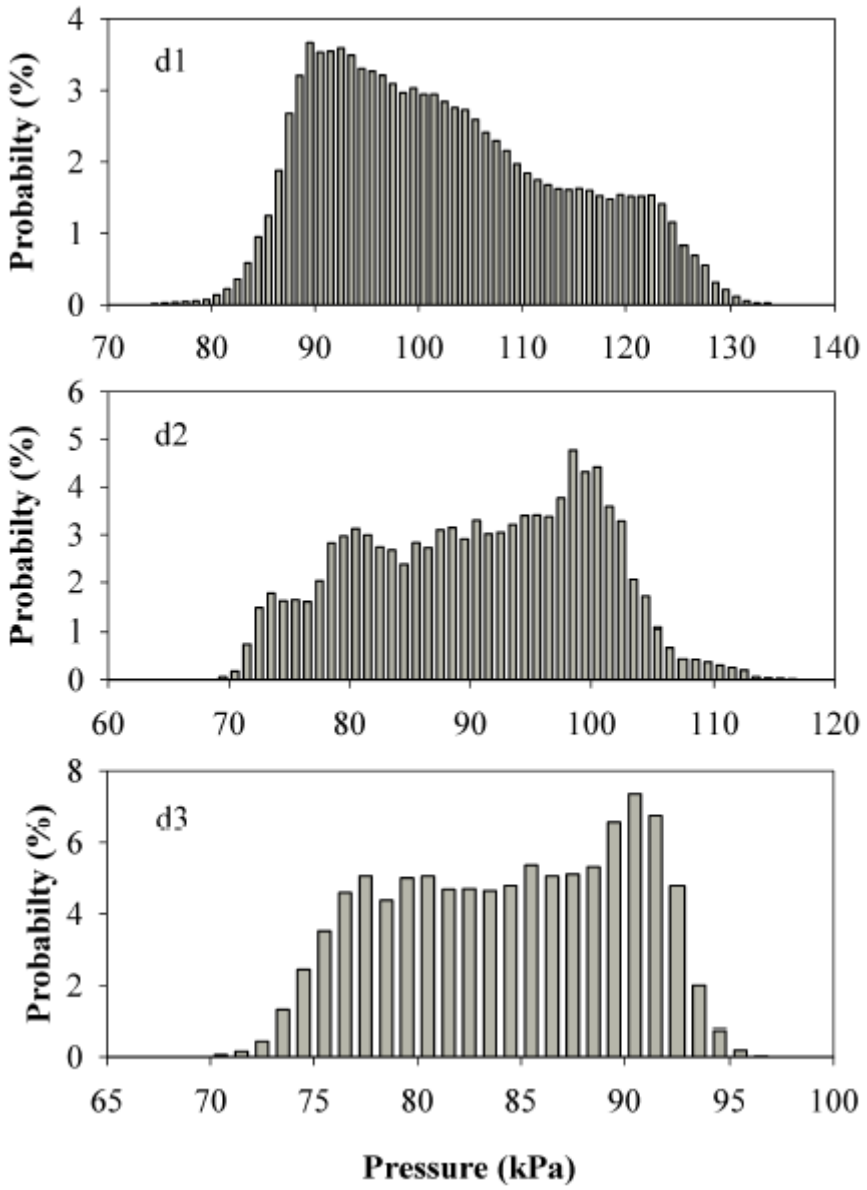

Figure 4.62 Histogram of measured abutment pressures for both monitoring periods

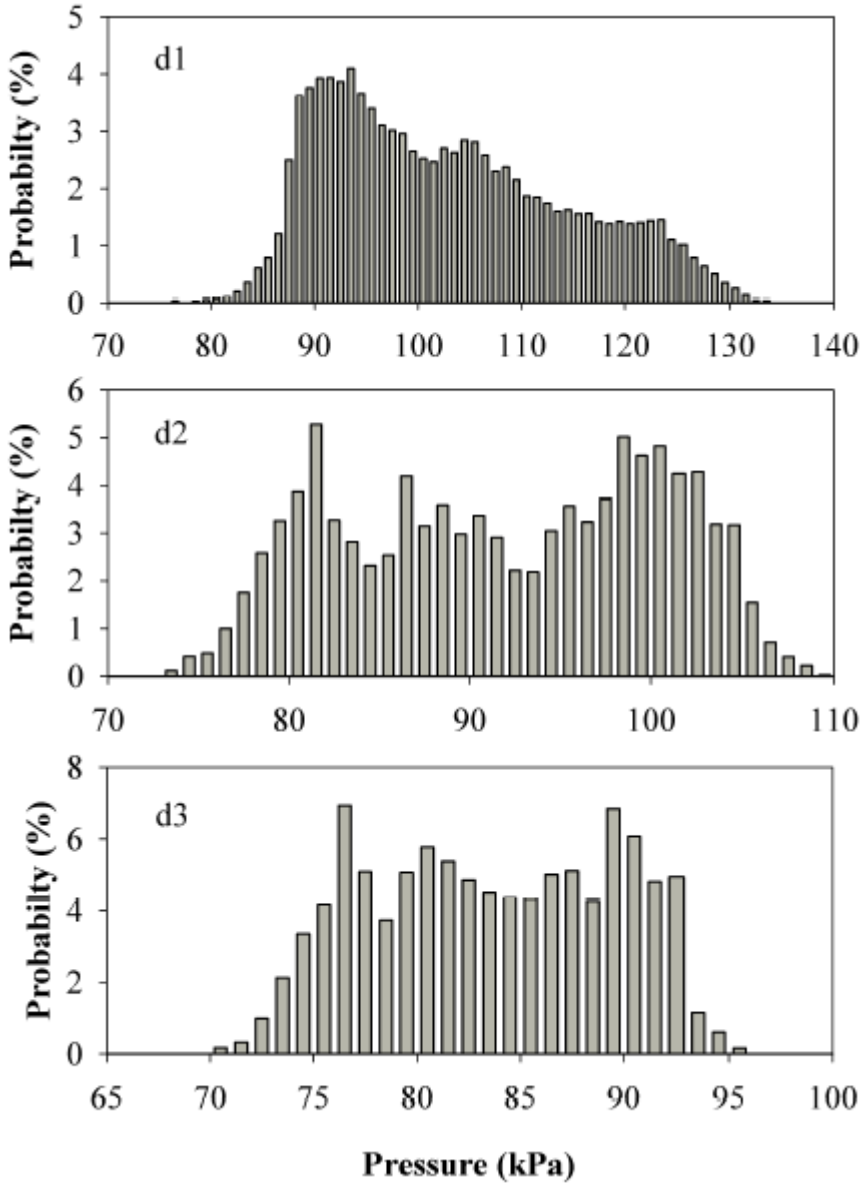

Figure 4.63 Histogram of measured abutment pressures for the current monitoring period

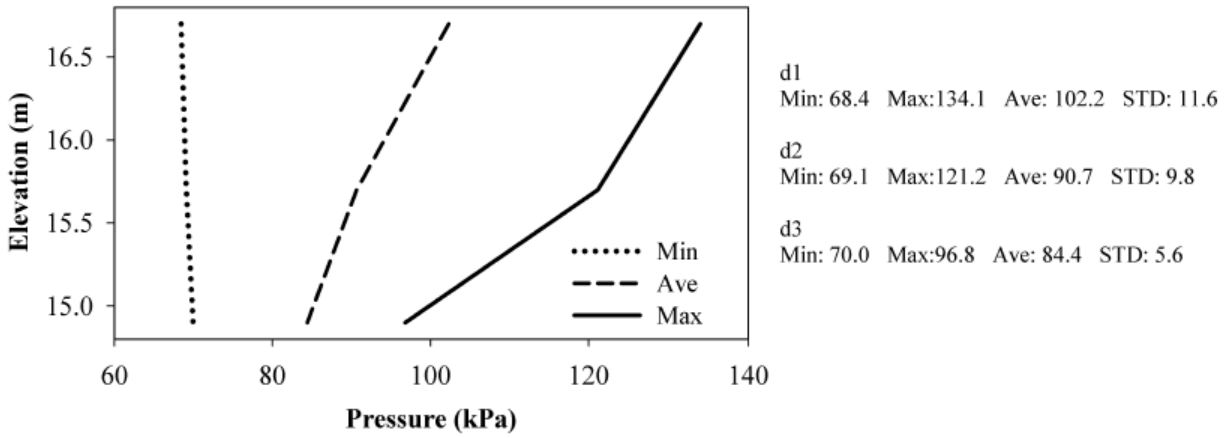

Figure 4.64 Minimum, maximum, and average measured abutment pressures for both monitoring periods

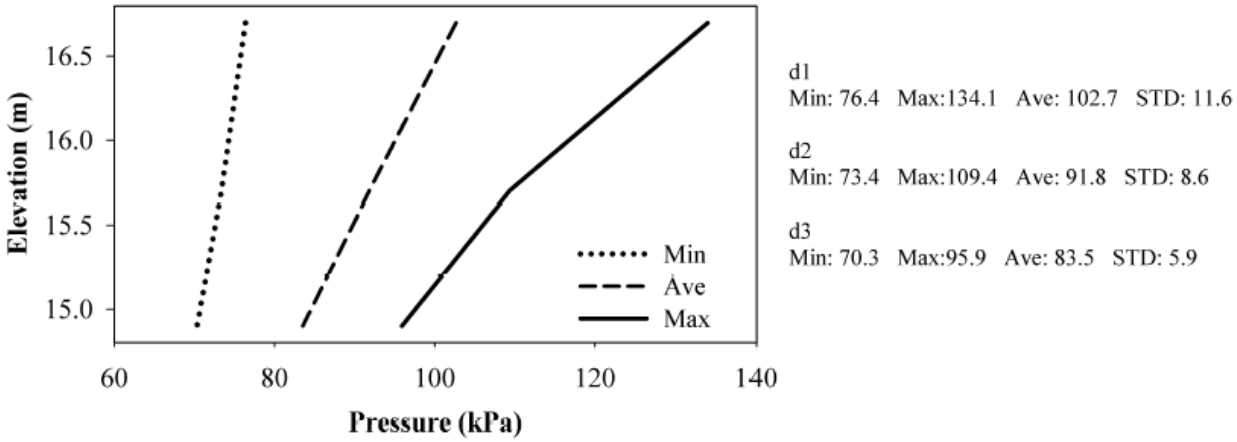

Figure 4.65 Minimum, maximum, and average measured abutment pressures for the current monitoring period

Similar to what was discussed in Section 4.2.7, temperature also has an effect on the abutment pressure cells and it is apparent as seasonal fluctuations can be seen in Figure 4.61. Again, a regression analysis was conducted and strong correlations were found between temperature and abutment pressure; an increase in the cell's temperature increased the cell's pressure, and vice versa. As mentioned, the seasonal changes in the measured pressure can be primarily attributed to changes in the pressure cell temperature. Talebi (2016) also investigated the noise in the abutment pressure cell readings by looking at the effect wire temperature had on the

pressure readings. It was determined that wire temperature changes are not the only source of noise in the abutment pressure cell readings.

The effect of air temperature on the abutment pressure cell readings was also investigated in Talebi (2016) where it was discovered that any increase in air temperature increases the pressure cell reading in d1 but decreases the pressure cell readings in d2 and d3. Overall, it was concluded that due to the location and the elevation of d1, the effect of the air temperature change on it is direct most of the time. For pressure cells d2 and d3, a similar conclusion was drawn to that of the foundation pressure cells in that the daily correlation coefficient between the air temperature and abutment pressure was mostly negative, thus indicating an inverse relationship.

Since the maximum measured pressure after bridge placement did not change from the first monitoring period, the factor of safety against abutment bearing capacity failure is still 4.5. Again, this is a conservative approach because it assumes the maximum applied pressure is applied continuously at all times (Talebi 2016).

4.3 Conclusion

In this chapter, the behavior of the GRS-IBS structure was investigated over construction, live load testing, and both monitoring periods with emphasis on the current monitoring period. The measured data by different types of sensors was discussed in detail. The following chapter will discuss the conclusions drawn from the analysis of this data and provide recommendations for the future.

References

Adams, M., Nicks, J., Stabile, T., Wu, J., Schelatter, W. and Hartmann, J. (2011). "Geosynthetic Reinforced Soil Integrated Bridge System Interim Implementation Guide." Federal Highway Administration, Publication No. FHWA-HRT-11-026, Washington, DC.

Meehan, C. L. and Talebi, M. (2017). "A Method for Correcting Field Strain Measurements to Account for Temperature Effects." Geotextiles and Geomembranes, Elsevier, 45(4), 250-260.

Talebi, M. (2016). "Analysis of the field behavior of a geosynthetic reinforced soil integrated bridge system during construction and operation", PhD Dissertation, University of Delaware, 2016.

Talebi, M., Meehan, C. L., and Leshchinsky, D. (2017). "Applied Bearing Pressure Beneath a Reinforced Soil Foundation Used in a Geosynthetic Reinforced Soil Integrated Bridge System." Geotextiles and Geomembranes, 45(6), 580-591.

Chapter 5

Conclusions and Recommendations

5.1 Introduction

Chapter 4 investigated the behavior of the GRS-IBS structure over construction, live load testing, and both monitoring periods with emphasis on the current monitoring period. This chapter will look to draw conclusions and give recommendations from the data presented in the previous chapter.

5.2 Conclusions

1. Water contents measured from the current monitoring period were consistent with what was recorded in the first monitoring period. Talebi (2016) suggested a slight increase in water content was observed over the first three years of operation and it should continue to be monitored, however this current monitoring period suggests that the water content within the abutment is steady and not increasing. For this monitoring period, water contents between 16% and 28% were observed. It was also observed that increases in precipitation increased the river water elevation, thus increasing abutment water content. It was concluded that after this current monitoring period the abutment water content did not significantly influence the structure's response.
2. The readings of pore water pressure from the piezometers very closely followed the water level in the river. Similar readings were seen in this monitoring period compared to the first, resulting in the conclusion that the structure's response was not significantly influenced by pore water pressure. No significant excess pore pressures were observed

in the current monitoring period. The measured precipitation and change in river water elevation were highly corelated, as expected. The maximum change in river water elevation was approximately 1.0 m.

3. Abutment temperature was directly affected by the air temperature. Seasonal fluctuations were greater for the parts of the abutment closest to the road surface and the abutment facing wall; readings at these locations also saw more noise in the recorded temperature signal as they were more affected by daily temperature changes. It was concluded that temperature within the abutment does not change significantly over the course of a single day. The temperature distribution for a cold day and a hot day are quite different however; on cold days, cold temperatures are seen near the ground surface and abutment facing wall with warmer temperatures seen further within the abutment. Vice versa is seen for hot days. No thermistors failed during the current monitoring period suggesting that thermistors that survive the first few years will likely continue to last into longer monitoring periods.
4. Measured strains of properly working abutment strain gauges were typically less than 0.5%. A total of 45 out of the 100 abutment strain gauges have failed or were deemed unreliable, an increase of 11 over this current monitoring period. This suggests that additional steps should be taken when protecting and waterproofing these gauges to improve survivability for long-term monitoring projects. It was seen that the estimated amount of creep from the start of the first monitoring period to the end of this current monitoring period (or right before the sensors stopped working properly) for the temperature corrected strains was generally less than 0.1%. No clear trend can be observed in the difference between strain readings for the short and long gauges.

Overall, the strain gauge readings from this current monitoring period were consistent with the readings from the previous monitoring period for the gauges that were still working properly.

5. The four strain gauges installed on the bottom of the bridge beams that were still working properly after the first monitoring period continued to work through this current monitoring period. The temperature corrected strains are less than 0.5%. Minimal creep was observed however, gauges b2 and b8 show greater signs of creep than the other sensors; this should continue to be monitored moving forward.
6. Minimal movement was observed in the facing wall with maximum lateral deflections and settlements of approximately 13 mm, which includes the error in the surveying approach ($\pm$6 mm); average recorded deflections and settlements were much lower than this amount. Maximum vertical strain of the GRS abutment was determined to be 0.27%, which is less than the recommended allowable vertical strain of 0.5%. The calculated maximum lateral strain was 1.18%, which exceeds the limit of 1% stated in the GRS-IBS Interim Implementation guide (Adams et al. 2011); however, the average deflection was only 4 mm which produces a horizontal strain of 0.4% (this is in good agreement with the horizontal strains measured by the strain gauges and it is probably more accurate). After a regression analysis, maximum slopes for lateral wall deflection and settlement were determined to be 1.17 and 1.42 mm per year respectively. Average slopes for lateral wall deflection and settlement were calculated as 0.23 and 0.91 mm per year, respectively. For the 51 months of monitoring, this results in a total average lateral deflection of 0.98 mm and a total average settlement of 3.87 mm. With lateral

deflections and settlements this small over 51 months of monitoring, it can be concluded that a very low amount of overall abutment deformation has occurred.

7. Lateral deflection of the clay foundation was measured using inclinometer sensors. Maximum deflections of 15 mm were observed, which over 51 months of monitoring, is not significant. Sensors In-1 and In-2 showed abnormal readings in the E-W direction at the end of this current monitoring period; this should continue to be monitored. Lateral deflections of the clay foundation in the N-S direction showed significantly more variation during the current monitoring period compared to the previous. This variation seemed to start at the end of the first monitoring period, however, these large spikes and variations tend to dissipate after some time. This trend should continue to be monitored.
8. Readings from the foundation pressure cells remained steady from the previous monitoring period to the current monitoring period. Histograms of the measured effective pressure for both monitoring periods and only the current monitoring period showed similar trends in shape, distribution, and average values. As discussed in Talebi (2016), a nonuniform pressure distribution was observed. The maximum pressure was recorded at sensor S2, underneath the facing wall elements, while the minimum pressure was recorded at sensor S1, under the toe of the foundation. Since the maximum applied pressure recorded was during the first monitoring period, the factor of safety against foundation bearing capacity failure of 3.1 did not change from Talebi (2016). The cell temperature effect on the pressure reading depends on different factors including temperature, pressure, cell properties, and installation was noted (Talebi

2016). It was also discussed how increases in the air temperature will decrease the foundation pressure readings and vice versa (Talebi 2016).

9. For the abutment pressure cells, almost identical behavior was seen in the current monitoring period compared to the previous monitoring period. This is shown by the similar histograms and minimum, maximum, and average values determined for each sensor comparing the monitoring periods. A seasonal and daily temperature effect is apparent for the abutment pressure cell readings. Talebi (2016) discussed how abutment pressure cell readings were affected by pressure cell temperature, daily air temperatures, and possibly bridge induced deformation by air temperature.
10. Overall, it was determined that the structure has performed satisfactorily over the course of construction, live load testing, and both monitoring periods of 51 months total.

5.3 Recommendations

1. GRS-IBS monitoring for this project should continue to investigate the long-term response of the structure; creep deformation of the abutment facing wall through surveying is a measurement of particular interest that should continue to be monitored. Lateral deflection and settlement usually occur over a long period of time. Creep can also be evaluated by continuous monitoring of properly working strain gauges. Under bridge strain gauges b2 and b8 should continue to be monitored due to the greater signs of creep shown in those sensors. Inclinometer sensors should also continue to be monitored to ensure the abnormal readings and high spikes that were observed with these sensors are stable over time.

2. As discussed in Talebi (2016), the effect of pressure cell temperature on the measured pressure is a factor. It is recommended that pressure cells be calibrated in the lab under different pressure and temperature conditions (Talebi 2016). Other researchers have suggested that each pressure cell be calibrated separately since calibration factors for each pressure cell are unique. For future work of this type, proper total pressure cell calibration under representative field conditions is considered to be particularly important.
3. For future studies of this type, sensors with high resolution and precision are recommended since the amount of strain, deflection, and settlement are generally quite small. In particular, a more accurate surveying operation should be utilized in future studies.

References

Talebi, M. (2016). "Analysis of the field behavior of a geosynthetic reinforced soil integrated bridge system during construction and operation", PhD Dissertation, University of Delaware, 2016.

Adams, M., Nicks, J., Stabile, T., Wu, J., Schelatter, W. and Hartmann, J. (2011). "Geosynthetic Reinforced Soil Integrated Bridge System Interim Implementation Guide." Federal Highway Administration, Publication No. FHWA-HRT-11-026, Washington, DC.